UNIVERSITE DE STRASBOURG

THESE

Présentée par

Cristian IACOVITA

Pour obtenir le titre de

Docteur de l'Université de Strasbourg

Domaine : Physique de la Matière Condensée

Spin-dependent tunneling into single cobalt-phthalocyanine molecules

Soutenue le 3 juin 2009 devant la commission d'examen :

Prof.	**Jean-Pierre BUCHER**	**Directeur de thèse**
Prof.	**Rodolfo MIRANDA**	**Rapporteur externe**
Dr.	**Mario RUBEN**	**Rapporteur externe**
Dr.	**Marc DRILLON**	**Examinateur interne**
Dr.	**Laurent LIMOT**	**Invité**

Institut de Physique et Chimie des Matériaux de Strasbourg,
UMR 7504, France

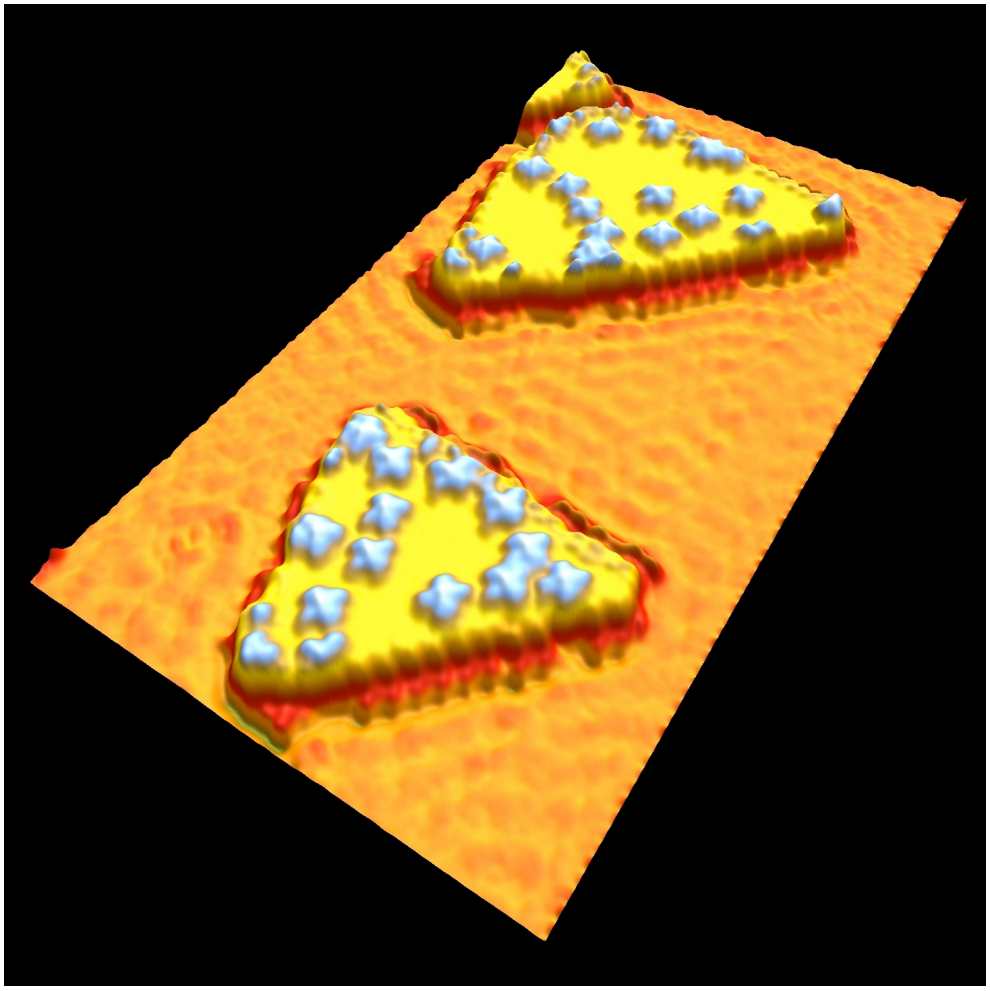

Abstract

The thesis presents an experimental study of both the electronic and the spin-polarized properties of single cobalt-phthalocyanine (CoPc) molecules, which are potentially interesting for the emerging field of molecular spintronics. The CoPc molecules were deposited on a non-magnetic and a magnetic surface and individually studied at low temperature using a scanning tunneling microscope. Two fundamental aspects of molecular spintronics are addressed, namely the injection of electron spins into a single molecule and the magnetic coupling of the molecule with the underlying magnetic surface. To do so, spin-polarized scanning tunneling spectroscopy is employed to locally inject spin-polarized electron across the vacuum barrier into a single CoPc molecule. Using the spin-polarized Co terminated tip and Co nanoislands of opposite magnetization as magnetic electrodes, and the CoPc molecule as an active element, spin-polarized electronic features are identified over the center of the molecule. The Co nanoislands were grown on Cu(111) and thoroughly calibrated to eliminate electronic artifacts. The stationary spin states of CoPc arise from the d-orbitals of the cobalt ion and reflect two molecular spin orientations. DFT calculations establish that CoPc couples ferromagnetically with the Co nanoislands through two exchange mechanisms (direct and superexchange), illustrating the important role played by the organic ligands in the spin-dependent transport properties. Comparative experimental studies are done on non-magnetic surfaces [Au(111) and Cu(111)], where the paramagnetic CoPc becomes non-magnetic upon adsorption, as DFT calculations predict.

Résumé

Cette thèse présente une étude des propriétés électroniques polarisés en spin d'une molécule individuélle de cobalt-phthalocyanine (CoPc), qui sont potentiellement intéressantes pour le domaine émergeant de l'électronique de spin. Les résultats expérimentaux sont analysés par des calculs de type DFT en collaborartion avec J. Kortus (Université Technique de Freiberg, Allemagne). Les molécules de CoPc ont été déposés sur des surfaces non-magnétiques et magnétiques, pour ensuite être individuellement étudiés à basse température par un microscope à effet tunnel. Deux aspects fondamentaux sont abordés: l'injection d'électrons polarisés en spin dans une molécule individuelle et le couplage magnétique de cette molécule avec une surface magnétique. En utilisant une pointe de Co polarisée en spin et un nanoîlot des Co comme électrodes magnétiques et la molécule de CoPc comme élément actif, une résonance polarisée en spin est identifiée sur le centre de la molécule. Cette résonance, ayant pour origine les orbitals moléculaire d du cobalt, reflète l'existence d'états stationnaires des spin. Ces états prouvent notamment que le moment magnetique de CoPc est figé dans une direction " up " ou " down " après adsorption sur la surface de cobalt magnétique. Les calculs DFT montrent que la molécule de CoPc est ferromagnétiquement couplée avec les nanoîlots via deux mécanismes d'échange (direct et superéchange) et illustrent le rôle important joué par les ligands organiques dans le magnétisme mais aussi dans le transport de spin. Des études expérimentales comparatives ont été effectué sur des surfaces non-magnétiques [Au(111) et Cu(111)] où la molécule de CoPc devient non-magnétique après adsorption comme les calculs DFT le prédisent.

Résumé étendu

La découverte de la magnétorésistance géante dans les multicouches magnétiques (Fe/Cr) par Albert Fert [1] et Peter Grunberg [2] en 1988 est considérée comme le début de l'électronique de spin, ou spintronique. Cette nouvelle branche de l'électronique est basée sur la dépendance en spin de la conductance et est potentiellement exploitable pour une caractérisation fine des nanostructures magnétiques. Au cours des ces dernières années, l'évolution de l'électronique de spin a permis une réduction des dimensions caractéristiques des composants électroniques, améliorant ainsi la densité d'intégration et la rapidité des circuits. En effet les nouvelles technologies doivent intégrer des composants dont les tailles sont inférieures à 10 nm avec des capacités de commutation et des propriétés d'interface flexibles. La plupart des recherches sur la miniaturisation des dispositifs de spintroniques ont été réalisée en utilisant des matériaux inorganiques, par exemple, les alliages de nickel, de fer et de cobalt [3]. Seul un petit nombre d'études ont exploité des couches moléculaires organiques comme barrière tunnel entre deux électrodes ferromagnétiques [4, 5, 6, 7, 8], et seul une étude a reussi l'exploit d'étudier une molécule individuelle [10]. Dans le même temps, quelques études théoriques du transport de spin à travers une molécule ont fait leur apparition [11, 12, 13, 14, 15].

Dans ce contexte, l'un des enjeux majeurs est de créer de nouveaux nanodispositifs de spin basé sur l'éléctronique moléculaire. En effet les molécules: a) sont de petite taille, généralement de quelques nanomètres, b) à l'aide de la chimie de coordination leur propriétés électroniques et magnétiques peuvent être finement réglées et c) elles peuvent être facilement manipulées par auto-assemblage. En particulier, il y a aujourd'hui un regain d'intêret pour les molécules consistuée d'un centre atomique entouré par des ligands organiques liés de manière covalente, par exemple les molécules de phthalocyanine et de porphyrine de métaux de transition. Le spin du centre métallique de telles molécules peut être en effet manipulé afin de créer de nouveaux interrupteurs et capteurs moléculaires basé sur le spin. Cependant, la création de cette nouvelle classe des dispositifs exige un gros effort pour comprendre et maîtriser le comportement de molécules magnétiques dans l'environnement métallique du dispositif. Un pas essentiel vers la réalisation de cet objectif sera d'étudier localement les propriétés de transport polarisées en spin, de visualiser la polarisation en spin d'une molécule individuelle et de comprendre l'interaction avec les surfaces inorganiques (non-magnétiques et magnétiques).

La plupart des techniques expérimentales utilisées afin de sonder le magnétisme, telle la microscopie par force atomique magnétique, la microscopie à balayage d'électron polarisé en spin,

le dichroïsme magnétique dans la gamme des rayons X etc., ont une résolution spatiale comprise entre 10 et 100 nm, et permettent donc d'accéder aux grandeurs moyennes des propriétés magnétiques. Cépendant ces technique sont inadaptée pour sonder des molécules, contairement à la microscopie à balayage à effet tunnel (STM) dont la résolution spatiale est subatomique [16]. Des études récentes ont montré qu'il est possible d'associer une sensibilité magnétique à la mesure STM en utilisant des pointes magnétiques [17]. Ainsi, l'injection locale des électrons tunnel devient sensible au spin permettant ainsi de relier les propriétés structurelles, électroniques et de transport avec les propriétés magnétiques de l'adsorbat. Ce courant tunnel polarisé en spin dépend fortement de l'orientation relative de l'aimantation de la pointe et de l'échantillon: il change fortement quand l'aimantation de la pointe et de l'échantillon sont parallèles et antiparallèles. Le STM polarisé en spin (SP-STM) peut aussi être considéré comme étant une jonction tunnel magnétique prototypique, puisqu'elle est composée de deux électrodes magnétiques bien caractérisée (la pointe et l'échantillon) séparés par une barrière isolante (le vide) dans un environnement expérimental très contrôlé. Par conséquent des relations claires peuvent être établies entre le transport dépendant du spin à travers des nano-objets et l'environnement magnétique. Par example, le SP-STM a permis de mettre en évidence l'interaction oscillatoire d'échange indirect RKKY entre un atome de Co individuel et un nanofil de Co présent à la surface de Pt(111) [18]. Un autre exemple révélateur est l'observation directe de la polarisation de spin d'atomes individuels déposés sur une surface magnétique [19]. Enfin, il a été possible de sonder les interactions magnétiques engendrées dans une chaine de dix atomes de manganèse déposées un par un sur une couche isolante [20].

Le STM a aussi été employé afin d'observer et eventuellment modifier l'interaction magnétique entre le spin magnétique de molécules telle la phthalocyanine ou la porphyrine et le spin d'électrons d'une surface hôte non-magnétique. Cette interaction est observé via l'effet Kondo qui se produit sur le centre métallique de ces molécules. La conductance différentielle, prise en positionnement la pointe au-dessus de l'atome centrale de la molécule, presente une résonance étroite (la résonance Kondo) près de l'énergie de Fermi et dont la largeur (la température Kondo) est proportionnelle au couplage magnétique entre l'atome et les électrons de la surface. Plusieurs groupes ont montré à l'aide d'un STM que la température de Kondo d'une molécule magnétique individuelle est très sensible: à son l'environnement moléculaire local [21], à sa conformation d'adsorption à la surface (sur la terrasse et aux marches atomiques) [22, 23, 24] et au site d'adsorption adoptée par son atome central magnétique [25]. Jusqu'à présent, cépendant, aucune étude STM n'a été consacrée au cas d'une molécule couplée à une surface magnetique.

Jusqu'à présent ceci a été abordé par dichroïsme magnétique circulaire des rayons X (XMCD). Il a été montré que le moment magnétique de Fe, dans une porphyrine de Fe adsorbée sur un substrat de Co et Ni, peut être orienté en cangeant l'aimantation du substrat magnétique à l'aide d'un champ magnétique extérieur [26].

Motivé par les progrès en SP-STM et par l'importance de ces molécules magnétiques, un de nos objectifs est de sonder et comprender à l'echelle locale comment ces molécules interagissent avec une surface magnétique bien caractérisée. Plus concrètement, dans ce travail de thèse nous avons couplé des études SP-STM basse température (4.7 K) avec des calculs théoriques DFT afin d'étudier le transport tunnel de spin dans une molécule individuelle de phthalocyanine de cobalt (CoPc). La molécule libre de CoPc possède un moment magnétique de $1.09\ \mu_B$ paramagnétique à l'ambiante. Afin de figer son moment magnétique, nous avons adsorbé la molécule de CoPc sur des nanoîlots magnétiques de cobalt maintenus à un temperature de 4.7 K. Ces nanoîlots qui croîent sur une surface de Cu(111), possédent à basse température une anisotropie magnétique perpendiculaire à la surface. Sur la surface magnétique la molécule de CoPc ne présente pas d'effet Kondo car son moment magnétique est bloqué. Une pointe STM magnétique peut alors être exploitée afin de produire un courant tunnel polarisé en spin en vue de sonder les états stationnaires de spin de la molécule. De plus, puisque le système point magnétique-vide-surface magnétique est un dispositif de type vanne de spin, cette étude permet aussi de sonder le transport dépendant du spin à travers une molécule individuelle. Les deux études (magnetisme moléculaire et transport de spin) n'ont jamais été abordés par une technique de champ proche.

La thèse s'articule sur six chapitres:
Le **chapitre 1** décrit le cadre général dans lequel s'inscrit ce travail de thèse.

Le **chapitre 2** débute avec la description de l'installation expérimental, à savoir le système d'enceinte ultravide et le microscope à effet tunnel basse température employé dans ce travail de thèse. Le chapitre se poursuit avec la présentation du mode opératoire du STM, suivi d'une présentation de la préparation de la pointe et des surfaces utilisées. Le cadre théorique de la spectroscopie à effet tunnel (STS) est ensuite présenté ainsi que la réalisation expérimentale de l'acquisition des spectres tunnel. La notion de chartographie de la conductance différentielle (dI/dV) est également illustrée. Finalement, l'évaporateur utilisé pour déposer les molécules est brièvement décrit.

Le **chapitre 3** est entièrement consacré à la molécule de phthalocyanine de cobalt (CoPc). Ce chapitre est divisé en deux parties. Il commence par une vue d'ensemble de la molécule de CoPc soulignant les précédents résultats obtenus avec STM et STS. Afin de nous familiariser avec les molécules de CoPc, nous les avons premièrement déposées sur une surface de Au(111) et étudiées leur auto-assemblage dans une monocouche. Dans l'étape suivante des CoPc individuelles déposées sur une surface de Cu(111) ont été analysées. Nous présentons plusieurs images topographiques en vue de vérifier l'intégrité et la conformation du CoPc après l'adsorption sur la surface. Puis la structure électronique locale du CoPc est présentée en examinant les spectres STS pris dans des endroits différents sur la molécule. Dans un nouveau paragraphe, les résultats expérimentaux sont confrontés aux calculs DFT. Ici, des informations sur le site d'adsorption de l'ion central de CoPc et surtout sur l'impact que la surface de Cu(111) a sur la structure électronique de CoPc sont détaillées. La seconde partie du chapitre porte sur l'adsorption du CoPc sur les nanoîlots magnétiques de cobalt. Après avoir résumé les propriétés électroniques de ces nanoîlots de cobalt dévoilées par STS, des résultats sur la croissance et les propriétés électroniques des CoPc sur ces nanoîlots sont présentés. Le chapitre se termine par un résumé des résultats obtenus.

Le **chapitre 4** commence par souligner les expériences le plus pertinentes qui ont été à l'origine des développement en spectroscopie tunnel de spin. Ensuite, la première expérience qui a conduit à la mise au point de la technique de STM polarisée en spin (SP-STM) est illustrée. Le premier paragraphe du chapitre se termine par une discussionportant sur le SP-STM en mode " courant constant ". On montre qu'une plus grande sensibilité magnétique est acquise par l'emploi du SP-STM en mode " cartographie de la conductance differentielle ". Son cadre théorique est présenté dans le deuxième paragraphe du chapitre, qui comprend également une étude sur les propriétés de spin des nanoîlots de cobalt, pertinentes pour cette thèse. La partie finale du chapitre est consacrée à l'influence de la géometrie de electrodes magnetique sur le transport de spin. En effet, dans une jonction magnétique SP-STM si une des deux électrodes est bien caractérisée (par example la surface magnétique du nanoîlots de cobalt), l'autre éléctrode (la pointe) peut présenter différentes formes. Nous montrons par un modèle analytique simplifié l'impact de ce facteur géométrique en comparant la polarisation d'une jonction où la pointe est planaire avec une jonction où la pointe a un sommet monoatomique. Le chapitre se termine sur un résumé des résultats obtenus.

Le **chapitre 5** présente les résultats les plus importants de la thèse. Il est divisé en deux parties qui comprennent les résultats expérimentaux et théoriques. La première section commence par une introduction du système CoPc/Co nanoîlots en mettant l'accent sur les propriétés magnétiques des nanoîlots en parallèle avec une discussion sur l'adsorption de CoPc. Les paragraphes suivants comprennent les résultats expérimentaux, qui démontrent l'existence des états stationaires polarisées en spin de CoPc adsorbée sur les nanoîlots de cobalt. En particulier, il est montré comment la détection et la visualisation de ces états stationnaires moléculaire de polarization opposée est possible. La distribution spatiale du signal polarisée en spin sur le CoPc est également présenté. Dans la section suivante, les résultats expérimentaux sont confrontés aux calculs DFT. Elles sont présentées en trois paragraphes. Tout d'abord, la géométrie de l'adsorption de la molécule de CoPc sur la surface magnétique de cobalt est discuté. Suit alors une discussion sur l'interaction qui apparait à l'interface CoPc/ surface de cobalt, en insistant sur l'origine des états stationaires polarisées en spin observées expérimentalment. Enfin, la nature de l'interaction d'échange magnétique entre CoPc et la surface magnétique de cobalt est examinée. Le chapitre se termine sur un résumé des résultats obtenus.

Le **chapitre 6** résume les résultats de cette thèse et présente quelques directions futures de recherche.

Bibliography

[1] M. N. Baibich, J. M. Broto, A. Fert, F. Nguyen Van Dau, F. Petroff, P. Eitenne, G. Greuzet, A. Friederich, and J. Chazelas. Giant magnetoresistance of (001)Fe/(001)Cr magnetic superlattices. Phys.Rev.Lett. **61**, 2472 (1988).

[2] G. Binash, P. Grünberg, F. Saurenbach, and W. Zinn. Enhanced magnetoresistance in layered magnetic structures with antiferromagnetic interlayer exchange. Phys.Rev.B **39**, 4828 (1989).

[3] J. P. Bucher. *Magnetism of free and supported metal clusters.* published in *Quantum Phenomena in Clusters and Nanostructures.* ed. by S. N. Khanna, and A. W. Castleman, Jr. Springer series in *Cluster Physics* pp. 83-137 (2002).

[4] K. Tsukagoshi, B. W. Alphenaar, and H. Ago. Coherent transport of electron spin in a ferromagnetically contacted carbon nanotube. Nature **401**, 572 (1999).

[5] V. Dediu, M. Murgia, F. C. Matacotta, C. Taliani, and S. Barbanera. Room temperature spin polarized injection in organic semiconductor. Solid State Commun. **122**, 181 (2002).

[6] M. Ouyang, and D. D. Awschalom. Coherent spin transfer between molecularly bridged quantum dots. Science **301**, 1074 (2003).

[7] Z. H. Xiong, D. Wu, Z. valy Vardeny, and J. Shi. Giant magnetoresistance in organic spin-valves. Nature **427**, 821 (2004).

[8] J. R. Petta, S. K. Slater, and D. C. Ralph. Spin-dependent transport in molecular tunnel junctions. Phys. Rev. Lett. **93**, 136601 (2004).

[9] W. Wanga, and C. A. Richterb. Spin-polarized inelastic electron tunneling spectroscopy of a molecular magnetic tunnel junction. Appl. Phys. Lett. **89**, 153105 (2006).

[10] A. N. Pasupathy, R. C. Bialczak, J. Martinek, J. E. Grose, L. A. K. Donev, P. L. McEuen, D. C. Ralph. The Kondo effect in the presence of ferromagnetism. Science **306**, 86 (2004).

[11] R. Pati, L. Senapati, P. M. Ajayan, and S. K. Nayak. First-principles calculations of spin-polarized electron transport in a molecular wire: Molecular spin valve. Phys. Rev. B **68**, 100407(R) (2003).

[12] E. G. Emberlya, and G. Kirczenowb. Molecular spintronics: spin-dependent electron transport in molecular wires. Chem. Phys. **281**, 311 (2002).

[13] A. R. Rocha, V. M. Garcia-Suarez, S. W. Bailey, C. J. Lambert, J. Ferrer, and S. Sanvito. Towards molecular spintronics. Nature Materials **4**, 335 (2005).

[14] D. Waldron, P. Haney, B. Larade, A. MacDonald, and H. Guo. Nonlinear spin current and magnetoresistance of molecular tunnel junctions. Phys. Rev. Lett. **96**, 166804 (2006).

[15] L. Senapati, R. Pati, and S. C. Erwin. Controlling spin-polarized electron transport through a molecule: The role of molecular conformation. Phys. Rev. B **76**, 024438 (2007).

[16] P. Grütter, W. Hofer, F. Rosei. *Properties of Single Organic Molecules on Crystal Surfaces*. Imperial College Press, London (2006).

[17] M. Bode. Spin-polarized scanning tunneling microscopy. Rep. Prog. Phys. **66**, 523 (2003).

[18] F. Meier, L. Zhou, J. Wiebe, and R. Wiesendanger. Revealing magnetic interaction from single-atom magnetization curves. Science **320**, 82 (2008).

[19] Y. Yayon, V. W. Brar, L. Senapati, S. C. Erwin, and M. F. Crommie. Observing spin polarization of individual magnetic adatoms. Phys. Rev. Lett. **99**, 067202 (2007).

[20] C. F. Hirjibehedin, C. P. Lutz, and A. J. Heinrich. Spin coupling in engineered atomic structures. Science **312**, 1021 (2006).

[21] V. Iancu, A. Deshpande, and S. W. Hla. Manipulation of the Kondo effect via two-dimensional molecular assembly. Phys. Rev. Lett. **97**, 266603 (2006).

[22] V. Iancu, A. Deshpande, and S. W. Hla. Manipulating Kondo temperature via single molecule switching. Nano Lett. **6**, 820 (2006).

[23] A. Zhao, Q. Li, L. Chen, H. Xiang, W. Wang, S. Pan, B. Wang, X. Xiao, J. Yang, J. G. Hou, and Q. Zhu. Controlling the Kondo effect of an adsorbate magnetic ion through its chemical bounding. Science **309**, 1542 (2005).

[24] A. Zhao, Z. Hu, B. Wang, X. Xiao, J. Yang, and J. G. Hou. Kondo effect in single cobalt phthalocyanine molecules adsorbed on Au(111) monoatomic steps. J. Chem. Phys. **128**, 234705 (2008).

[25] L. Gao, W. Ji, Y. B. Hu, Z. H. Cheng, Z. T. Deng, Q. Liu, N. Jiang, X. Lin, W. Guo, S. X. Du, W. A. Hofer, X. C. Xie, and H. J. Gao. Site-specific Kondo effect at ambient temperatures in iron-based molecules. Phys. Rev. Lett. **99**, 116402 (2007).

[26] H. Wende, M. Bernien, J. Luo, C. Sorg, N. Ponpandian, J. Kurde, J. Miguel, M. Piantek, X. Xu, Ph. Eckhold, W. Kuch, K. Baberschke, P. M. Panchmatia, B. Sanyal, P. M. Oppeneer, and O. Eriksson. Substrate-induced magnetic ordering and switching of iron porphyrin molecules. Nat. Mater. **6**, 516 (2007).

Acknowledgments

It is a great pleasure for me to express my gratitude to Prof. Jean-Pierre Bucher, my thesis director, for giving me the opportunity to perform this challenging research in his group from the Department of Organic Materials of IPCMS. Here I spent a great time and I had the possibility to work in a really enthusiastic, stimulating and pleasant environment.

I am very happy that I had the chance to meet and to work with Dr. Laurent Limot, who obtained a permanent position in our group in the beginning of my thesis. I would like to thank him for his mentoring, patience, availability and for introducing me for the first time in the Scanning Tunneling Microscopy and Spectroscopy. His ideas, theoretical and experimental skills have been contributed a lot to the success of this thesis. Furthermore, his careful reading of the manuscript is gratefully acknowledged.

I will take this opportunity to deeply acknowledge Dr. Mircea Rastei and PhD student Benjamin Heinrich for the scientific discussions and their help at different stage of the project. In particular I want to acknowledge Prof. Jean Kortus and his student Thomas Brumme for the DFT calculations presented in this thesis. In the same time I thank all members of the jury that have agreed to move and to judge my work during this thesis.

My sincerely thanks go to the Romanian scientific community from IPCMS: Petru, Lucian, Lenuta, Liviu, Sorin, Ovidiu, Silviu, Gabriela, Mircea, Simona, Ovidiu, Ela and Claudiu, who supported morally during the last four years of my stay in Strasbourg. I would also like to thank to Silviu, Simona, Theo, Mihai and Costin for the nice moments, the parties and especially the football games that we spent together.

Last but not least, I would like to truly thank my family: my parents Marioara and Traian and my sister Adina as well as my aunt Angela and uncle Pompei for their confidence and support through the difficult times.

I dedicate this thesis to my grandparents:
To whom I owe being who I am

Contents

Chapter 1

Introduction

1.1 Motivation

The discovery of the giant magnetoresistance in magnetic multilayers (Fe/Cr) by Albert Fert [1] and Peter Grunberg [2] in 1988 is considered the beginning of spin electronics, or spintronics, a new branch of electronics based on the spin dependence of the conductance which can be exploited in magnetic nanostructures. Over the past years, the development of spin electronics has involved reducing the characteristic size of the components in order to improve both the integration density and the speed of the circuits. Possible new technologies must have controllable features of sizes below 10 nm, switching capability (preferably non-charge based) and flexible interface properties. Most of the research on the miniaturization of spintronic devices have been carried out using inorganic materials, such as nickel, iron and cobalt [3]. A few studies have experimentally tested the implementation of organic molecules as the tunnel barrier between two magnetic electrodes [4, 5, 6, 7, 8, 9] and only one of them has studied the case of an individual molecule [10]. At the same time a few seminal theoretical studies on spin transport through a single molecule have appeared [11, 12, 13, 14, 15].

In this context, one of the major challenges of the scientific community is to create new nano-devices that use the spin of a single molecule as an active element. The motivation is provided by the idea that organic molecules have specific properties that make them attractive for application in spintronic devices. Organic molecules: $a.)$ are small, typically a few nanometers, $b.)$ with coordination chemistry their electronic and magnetic properties can be finely adjusted and, $c.)$ they can be easily manipulated by self-assembly. Moreover, organic molecules used as

spacer in spin-valve devices, preserve spin coherence over large distances due to their, inherently low spin-orbit interaction. In particular, magnetic molecules consisting of an atomic center surrounded by covalently bonded organic ligands are of great interest. The state variable describing such molecules is the quantum spin of the metal centers, which can potentially be manipulated in active molecular nanostructures to create new spin-based molecule-scale switches and sensors. However, the creation of this new class of devices requires an effort to understand and control the behavior of such molecules in the magnetic environment of the device. An essential step towards achieving this tantalizing goal will be $1.)$ to study how spin-polarized currents can be locally injected, manipulated and detected in a single magnetic molecule and $2.)$ to understand the interaction of its spin with the magnetic surface.

Most of the techniques used for measuring the magnetic properties of adsorbates, such as magnetic force microscopy (MFM), scanning electron microscopy with polarization analysis (SEMPA), X-ray magnetic circular dichroism (XMCD) etc, have a limited spatial resolution between 10 and 100 nm and offer only an access to spatially averaged magnetic properties. Progress in scanning tunneling microscopy (STM) has provided access to the physical properties of single molecules with a sub-molecular resolution [16]. At the same time it was shown that it is possible to associate a spin sensitivity to the STM measurements using spin-polarized tips [17]. Thus, the local injection of the spin-polarized electrons between both the tip and the surface allows not only the investigation of magnetic properties but also a direct correlation between the spin-polarized structure and the geometric structure. The spin-polarized current depends strongly on the relative orientation of the magnetizations of both the tip and the sample: it increases when the magnetizations are aligned parallel and decreases when they are aligned antiparallel. Moreover, spin-polarized scanning tunneling spectroscopy (SP-STS) represents a prototypical magnetic tunneling junction, since it is composed of two well-characterized magnetic leads (the tip and the sample) separated by a vacuum barrier in a highly controlled experimental environment. Indeed, owing to the ultra-high vacuum environment ($< 10^{-10}$ mbar), the impurities which alter or even cancel the spin-polarized transport are not present inside the magnetic junction. Therefore clear relations can be established between the spin-dependent transport across single magnetic nano-objects (atoms and molecules) and their interaction with the magnetic environment, including the coupling between their individual spin and the magnetic surface. Recent studies using cryogenic scanning tunneling microscopy have illustrated different magnetic couplings, namely, the direct coupling, the indirect RKKY exchange and superexchange coupling. These studies are highlighted in the next section.

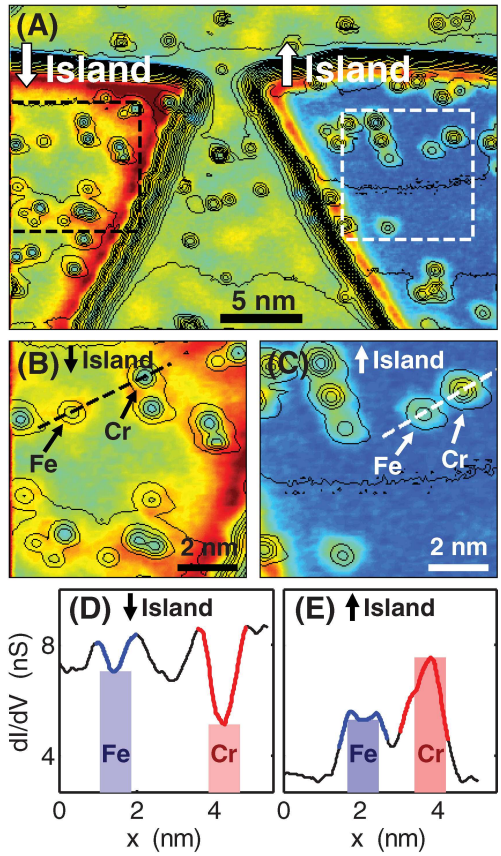

Figure 1.1: a) Spin-polarized dI/dV map of Fe and Cr adatoms on $\downarrow$ and $\uparrow$ cobalt nanoislands grown on Cu(111) (Tunneling parameters: $V = -0.365$ V, $I = 20$ pA). b) and c) Zoom-in of areas marked by dashed lines on $\downarrow$ and $\uparrow$ cobalt nanoislands in (a). d) and e) Line scans marked by dashed lines in (b) and (c) through the centers of Fe and Cr adatoms on $\downarrow$ and $\uparrow$ cobalt nanoislands, respectively (from [18]).

1.2 Magnetic interactions probed by STM

The experiments performed by Yayon et *al.* [18] can be regarded as an example of a STM observation of a direct exchange coupling. A spin-polarized dI/dV map for Fe and Cr atoms codeposited on two cobalt nanoislands with opposite spin polarization is presented in Fig. 1.1 a. The right cobalt nanoisland is spin-polarized $\uparrow$ and has a blue color, while the left cobalt nanoisland is spin-polarized $\downarrow$ and has a yellow color. Blue color represents a low dI/dV (differential conductance) signal, whereas the yellow color suggest a high dI/dV signal. It can be observed (Figs. 1.1 b and 1.1 c) that the Fe adatoms have the same intensity as the cobalt

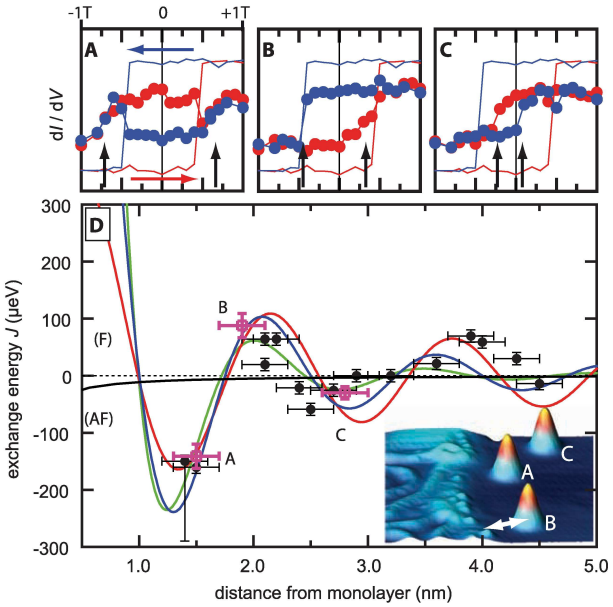

Figure 1.2: A), B) and C): Magnetization curves measured on the cobalt monolayer (straight lines) and on the three adatoms (dots) A, B, and C visible in the inset topography of (D). The blue color indicates the down sweep from $B = +1$ T to -1 T and red the up sweep from $B = -1$ T to $+1$ T. The vertical arrows indicate the exchange bias field, B_{ex} (Tunneling parameters: $I = 0.8$ nA, $V = 0.3$ V). D) The dots show measured exchange energy as a function of distance from cobalt monolayer as indicated by the arrow in the inset. The red, blue, and green lines are fits to 1D, 2D, and 3D range functions for indirect exchange. Horizontal error bars are due to the roughness of the Co-monolayer-stripe edge, whereas the vertical ones are due to the uncertainty in B_{ex} (from [19]).

nanoislands while the Cr adatoms display an opposite intensity. The line cuts trough the Fe and the Cr atoms (Figs. 1.1 d and 1.1 e) indeed show that the Fe atom on the $\downarrow$ nanoisland exhibits a larger dI/dV signal than the Fe atom on the $\uparrow$ nanoisland. On the contrary, the Cr atom on the $\downarrow$ nanoisland displays a smaller dI/dV signal than the Cr atom on the $\uparrow$ nanoisland. The STM data, taken for a given voltage, however cannot established the nature of the coupling since it evidences only a spin polarization but not a magnetization (as we will see the two are linked, but are not identical). Theoretical calculations predict that the Fe adatoms prefer ferromagnetic alignment to the cobalt surface, while the Cr adatoms exhibit an antiferromagnetic alignment. The exchange energy predicted is $U = -0.5$ eV for the Fe adatoms and $U = 0.25$ eV for the Cr adatoms.

The indirect RKKY exchange interaction has been experimentally detected by Meier et *al.*

[19] between stripes of one atomic layer cobalt grown at room temperature along the Pt(111) surface steps [20] and individual cobalt adatoms deposited at about 25 K on the bare Pt(111) surface (inset of Fig. 1.2 D). In the first step they have realized the magnetization curves of both monolayer stripes and adatoms, by positioning the spin-polarized probe tip above them and then measuring the spin-polarized current as a function of an applied external magnetic field. The dI/dV spectrum recorded on the cobalt stripe shows a pronounced feature below E_F, with the peak energy depending on the specific stacking of the atoms [20]. When the applied magnetic field is swept the intensity of the differential conductance (dI/dV) at this peak changes, giving rise to a regular square-like magnetic hysteresis curve (Fig. 1.2 A), corresponding to ferromagnetic behavior. The adatom, which is 1.5 nm away from the stripe edge (labelled A in the inset of Fig. 1.2 D), behaves completely differently (Fig. 1.2 A). As an example, in the down sweep, the adatom magnetization switches from up to down at positive $B = +0.7$ T (see black arrow), whereas at negative magnetic field, it switches back to up simultaneously with the reversal of the stripe magnetization from up to down at $B = -0.5$ T, and then at $B = -0.7$ T it is again forced into the down state (see black arrow). It can be observed that, at the zero field, where the stripe magnetization points downward, the adatoms magnetization is oriented upward. This suggest an antiferromagnetic coupling of the adatom to the stripe corresponding to an interaction energy of $J \approx -150$ μeV ($m = 3.7\mu_B$). The magnetization curve of a more distant adatom (labeled B in the inset of Fig. 1.2 D) shows a ferromagnetic coupling, which means that at zero field the adatom magnetization is forced parallel to the stripe magnetization (Fig. 1.2 B). An even more distant adatom (labeled C in the inset of Fig. 1.2 D) again couples antiferromagnetically (Fig. 1.2 C). The interaction energies J of the three adatoms (labeled A,B and C) as a function of their distance from the stripe edge (Fig. 1.2 D) shows a damped oscillatory behavior. Therefore the magnetic exchange coupling, alternating between ferromagnetic and antiferromagnetic, illustrates that these interactions are strongly distance dependent. Moreover the corresponding fits to the data suggest that an RKKY-like exchange description is the most appropriate. As a consequence, the interactions between adatoms and stripe is due to indirect exchange via the Pt itinerant conduction electrons.

Experimentally, the superexchange interaction between spins in individual atomic-scale magnetic structures has been probed by Hirjibehedin et *al.* [21]. The experiments were performed on square-shaped insulating nanoislands one atomic-layer-high of copper nitride (CuN) formed on the Cu(100) surface [22] (Fig. 1.3 a). The bright spots in the topography are hollow sites that are flanked by four Cu atoms (Fig. 1.3 a). Manganese atoms, evaporated on the pre-cooled

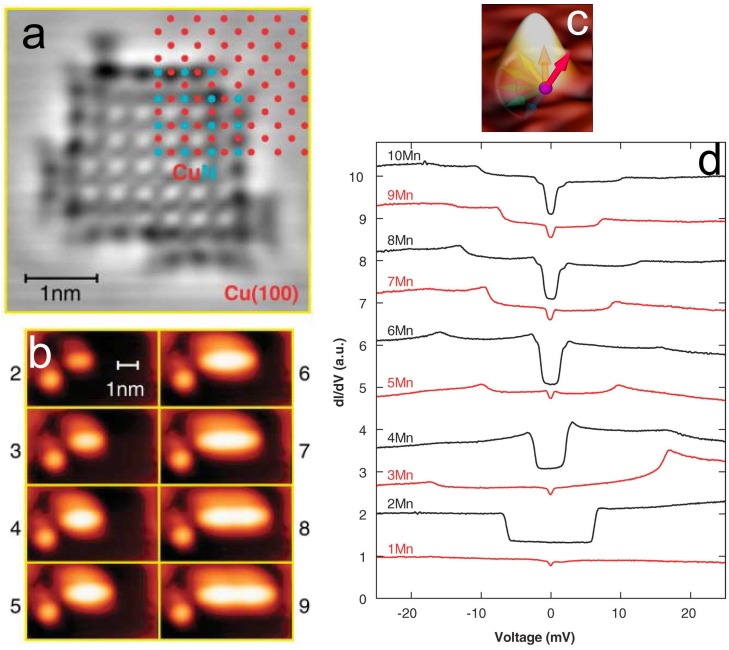

Figure 1.3: a) STM image of CuN nanoisland on Cu(100) with lattice positions of Cu (red dots) and N (blue dots) atoms overlaid (Tunneling parameters: $I = 1.0$ nA, $V = 10$ mV). b) STM image of the building of a chain of Mn atoms, lengts 2 to 9, on CuN nanoisland (Tunneling parameters: $I = 0.1$ nA, $V = 10$ mV). c) A conceptual representation of the spin of a Mn atom, being flipped from the "down" to "up" state. d) dI/dV spectra of Mn chains on CuN. Spectra were taken with the tip positioned above the center of chains of Mn atoms of lengths 1 to 10 at $T = 0.6$ K and $B = 0.0$ T. (Tunneling parameters: $V = 20$ mV, $I = 1.0$ nA). Successive spectra are vertically offset by one unit for clarity. Odd spectra are in red and even spectra are in black to emphasize the parity dependence (from [21]).

CuN/Cu(100) system, were then manipulated [23, 24] on the CuN surface with atomic precision. In this way the authors have constructed linear chains of 1 to 10 Mn atoms one atom at a time (Figs. 1.3 b). On the insulating nanoislands the Mn atoms were positioned atop Cu atoms so that one nitrogen atom lays between each pair of Mn binding sites. The authors have analyzed the engineered linear chains by employing the technique called *spin excitation spectroscopy* developed by Heinrich et *al.* [25]. This technique is a magnetic version of the inelastic electron tunneling spectroscopy (IETS) which has allowed to measure excitation energies, such as vibrational energies of single molecules within a tunnel junction [26]. In the case of the magnetic atom within the tunnel junction, at a certain threshold voltage, the tunneling electrons injected into the atom will have sufficient energy to perform an allowed spin excitation

(thus loosing some of their energy). Heinrich et *al.* have shown that the energy transfered to the single Mn atom (adsorbed on Al_2O_3) by the inelastic channel causes a spin flip (Fig. 1.3 c), appearing as a narrow dip in the dI/dV spectrum centered at the Fermi level [25]. A single Mn atom placed on the CuN surface when excited with tunneling electrons, behaves in the same way (Fig. 1.3 d). As can be seen in Fig. 1.3 d, the zero-bias narrow dip in the dI/dV spectrum is present for all odd-length chain, whereas it is absent in all even-length chains. The absence of spin-flip excitations for even-chains suggests that the total spin in the ground state is $S = 0$, and the presence of such excitations in odd-chains implies their ground state to have $S \neq 0$; therefore, the chains are ordered antiferromagnetically. The *ab initio* calculations based on DFT methods have shown that the Cu atoms that host the Mn adatoms moved towards the bulk while the Mn adtoms create bonds with their neighboring N atoms. In this way two neighboring Mn atoms are interconnected by N atoms and thus the Mn-Mn interaction is mediated by N-orbitals giving rise to an antiferromagnetic coupling. Therefore, the nitrogen atom helps realizing the magnetic coupling between two localized spins. As a matter of fact nitrogen atoms are present in the structure of many molecules, as metalloderivatives of porphyrins and phthalocyanines, it is known that they provide a possible magnetic exchange pathway between the metal atom of the molecules and the surface atoms. Not surprisingly the author have analyzed the spectroscopic results using the same Heisenberg Hamiltonian model employed to describe the antiferromagnetic interactions between manganese atoms inside a Mn_{12} molecular magnet [27]. As a conclusion, the above result represents an atomic-scale toolbox for engineering local magnetic molecule and exploring their magnetism.

1.3 STM studies on magnetic molecules

Transition metal-phthalocyanine or phorphyrin molecules can be magnetic. The molecular magnetism arises from the unpaired spins residing in the d-orbitals of the atom. Such molecules adsorbed on metallic substrates have recently gain special interest in view of the emerging field of spintronics, as the ligands attachments to the magnetic atom can change its electronic distribution and therefore novel interaction mechanisms can arise in such systems. The STM has been employed for observing and controlling the magnetic interaction between the spin of these magnetic molecules and the electrons of metallic substrates. On a surface the interaction between the molecular spin ant the electron spins of the host metal gives rise to a many

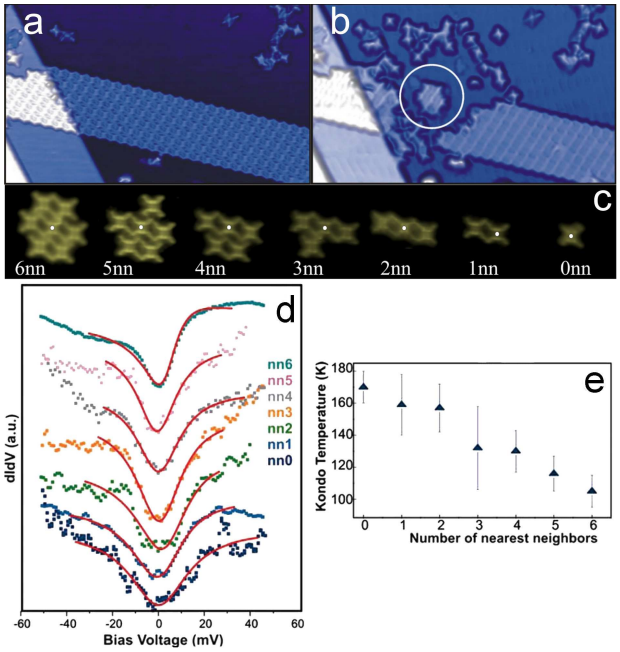

Figure 1.4: a) and b) The TBrPP-Co molecules from the ribbon (a) are removed by using STM to create a hexagonal cell (circled) (b) (Scan size: 28×50 nm^2; Tunneling parameters: $I = 0.2$ nA, $V = 1.0$ V). c) A sequence of STM images with different number of nearest neighbors created by removong one molecule at a time with the STM tip. The with dots indicate the tip position during the recording of the dI/dV spectra. d) Kondo resonance for different number of nearest neighbors. The spectra are vertically and horizontally displaced for clarity. e) The plot of Kondo temperature as a function of the number of nearest neighbors (from [28]).

body phenomenon known as the Kondo effect. In the dI/dV spectrum taken by positioning the STM tip above the central atom of the molecule, the signature of the Kondo effect is a narrow resonance (the Kondo resonance) that appears near E_F (Fig. 1.4 d) and whose width (the Kondo temperature) is proportional to the magnetic coupling between the atom and the host electrons. A standard STM tip (non-magnetic) is sufficient to detect this resonance. Iancu et *al.* [28] have modified the Kondo temperature in a two-dimensional molecular assembly of TBrPP-Co (bromophenyl-porphyrin-Co) molecules on a Cu(111) surface. In the first step, the authors have created a hexagon of TBrPP-Co molecules, by removing molecules from a TBrPP-Co ribbonlike monolayer island with the STM tip (Fig. 1.4 a and 1.4 b). The molecular hexagon is formed by six TBrPP-Co molecules surrounding one TBrPP-Co molecule placed in the center of the hexagon. In the second step, the hexagon was disassembled by moving one

of the six surrounding TBrPP-Co molecules (Fig. 1.4 c). The Kondo signature was determined above the same center molecule after each molecule removal. The recorded dI/dV spectra for different number of nearest neighbors are illustrated in Fig. 1.4 d. It can be observed that when the number of nearest neighbor (nn) molecules decreases, the width of the Kondo resonance increases. Thus, using this manipulation scheme, the authors to tune the Kondo temperature from 105 K to 170 K (Fig. 1.4 e).

The same authors have shown that a change of the TBrPP-Co molecule conformation, without altering its chemical composition, can lead to a variation in the Kondo temperatures [29]. In an important work, Zhao et *al.* [30] have changed the magnetic nature of the cobalt phthalocyanine (CoPc) molecule adsorbed on Au(111) surface by altering its structure. For pristine CoPc molecules sitting on the Au(111) surface they observed the d-orbital of the inner cobalt ion to be an energetically broad resonance lying below the Fermi energy. After cutting away eight hydrogen atoms from the periphery of the molecule with voltage pulses from a STM tip, the broad d-resonance is presumably replaced by a Kondo resonance with a high Kondo temperature (more than 200 K). Currently, Kondo resonances with Kondo temperatures above room temperature are found for iron phthalocyanine (FePc) molecules on Au(111) surface in STM measurements [31]. It was also shown that the signal of the Kondo resonance depends strongly on the adsorption site of the FePc. Experimental data were verified by extensive numerical simulations, which establish that the coupling between iron orbitals and states of the substrate depends strongly on the adsorption configuration. Other studies have provided feasible ways to modulate the Kondo resonance at the single molecular level by ligand attachment [32] and by exploiting the quantum size effects in ultrathin Pb films grown on Si(111) substrate [33]. Experiments such as these reported above form a complement to the transport measurements because they provide direct microscopic evidence of how specific, well-characterized molecular contact configurations lead to different electronic and magnetic behaviors.

Magnetic substrates offer the interesting possibility of probing the interaction of the magnetic surface with the spin of the metal atom in a metallorganic complex. This topic has only been addressed using X-ray magnetic circular dichroism (XMCD). Induced magnetic order of Mn-tetraphenylporphyrins on a Co film as well as a magnetic coupling between the Mn-porphyrin and the Co film was demonstrated [34]. Very recently, induced magnetic ordering and switching of the Fe spin in Fe-porphyrins on Co and Ni substrates was also shown [35, 36].

The studies mentioned in the previous sections have convincingly shown that the STM is a suitable tool $1.)$ for probing different magnetic interactions at a single atomic level, $2.)$ for

controlling the Kondo effect at a single molecular level and $3.$) for determining the conformation of single adsorbed molecules. Motivated by the technical advances in STM and by the importance of magnetic molecules in future spin-based devices, our goal is to fulfill the gap that exists in understanding the interaction between a single magnetic molecule and a magnetic surface. In particular in this thesis, SP-STM and SP-STS studies at low temperature (4.7 K) are coupled with theoretical calculations to study the spin-polarized transport through a single magnetic cobalt phthalocyanine (CoPc) molecule. The CoPc molecule has an uncompensated magnetic moment of 1.09 Bohr magnetons [30, 37], but is paramagnetic. In order words its magnetic moment fluctuating in directions under thermal activation. Thus, in order to freeze the magnetic moment, we need to place the CoPc in an anisotropic environment (for example, a solid state material). For this purpose the CoPc molecules are deposited on magnetic cobalt nanoislands grown on Cu(111) surface which exhibit a perpendicular magnetic anisotropy with respect to the surface plane [38]. On the magnetic surface a molecule will not exhibit a Kondo effect, since its magnetic moment is quenched. However, a magnetic tip can be exploited to produce a spin-polarized tunneling current in order to probe the stationary spin states of the molecule. Moreover, the spin-polarized tip together with the magnetic surface form a spin-valve device where the insulating layer is the vacuum barrier. Therefore, we are in a position to study locally the magnetic properties of a single molecule, but also the spin transport across a single molecule. Both studies have never been addressed by a near-field technique.

The thesis is organized as follows:

Chapter 2 gives a detailed description of the apparatus used to characterize the electronic and magnetic properties of an individual molecule. The apparatus is a scanning tunneling microscope (STM) that was designed to operate at low temperatures and in ultra-high vacuum environment. Beside the imaging, STM can also be used to perform spectroscopy. The density of states of an adsorbate can be locally determined using scanning tunneling spectroscopy (STS). The theoretical background of STS together with the experimental realization of spectra acquisition is presented in this chapter. An example of STS is also given to introduce the notion of dI/dV map. At the end of the chapter a homebuilt molecular evaporator is briefly described.

Chapter 3 is divided in two parts. After an overview of previous STM and STS studies of cobalt-phthalocyanine (CoPc) molecules, the first part starts with the STM measurements of a supramolecular self-assembly of CoPc on Au(111). Follows then a study on the adsorption

and electronic properties of individual CoPc on Cu(111). Insight on the interaction occurring at the CoPc-Cu(111) metal interface is given by density functional theory calculations. The second part of this chapter begins with an overview of the electronic properties of the cobalt nanoislands as revealed by STS. Afterwards, the growth and the electronic properties of CoPc molecules on these nanoislands are discussed.

Chapter 4 is devoted to spin-polarized scanning tunneling microscopy (SP-STM). This method is spin sensitive and has a high spatial resolution which allows not only the investigation of magnetic properties but also the direct correlation to electronic structure measurements and topographic studies. Herein, this method is employed to study the cobalt nanoislands. It is shown that the SP-STM in constant-current mode is not well suited for a clear separation between topological and magnetic contributions to the measured signal of the cobalt nanoislands. A higher magnetic sensitivity is gained in the images by employing spin-polarized scanning tunneling spectroscopy (SP-STS). It allows to identify two magnetically different cobalt nanoislands types (of same stacking): either of spin up or of spin down with respect to the surface plane. Based on a simple theoretical model, developed in this thesis, we discuss the role of the tip-apex geometry in spin-polarized electron tunneling. Two types of geometry are taken into account: a blunt tip, viewed as a surface of small area and a sharp tip, defined as one single atom added onto the surface.

Chapter 5 presents the most important results of the thesis. It includes spin-polarized measurements through an individual CoPc deposited on cobalt nanoislands of opposite polarization. It is shown that the interaction between the CoPc molecule and the cobalt surface results in two molecular spin-polarizations. The spatial distribution of the spin-polarized signal over the CoPc is also presented. The experimental results are compared to DFT calculations. Herein, we discuss the adsorption geometry of the CoPc molecules on cobalt surface, the interaction occurring at the CoPc-Co surface interface, the origin of the experimentally observed spin-polarized stationary states and the nature of the magnetic exchange interaction between CoPc molecule and the magnetic cobalt surface.

Chapter 6 summarizes the research achievements of this thesis and presents future research directions.

Bibliography

[1] M. N. Baibich, J. M. Broto, A. Fert, F. Nguyen Van Dau, F. Petroff, P. Eitenne, G. Greuzet, A. Friederich, and J. Chazelas. Giant magnetoresistance of (001)Fe/(001)Cr magnetic superlattices. Phys.Rev.Lett. **61**, 2472 (1988).

[2] G. Binash, P. Grünberg, F. Saurenbach, and W. Zinn. Enhanced magnetoresistance in layered magnetic structures with antiferromagnetic interlayer exchange. Phys.Rev.B **39**, 4828 (1989).

[3] J. P. Bucher. *Magnetism of free and supported metal clusters.* published in *Quantum Phenomena in Clusters and Nanostructures.* ed. by S. N. Khanna, and A. W. Castleman, Jr. Springer series in *Cluster Physics* pp. 83-137 (2002).

[4] K. Tsukagoshi, B. W. Alphenaar, and H. Ago. Coherent transport of electron spin in a ferromagnetically contacted carbon nanotube. Nature **401**, 572 (1999).

[5] V. Dediu, M. Murgia, F. C. Matacotta, C. Taliani, and S. Barbanera. Room temperature spin polarized injection in organic semiconductor. Solid State Commun. **122**, 181 (2002).

[6] M. Ouyang, and D. D. Awschalom. Coherent spin transfer between molecularly bridged quantum dots. Science **301**, 1074 (2003).

[7] Z. H. Xiong, D. Wu, Z. valy Vardeny, and J. Shi. Giant magnetoresistance in organic spin-valves. Nature **427**, 821 (2004).

[8] J. R. Petta, S. K. Slater, and D. C. Ralph. Spin-dependent transport in molecular tunnel junctions. Phys. Rev. Lett. **93**, 136601 (2004).

[9] W. Wanga, and C. A. Richterb. Spin-polarized inelastic electron tunneling spectroscopy of a molecular magnetic tunnel junction. Appl. Phys. Lett. **89**, 153105 (2006).

[10] A. N. Pasupathy, R. C. Bialczak, J. Martinek, J. E. Grose, L. A. K. Donev, P. L. McEuen, D. C. Ralph. The Kondo effect in the presence of ferromagnetism. Science **306**, 86 (2004).

[11] R. Pati, L. Senapati, P. M. Ajayan, and S. K. Nayak. First-principles calculations of spin-polarized electron transport in a molecular wire: Molecular spin valve. Phys. Rev. B **68**, 100407(R) (2003).

[12] E. G. Emberlya, and G. Kirczenowb. Molecular spintronics: spin-dependent electron transport in molecular wires. Chem. Phys. **281**, 311 (2002).

[13] A. R. Rocha, V. M. Garcia-Suarez, S. W. Bailey, C. J. Lambert, J. Ferrer, and S. Sanvito. Towards molecular spintronics. Nature Materials **4**, 335 (2005).

[14] D. Waldron, P. Haney, B. Larade, A. MacDonald, and H. Guo. Nonlinear spin current and magnetoresistance of molecular tunnel junctions. Phys. Rev. Lett. **96**, 166804 (2006).

[15] L. Senapati, R. Pati, and S. C. Erwin. Controlling spin-polarized electron transport through a molecule: The role of molecular conformation. Phys. Rev. B **76**, 024438 (2007).

[16] P. Grütter, W. Hofer, F. Rosei. *Properties of Single Organic Molecules on Crystal Surfaces*. Imperial College Press, London (2006).

[17] M. Bode. Spin-polarized scanning tunneling microscopy. Rep. Prog. Phys. **66**, 523 (2003).

[18] Y. Yayon, V. W. Brar, L. Senapati, S. C. Erwin, and M. F. Crommie. Observing spin polarization of individual magnetic adatoms. Phys. Rev. Lett. **99**, 067202 (2007).

[19] F. Meier, L. Zhou, J. Wiebe, and R. Wiesendanger. Revealing magnetic interaction from single-atom magnetization curves. Science **320**, 82 (2008).

[20] F. Meier, K. von Bergmann, P. Ferriani, J. Wiebe, M. Bode, K. Hashimoto, S. Heinze, and R. Wiesendanger. Spin-dependent electronic and magnetic properties of Co nanostructures on Pt(111) studied by spin-resolved scanning tunneling spectroscopy. Phys. Rev. B **74**, 195411 (2006).

[21] C. F. Hirjibehedin, C. P. Lutz, and A. J. Heinrich. Spin coupling in engineered atomic structures. Science **312**, 1021 (2006).

[22] F. M. Leibsle, C. F. J. Flipse, and A. W. Robinson. Structure of the Cu(100)-c(2×2)N surface: A scanning-tunneling-microscopy study. Phys. Rev. B **47**, 15865 (1993).

[23] D. M. Eigler, C. P. Lutz, and W. E. Rudge. An atomic switch realized with the scanning tunnelling microscope. Nature **352**, 600 (1991).

[24] L. Bartels, G. Meyer, and K. H. Rieder. Basic steps of lateral manipulation of single atoms and diatomic clusters with a scanning tunneling microscope tip. Phys. Rev. Lett. **79**, 697 (1997).

[25] A. J. Heinrich, J. A. Gupta, C. P. Lutz, and D. M. Eigler. Single-atom spin-flip spectroscopy. Science **306**, 466 (2004).

[26] B. C. Stipe, M. A. Rezaei, and W. Ho. Single-molecule vibrational spectroscopy and microscopy. Science **280**, 1732 (1998).

[27] D. Gatteschi, R. Sessoli, and J. Villain. *Molecular Nanomagnets*. Oxford University Press, Oxford (2006).

[28] V. Iancu, A. Deshpande, and S. W. Hla. Manipulation of the Kondo effect via two-dimensional molecular assembly. Phys. Rev. Lett. **97**, 266603 (2006).

[29] V. Iancu, A. Deshpande, and S. W. Hla. Manipulating Kondo temperature via single molecule switching. Nano Lett. **6**, 820 (2006).

[30] A. Zhao, Q. Li, L. Chen, H. Xiang, W. Wang, S. Pan, B. Wang, X. Xiao, J. Yang, J. G. Hou, and Q. Zhu. Controlling the Kondo effect of an adsorbate magnetic ion through its chemical bounding. Science **309**, 1542 (2005).

[31] L. Gao, W. Ji, Y. B. Hu, Z. H. Cheng, Z. T. Deng, Q. Liu, N. Jiang, X. Lin, W. Guo, S. X. Du, W. A. Hofer, X. C. Xie, and H. J. Gao. Site-specific Kondo effect at ambient temperatures in iron-based molecules. Phys. Rev. Lett. **99**, 116402 (2007).

[32] P. Wahl, L. Diekhöner, G. Wittich, L. Vitali, M. A. Schneider, and K. Kern. Kondo effect of molecular complexes at surfaces: ligand control of the local spin coupling. Phys. Rev. Lett. **95**, 166601.

[33] Y. S. Fu, S. H. Ji, X. Chen, X. C. Ma, R. Wu, C. C. Wang, W. H. Duan, X. H. Qiu, B. Sun, P. Zhang, J. F. Jia, and Q. K. Xue. Manipulating the Kondo Resonance through Quantum Size Effects. Phys. Rev. Lett. **99**, 256601 (2007).

[34] A. Scheybal, T. Ramsvik, R. Bertschinger, M. Putero, F. Nolting, and T. A. Jung. Induced magnetic ordering in a molecular monolayer. Chem. Phys. Lett. **411**, 214 (2005).

[35] H. Wende, M. Bernien, J. Luo, C. Sorg, N. Ponpandian, J. Kurde, J. Miguel, M. Piantek, X. Xu, Ph. Eckhold, W. Kuch, K. Baberschke, P. M. Panchmatia, B. Sanyal, P. M. Oppeneer, and O. Eriksson. Substrate-induced magnetic ordering and switching of iron porphyrin molecules. Nat. Mater. **6**, 516 (2007).

[36] M. Bernien, X. Xu, J. Miguel, M. Piantek, Ph. Eckhold, J. Luo, J. Kurde, W. Kuch, K. Baberschke, H. Wende, and P. Srivastava. Fe-porphyrin monolayers on ferromagnetic substrates: electronic structure and magnetic coupling strength. Phys. Rev. B **76**, 214406 (2007).

[37] B. Bialek, I. G. Kim, and J. I. Lee. Density functional investigation of the electronic structure of cobalt phthalocyanine monolayer. Thin Solid Films **513**, 110 (2006).

[38] O. Pietzsch, A. Kubetzka, M. Bode, and R. Wiesendanger. Spin-polarized scanning tunneling spectroscopy of nanoscale cobalt islands on Cu(111). Phys. Rev. Lett. **92**, 057202 (2004).

Chapter 2

Scanning tunneling microscopy and spectroscopy

A scanning tunneling microscope (STM) which operates in a ultra-high environment and at low temperature was used during this thesis to investigate the electronic and spin-polarized properties of single molecules. The beginning of the chapter is devoted to introducing the ultra-high vacuum setup and the low-temperature scanning tunneling microscope. After that, the general operating principle of the scanning tunneling microscope is presented, followed by a description of the tip and sample preparation. One of the most fascinating potential of the STM is its possibility of extracting information on the electronic structure of surfaces or adsorbates on a local scale. This is done trough scanning tunneling spectroscopy (STS). The theoretical background of the STS together with the experimental realization of spectra acquisition is given in the second part of the chapter. As an example, the STS over the noble crystals is presented. Taking advantage on the confinment of surface state electrons in artificial engineered nanocavities the notion of dI/dV map is also introduced. The investigated molecules were deposited on the substrates from a home built molecular evaporator, whose specific design will briefly be described at the end of the chapter.

2.1 Experimental setup

2.1.1 The ultra-high vacuum system

Investigating individual molecules by scanning tunneling microscopy (STM) requires an atomically clean environment, where contaminants are minimized. For this purpose, we use ultra-high vacuum (UHV) where the pressure is typically below 10^{-10} mbar, and a temperature of 4.6 K or lower, in order to freeze the diffusion of the studied adsorbates. The UHV consists of a main chamber, a load lock chamber and a STM chamber, all made of stainless steel (Fig. 2.1). The main chamber is formed from two adjacent chambers: the preparation chamber and the intermediary chamber which connects the preparation and the STM chamber. The preparation chamber is equipped with sample cleaning facilities, a heating device (positioned within the chamber) and two e-beam evaporation sources. These are used to deposit a precise amount of metal (e.g. Co and Cr). The material to deposit is in the form of a metal rod, which is heated up by bombarding with an electron beam of typically a few mA at a energy up to 1 keV. This leads to the evaporation of a minute quantities from the top end of the rod. In the intermediary chamber is located an homebuilt evaporation source, designed to deposit molecules on the surfaces, together with a quartz balance, a tungsten filament used for tip cleaning and two transfer rods. The main transfer rod provides translational (along the chamber axis) and rotational mobility ($360°$) to position and transfer the sample (tip) to different locations in the intermediary and preparation chamber. The other one has four sample (tip) carriers and is used to transfer the prepared samples (tips) inside the STM chamber. The STM chamber hosts the scanning tunneling microscope and is separated from the main chamber by a gate valve. By closing this valve, the sample (tip) preparation can be performed without contaminating the STM chamber.

The sample cleaning includes several cycles of ion sputtering and annealing. Sputtering of the sample is performed by establishing a partial pressure of argon (Ar) in the chamber (2×10^{-6} mbar) trough a leak-valve and then generating an Ar^+ ion beam focused onto the sample by a ion bombardment gun. The thermal annealing is then necessary to heal the sputtering damage, thus producing large atomically flat terraces. The *in situ* thermal treatment of the sample is done by heating trough electronic bombardment. This is done using a tungsten filament, located at a distance of 0.5 mm below the sample holder and traversed by a current of a few amps. A high voltage (800 V) applied between the filament and sample support, leads

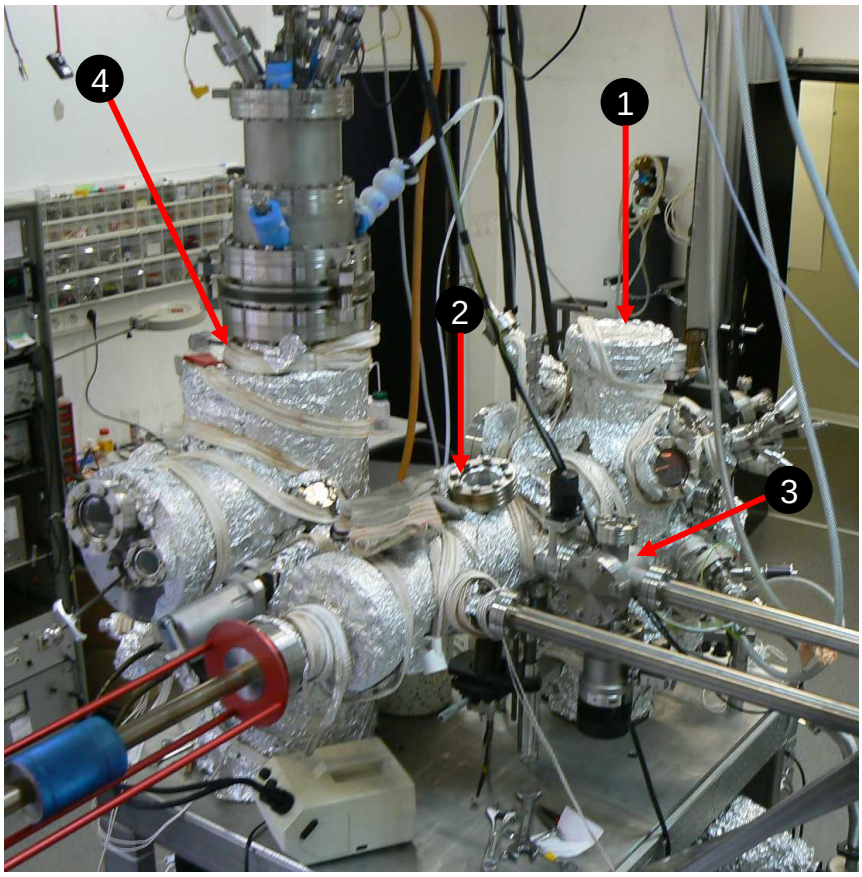

Figure 2.1: Photo illustrating the ultra-high vacuum system with its components: (1) preparation chamber, (2) intermediary chamber, (3) lock load chamber and (4) STM chamber.

to electron acceleration and heating of the sample. The temperature is controlled by means of a thermocouple attached to the sample support. The maximum temperature that can be reached is about 1000 K.

The UHV system uses three different types of pumps: three rotary pumps, two turbomolecular pumps, two ion pumps. To pump the system from the atmosphere down to 10^{-3} mbar pressure, one of the rotary pumps is used. The whole main chamber is pumped by one of the turbomolecular pumps, which requires a starting pressure of at least 10^{-2} mbar. A rotary pump and a turbomolecular pump are located on the load lock chamber which is equipped with a transfer rod, allowing to transfer the samples and tips from UHV to atmosphere and vice-versa without breaking the UHV in the main chamber. Both preparation and STM chambers are equipped with ion pumps that keep the pressure at 2×10^{-10} mbar provided that baking of the

system took place. During the baking all the chambers are wrapped with electric heating tapes and temperature is set up to $120°$C for two days so that all the water and residual gases on the walls are removed. After the baking, all the filaments are out gassed and then STM is cooled down to helium temperature. The pressure in the main chamber reaches almost 10^{-10} mbar while the STM chamber reaches the 10^{-11} mbar range due to the cryopumping of the cold surfaces. Once a sample is plugged into the STM, the environment is so clean that little or no contaminants is apparent down to the atomic scale even after weeks of measurements. The pressure monitoring in both main and STM chamber is done using two ion gauges. The samples and tips are introduced into the STM from a room temperature carousel (comprising six storage drawers for sample plates and/or tip transfer plates) with a wobblestick.

2.1.2 The scanning tunneling microscope

The direct investigation of the sample surface and its adsorbates was done with a scanning tunneling microscope (STM). The microscope allows to image not only the surface and its adsorbates, but also the electronic and spin-polarized properties as well (Chapter 3, 4, 5). Measurements in this thesis were performed with a commercial low-temperature STM provided by Omicron. It uses a single tube scanner with a maximum scan range (at room temperature) of about 10 μm $\times$ 10 μm with a z-travel of about 1 μm. A z-resolution of 0.01 nm can be achieved.

Isolation from the mechanical vibrations is very important for a STM as the tunneling current is exponentially dependent on the distance between tip and sample. To address this matter two damping systems are implemented. First the STM stage is suspended by three soft springs whose resonant frequency is around 2 Hz, therefore providing a vertical damping. Second, lateral vibrations are eliminated using an eddy current damping mechanism, formed by copper plates inserted between permanent magnets. The copper plates are arranged in circular manner around the STM head. Just before triggering the approach procedure to the tunneling regime, the STM head is released and hence the scanner and the sample are suspended since they are connected to the rest of the instrument only through the three springs. Beside isolation from the mechanical vibration the STM stage is also isolated from thermal radiation by a concentric cryogenic bath. The lowest sample temperature achieved without pumping the cryostat is 4.6 K. The thermal drift is small at this temperature and hence, it is possible to perform measurements at the same surface location.

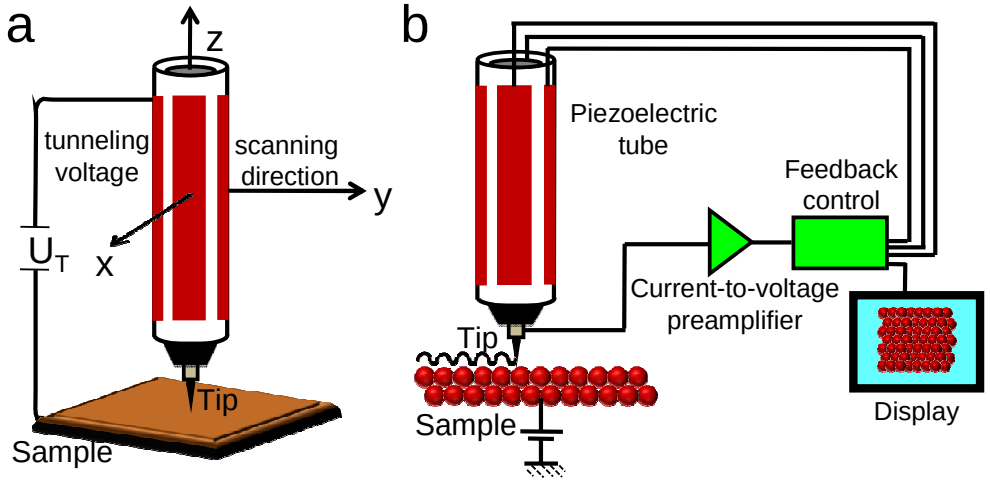

Figure 2.2: a) Schematic diagram of the STM junction: a tunneling voltage applied to a tip and a sample 1 nm away generates a tunneling current. b) Schematic representation of data acquisition with a STM.

2.2 Image acquisition: Topography

2.2.1 Tunneling current

A scanning tunneling microscope is based on the quantum mechanical principle of electron tunneling. A bias voltage applied across a junction formed by a tip and a conducting sample separated by 1 nm produces a measurable tunneling current across the junction (Fig. 2.2 a).

While moving the tip over the sample, its lateral position (x and y direction) as well as its vertical (z) position relative to the sample is controlled with subnanometer precision by means of a piezoelectric tube [1]. A feedback loop system constantly maintains the tip-sample interaction at a given value by making adjustments to the z position of the tip relative to the sample. These adjustments are recorded by a computer and presented as an image (Fig. 2.2 b). The STM can be employed following two different modes of operation: constant-height mode and constant-current mode. In the constant height mode, the height between the tip and the sample is kept constant and the variation of the tunneling current due to the changes in surface structure is detected. Such a working mode allows only to scan small areas, typically 5×5 nm^2. In this thesis the STM measurements were done in the constant-current mode. The tunneling current is kept constant by means of the feedback-loop. It checks the tunneling current with a reference value and the difference is converted in voltage which is used to drive the z piezo

up or down. The changes in the elongation of the piezo tube are recorded, reflecting then, the surface landscape. Such an image is called a topography.

The magnitude of the tunneling current depends exponentially on the distance between the two electrodes and is expressed by the following equation:

$$I \propto V\rho_s(0, E_F)\exp\left(-1.025\sqrt{\Phi}\ d\right) \tag{2.1}$$

where V, ρ_s and Φ(eV) represents the bias voltage, the density of states of the sample and the apparent barrier height, respectively [2]. The distance between the tip and the sample is expressed by d(Å). The exponential sensitivity of the tunneling current on the tip-sample separation is one of the key aspects of the STM. This implies that only the very end of the tip and a very small portion of the sample are involved in the tunneling process. Such a localized interaction is crucial for a real space investigation of surfaces at the atomic scale. With a lateral resolution below the Angstrom, the inventors of the STM, Gerd Binning and Heinrich Rohrer could obtain for the first time features such as monoatomic steps [3], surface reconstruction as well as atomic resolution of metal [4, 5] and semiconductor [6] surfaces in real space.

2.2.2 Tip and sample preparation

The tips used to obtain the experimental results presented in this thesis (in particular, those presented in Chapter 3) were made with a polycrystalline tungsten (W) wire (diameter of 0.3 mm) which were etched chemically in sodium hydroxide solution ($2M$ NaOH). After fixing the tip in the tip holder it was inserted into the vacuum chamber by a tip carrier plate. To remove the oxide film of the tungsten tip, it was heated to 1000 K for a short time by resistive heating. Sputtering of the tip was subsequently done with the Ar^+-ion bombardment gun at energies between $1-2$ keV for a duration of 12 minutes. The sharper the tip is, the higher is the lateral resolution. A sharp tip is generally defined as having its apex formed by a single atom sitting in a threefold hollow site. The apical atom carries about 90% of the tunneling current because of the difference in distance between it and the atoms at its base. Usually sharp tips are not obtained by traditional sputtering and annealing treatments. Therefore, additional tip treatments are done *in situ*. $1.)$ By applying a voltage pulse between tip and sample a rearrangement of the tip-apex on the atomic scale by a loss of material is possible. $2.)$ A controlled way to tailor the tip apexes is vertical manipulation, where single atoms are

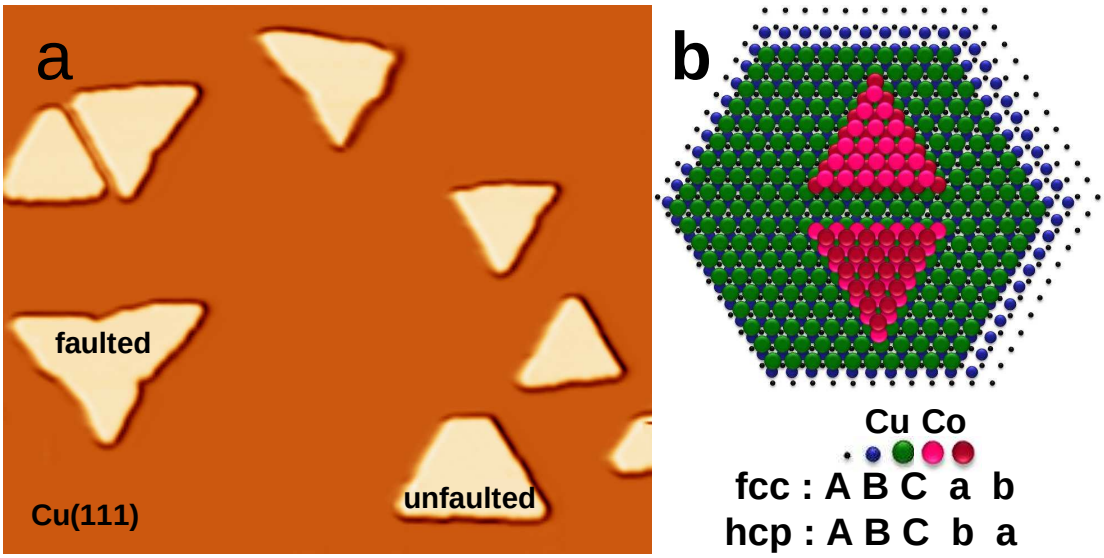

Figure 2.3: a) Constant-current image of two-atomic-layer high Co nanoislands on Cu(111). The scan range is 90 nm $\times$ 41 nm and the tunneling parameters are $V = 0.4$ V, $I = 1.5$ nA. b) The model proposed for the two types of islands shown in panel (a). The unfaulted nanoislands follow the fcc stacking sequence and the faulted ones present a stacking fault following a hcp stacking sequence.

transfered from tip apex to the surface [7, 8]. $3.$) Alternatively, the controlled dipping of the tip into the substrate, can be performed. In this way the tungsten tip picks up atoms from the surface (it is coated with substrate material) and the local Joule heating leads to a re-shaping of the tip apex [9].

In this thesis two types of surfaces are used: a non-magnetic metallic copper surface cleaved along a (111) plane and a magnetic cobalt surface. Performing experiments on single molecules requires the preparation of a clean surface. The single Cu(111) crystal has been prepared *in situ* according to regular surface science techniques by several cycles of Ar^+-ion bombardment (sputtering) and annealing. Sputtering was done at energies of 1 keV for a duration of 20 minutes at a pressure of about 1.5×10^{-6} mbar. During the annealing the Cu(111) crystal was steadily heated up to 500 K, kept at this temperature for 3 minutes and then slowly cooled down. The above described recipe, allows to produce atomically flat and clean metallic substrate. The quality of the pure metallic substrate was routinely checked by means of STM. The STM images show atomically flat terraces with typical size in the order of hundred nanometer. A 1-2% contamination from bulk impurities was found.

The magnetic overlayer has been realized by evaporation of about 0.7 monolayer (ML) of cobalt onto Cu(111) surface at room temperature from a thoroughly outgassed Co rod. By self-assembly the cobalt form triangular shape nanoislands two-atomic-layer high relative to the Cu surface, whose lateral size varies typically between 5 and 30 nm (Fig. 2.3 a) [10, 11]. Immediately after the cobalt deposition, the sample was inserted into the cryogenic microscope (typically transfer time of 1 minute) and rapidly cooled down to the measurement temperature of 4.6 K to avoid the intermixing with copper. The Co nanoislands with sizes ranging from 5 to 30 nm, provide a surface area ranging from 10 to 400 nm^2, which is big enough to host several molecules or atoms. Moreover, they grow in two different orientations, that have been explained by initial nucleation on the two different threefold hollow sites of Cu(111) surface. One of the nanoisland continues the exact fcc stacking sequence of the Cu(111) substrate (unfaulted nanoisland), whereas the other one presents a stacking fault at the interface being deviated to hcp stacking sequence (faulted nanoisland) as sketched in Fig. 2.3 b [10]. The formation of two-monolayers-high nanoislands starts from the early deposition stages and is due mainly to exchange processes at the edges of nanoislands. Strain relaxation induced in the Cu substrate and in the Co nanoislands have a strong impact in defining the triangular-shape of the nanoislands [12]. The triangular-shape of the Co nanoislands is lost when the self-assembly of cobalt occurs below room temperature, compact irregular nanoislands with dendritic shape developing then [13]. At low temperature, the Co nanoislands are ferromagnetic with strong perpendicular magnetic anisotropy, exhibiting a high coercivity ranging from 1.0 to 1.5 T, depending on island size [14, 15].

2.3 Scanning tunneling spectroscopy

2.3.1 Theoretical background

The ability of STM to image sample surfaces as contours of constant current in the topography mode, allows to visualize and explore the nanoscale world. But there is more information in the tunneling current than just the surface geometry. Changes in current with applied voltage at constant tip-sample separation provide spectroscopic information about the sample surface and any adsorbate located in the barrier region. The high energy resolution at low temperatures (on the meV scale) combined with the high spatial resolution represent the main advantages of scanning tunneling spectroscopy (STS) over spatially averaging techniques like photoemission or

inverse photoemission. The high spatial resolution is of great importance because the impurities or surface defects disturb the local electronic structure.

In the limit of small bias voltages V between the two electrodes, the tunnel process is well described by the Tersoff-Hamann model. For large bias voltages V ($V < \Phi_s, \Phi_t$, where $\Phi_{i=s,t}$ are the work functions of the surface and the tip), where a relative shift of the Fermi levels of the tip and sample occurs, the results of Tersoff-Hamann model is modified to the energy integral:

$$I(V) \propto \int_0^{eV} \rho_t(E - eV)\rho_s(E)T(z, E, eV)dE \tag{2.2}$$

where ρ_t, and ρ_s are the densities of states of the tip and sample, respectively, and all energies are taken with respect to E_F. In Eg. 2.2, the main difficulty is the choice of an adequate transmission coefficient $T(z, E, eV)$. In the framework of a semi-classical WKB-approximation the transmission coefficient can be written as [16]:

$$T(z, E, eV) \propto \exp\left[-2\kappa(E, eV)d\right], \qquad \kappa(E, eV) = \sqrt{\frac{2m}{\hbar^2}[\overline{\Phi} + \frac{eV}{2} - (E - E_{\|})]} \tag{2.3}$$

Here d is the effective tunnel distance (i.e. the distance from the foremost end of the tip to the sample surface plus the radius of a spherical shape tip) and $\overline{\Phi} = (\phi_s + \phi_t)/2$ the average work function. The decay constant $\kappa(E, eV, k_{\|})$ becomes minimal at a certain energy E for states that have a vanishing wave vector parallel to the surface ($k_{\|} = 0$). Therefore, the states at the $\overline{\Gamma}$ -point of the surface Brillouin zone are more pronounced in STS. However, there is another effect related to the exponential dependence of the transmission coefficient T on the effective barrier height Φ_{eff} [where $\Phi_{eff} = (\Phi_s + \Phi_t - e|V|)/2$] that has to be taken into account. If the tip and the sample are far away from each other, their Fermi levels are independent. In the tunneling regime they are in equilibrium, i.e. the Fermi levels of the tip and sample are equal. Applying a bias voltage V leads to a shift of the Fermi level by $|eV|$. At negative sample bias, electrons from the sample in the energy interval from $E_F - eV$ to E_F can tunnel into unoccupied states of the tip (Fig. 2.4 a). For positive sample bias voltage V the situation is reversed and electrons tunnel from occupied tip states into unoccupied sample states (Fig. 2.4 b). In both cases, electronic states close to the Fermi level of the negatively biased

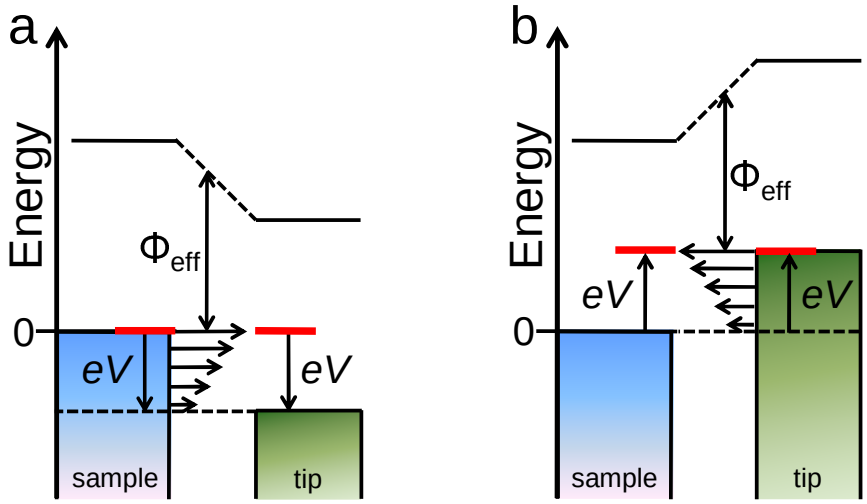

Figure 2.4: Schematic diagram picture revealing the asymmetry of the tunneling junction for a) a negative sample bias and b) a positive sample bias.

electrode will contribute most to the tunneling current, since these electrons "feel" a lower effective barrier height than electrons from states lying lower in energy (indicated in Fig. 2.4 by arrows of different size).

If we assume a constant or weakly varying LDOS of the tip ($\rho_t = constant$) , we obtain from differentiating Eq. 2.2 with respect to V:

$$\frac{dI(V)}{dV} \propto \rho_t(0)\rho_s(eV)T(z,eV,eV) + \int_0^{eV} \rho_t(E-eV)\rho_s(E)\frac{dT(z,E,eV)}{dV}dE \qquad (2.4)$$

The first term shows the proportionality $dI/dV \approx \rho_s(eV)$ while the second term provides a smoothly changing background signal in the case of small bias voltages. From this equation it follows that the measurement of the differential conductance dI/dV gives information about the surface LDOS ρ_s at eV.

2.3.2 Phase detection setup

Experimentally, the energy-dependent differential conductance is measured by stabilizing the tip above the desired location on the surface at specific feedback loop parameters (I and V). Then the feedback loop is switched off, therefore the tip-sample distance is held constant. While the

bias voltage is ramped from the initial to a final value, the tunneling current is measured. The energy-dependent differential conductance [$dI/dV(V)$] can be obtained by either differentiating $I(V)$ curves numerically or by means of a lock-in technique. All the $dI/dV(V)$ spectra shown in this theses were recorded using a lock-in technique, which helps to improve significantly the signal-to-noise ratio. The lock-in detection consists in adding a small voltage modulation of amplitude V_m and frequency ω (from an internal oscillator) to the bias voltage V ($V_m \ll V$). In this way the tunneling current becomes a function of time:

$$I \equiv I[V + V_m \cos(\omega t + \theta)] \tag{2.5}$$

and by applying a Taylor and a Fourier [21] expansion it can be rewritten as:

$$I(V+V_m \cos(\omega t+\theta)) = I(V)+a_0\frac{dI(V)}{dV}V_m \cos(\omega t+\theta)+a_1\frac{d^2I(V)}{dV^2}V_m^2 \cos(2\omega t+\theta)+... \tag{2.6}$$

where a_0 and a_1,... are constants.

A the heart of a lock-in amplifier is a phase-sensitive detector (PSD), which is a circuit that gives preferential treatment to the desired signal based on information about the phase of the signal. The phase-sensitive detector multiplies simultaneously all the above components of the tunneling current (Eq. 2.6) by a signal at the reference frequency and phase shifted by ϕ: $V_{sig}\cos(\omega t + \phi)$. This signal derives from the same internal oscillator that excites the experiment. To detect the first harmonic of the tunneling current the reference frequency is ω and the output of the PSD will be simply the product of two cosine waves:

$$V_{PSD} = V_{sig}\cos(\omega t + \phi) \times [a_0\frac{dI(V)}{dV}V_m \cos(\omega t + \theta)] \tag{2.7}$$

Using the appropriate trigonometric identities, the Eq. 2.7 may be rewritten as follow:

$$V_{PSD} = a_0\frac{V_{sig}}{2}\frac{dI(V)}{dV}V_m[\cos(\theta - \phi) + \cos(2\omega t + \theta + \phi)] \tag{2.8}$$

The above output from the PSD then passes to a low-pass filter which removes the $2\omega t$ com-

ponent, leaving the output of the lock-in amplifier as a DC signal:

$$V_{PSD} = a_0 \frac{V_{sig}}{2} \frac{dI(V)}{dV} V_m [\cos(\theta - \phi)] \tag{2.9}$$

As it can be seen from Eq. 2.9, if the magnitude, V_{sig}, of the reference signal is kept constant, then the DC signal is proportional with the magnitude of the input signal, which is the first derivate of the tunneling current (dI/dV) and with $\cos(\theta - \phi)$, the phase difference between the signal and the lock-in reference oscillator. For maximum output, you have to adjust the phase difference, to either $0°$ or $180°$, a task not very convenient to perform with very weak, noisy input signals. In order to eliminate this phase dependency the modern lock-in amplifiers (as the Stanford SR830 model used here) use a second PSD. If the second PSD multiplies the signal (all the components of tunneling current from Eq. 2.6) with the reference oscillator shifted by $90°$, i.e. $V_{sig} \cos(\omega t + \phi + 90°)$, its low pass filtered output will be:

$$V_{PSD} = a_0 \frac{V_{sig}}{2} \frac{dI(V)}{dV} V_m [\sin(\theta - \phi)] \propto a_0 \frac{V_{sig}}{2} \frac{dI(V)}{dV} V_m \sin(\theta - \phi) \tag{2.10}$$

Now, there are two outputs, one proportional to $\cos(\theta - \phi)$ (Eq. 2.9) and the other proportional to $sin(\theta - \phi)$ (Eq. 2.10). The first output, called X and the second, denoted Y:

$$X = a_0 \frac{V_{sig}}{2} \frac{dI(V)}{dV} V_m \sin(\theta - \phi) \quad Y = a_0 \frac{V_{sig}}{2} \frac{dI(V)}{dV} V_m \cos(\theta - \phi) \tag{2.11}$$

represent the signal as a vector to the lock-in reference oscillator. Often, X is called the *quadrature* component and Y the *in-phase* component. If the phase difference is adjusted to $90°$, the signal given by Y is zero, while the quadrature component of the signal becomes maximum:

$$X = a_0 \frac{V_{sig}}{2} V_m \frac{dI(V)}{dV} \tag{2.12}$$

Therefore, the detection of the first harmonic by the lock-in amplifier will provide the differential conductance $[dI(V)/dV]$ and hence will allow us to probe the local density of states (LDOS) from the area located beneath the tip. Moreover, detection of the second harmonic (for this task it is necessary to feed a frequency of 2ω, into the reference input of the PSD) will provide a spectrum of the second derivative of the tunneling current versus

bias voltage [$d^2I(V)/dV^2$]. If the tunneling current contains contributions originating from inelastic tunneling process, peaks will be generated in the second derivative spectrum. Inelastic tunneling spectroscopy detects the excitation of localized surface plasmon [17], vibration mode of molecules [18] or spin-flips of atoms [19].

Obtaining accurate spectroscopic data depends crucially on the correct adjustment of the phase between the reference signal input and the signal input. This is done by retracting the tip, i.e. making the tunneling resistance infinitely large, adjusting the phase to maximum output, turning the phase by 90° and approaching the tip again. This procedure results in a maximization of the output of the lock-in signal to the resistive part of dI/dV.

The energy resolution in scanning tunneling spectroscopy (STS) can be limited by two sources of instrumental broadening. One of them is the thermal broadening or the thermal smearing of the Fermi-Dirac distribution as the temperature is increased. The second mechanism is related to the amplitude of the voltage modulation employed for the lock-in detection of the differential conductance (Eq. 2.12). The overall energy resolution of STS can be expressed by a smearing instrumental function of width [20]:

$$\Delta E \approx \sqrt{(3.5k_BT)^2 + (1.7V_M)^2} \tag{2.13}$$

All the STS spectra presented in this thesis were acquired at helium temperature of 4.6 K and using the following lock-in parameters: voltage modulation amplitude from 3 mV rms to 5 mV rms and modulation frequency of 7 kHz. At 4.6 K the voltage modulation amplitude V_m will be the dominant contribution limiting the energy resolution, $\Delta E \approx 1.5V_m$. As long as the width of the spectra feature of interest in the differential conductance is greater than the instrumental resolution, the lock-in related broadening can be neglected. The energy resolution for our experiments was therefore between 4 mV and 8 mV.

2.3.3 An example of STS: Shockley surface states

In a metal crystal, the overlapping of atomic orbitals gives rise to electronic bulk states. The energy dispersion of these states form continuous bands separated by a gap in some regions of momentum space. At the metal surface the periodicity of the crystal potential is interrupted. Due to this, the solutions of the Schrödinger equation also exist in the band gap and are restricted to the close vicinity of the surface. Such solutions are called Shockley or Tamm states [26]. Since their energy lie within the gap, they cannot propagate into the crystal and in

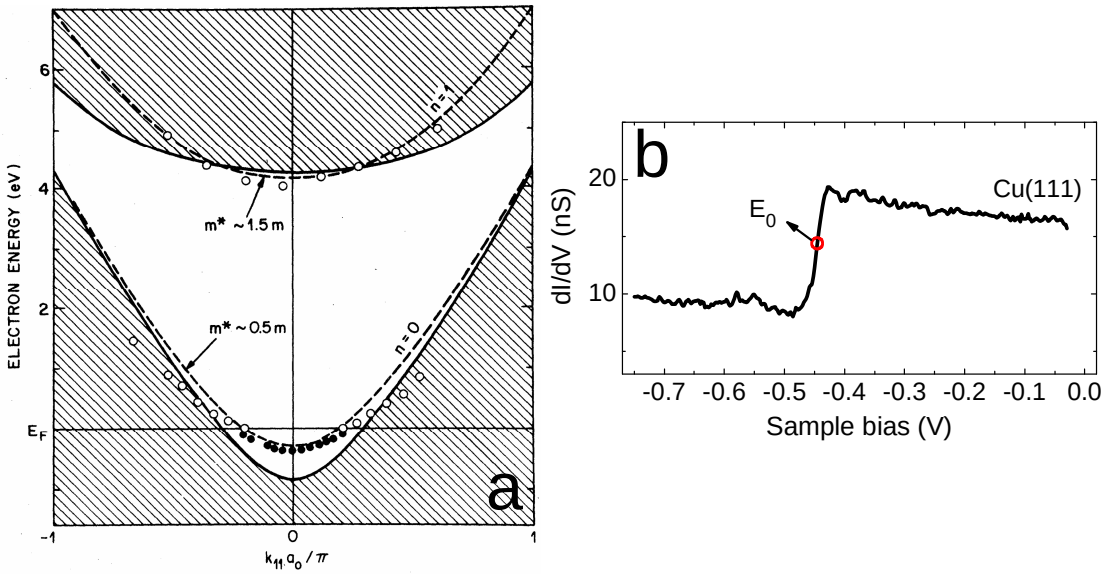

Figure 2.5: a) Dispersion of the $n = 1$ image state and $n = 0$ Shockley surface state near $\overline{\Gamma}$ on Cu(111).The cross-hatched area is the projection of the bulk band structure (from [25]). b) Typical dI/dV spectrum taken on Cu(111) ($T = 4.6$ K). The feedbackloop was opened at $I = 0.5$ nA and $V = -30$ mV.

that sense they form a quasi-two dimensional ($2D$) electron gas. The amplitude of the surface states wave-function decreases exponentially in vacuum and within a few atomic distances to the bulk. In particular the (111) faces of noble metal surfaces (Cu, Ag, Au) host a surface state which has been extensively studied by means of angle-resolved photoelectron spectroscopy (ARPES) [22, 23, 24].

These states, originally observed by Gartland and Slagsvold [27], have a parabolic dispersion of s-p character and appear at the $\overline{\Gamma}$-point of the projected band structure as obtained from calculation and experimental data (Fig. 2.5 a). The step like onset (defined as the middle point of the rise) of the differential conductance detected in STS (Fig. 2.5 b), corresponds to the bottom edge of the parabolic Shockley band, or binding energy, E_0 of surface states. A binding energy of $E_0 = -445$ mV is extracted from the spectrum on Cu(111), in agreement with prior STS measurements [28, 29]. The scattering at defects and steps, as well as the confinement in engineered nanostructures, has been exploited to determine their life time [20, 30, 31, 32] and their scattering coefficient [33]. The confinement, first observed in nanostructures 15 years ago [28, 34, 35], can also be used to measure the quantum mechanical phase [36], or to produce original effects by their interaction with atoms such as a Kondo mirage [37]. The

Shockley surface state was also exploited to evidence the Stark effect in STS [38]. In this thesis, the Cu(111) Shockley surface states have served as a reference spectrum for determining the spectroscopic quality of the tip.

2.3.4 An example of a dI/dV map: confinement of surface states

Since the full differential conductance[$dI/dV(V)$] is carried out at every pixel of a topographic image the complete set of data provides a stack of spectroscopic layers, often called $dI/dV(V,x,y)$ maps. This approach allow a direct correlation of topographic and spectroscopic properties of the sample. In order to get a idea what a dI/dV map means, in the following the spatial distribution of confined Shockley surface states in engineered surface nanocavities is presented. Taking advantage of the capability of STM to manipulate individual atoms, Kliewer et *al.* [39] have constructed a rectangle comprising 28 Mn atoms on Ag(111) surface (the manipulation has been done using the sliding process pioneered by Eigler and Schweizer [40]). As can be seen in the Fig. 2.6, the underlying Ag substrate inside the artificial rectangle shows complex wave patterns generated by the presence of the Mn atoms lying on top of it. This is a quantum effect, the electron on the substrate surface are showing their wave-like behavior, and we are seeing the scattering of these electron waves off the atoms that have been placed on the surface (Fig 2.6).

At negative voltages, the constant current topographies exhibit a rectangular pattern of four maxima within the confining array of Mn atoms (Fig. 2.6 a-p), while at positive voltages, the pattern becomes more complex and varies with bias voltage V (Fig. 2.6 e-h). The lower panels of the figure show the dI/dV maps that were recorded simultaneously with the topographic scans. Below the onset of Ag surface state, $E_0 = -0.67$ V, no corrugation is discernible inside the array (Fig. 2.6 i). In contrast, above E_0 a clear bias dependent wave pattern arises within the structure, while the adatoms are only weak features which conveniently serve to indicate the rectangular boundary (Fig. 2.6 j-p). Consequently dI/dV maps are not directly comparable to constant current maps, a fact clearly visible by comparing both the images from upper and lower panels. This is because the differential conductance dI/dV is approximately proportional to the local density of states (LDOS) at the energy eV, while a constant current topographic image (an STM image) represents a contour of constant integrated local density of states. The dI/dV maps reflect here the stationary LDOS of the nanocavity:

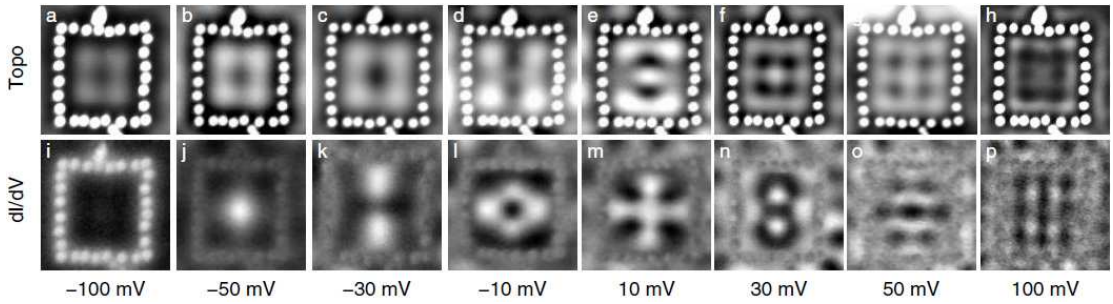

Figure 2.6: Array of 28 Mn atoms forming a rectangle of size 9×10 nm^2. Panels a) - h) show constant-current topographies recorded at the indicated sample voltages. Panels i) - p) are dI/dV maps recorded simultaneously (from [39]).

$$| \psi_{n,m}(x,y) |^2 \propto | \sin(n\pi x/X) \sin(m\pi y/Y) |^2 \tag{2.14}$$

where X and Y are the linear dimensions of the engineered structure, while n and m quantify the radial and the angular motion.

The dI/dV map performed at low energy (Fig. 2.6 j) shows the space distribution of $E_{n=1,m=1}$ level which consists of a single maximum located in the middle of the cavity. At higher energies, two maxima appear along the longer axis of the rectangle (Fig. 2.6 k), corresponding to the $E_{n=1,m=2}$ level. The map, taken at -10 mV (Fig. 2.6 l) and showing four maxima (two along each axis of the rectangle), reflects contributions from both the second ($E_{n=1,m2}$) and third ($E_{n=2,m=1}$) levels. At higher energies the pattern becomes increasingly complex.

2.4 Molecular Evaporator

In this paragraph we briefly present the molecular evaporator used in this thesis for depositing molecules on the metal surfaces. A home built molecular evaporator (Fig. 2.7 a) was used to deposit organic molecular compounds by organic molecular beam deposition in ultra-high vacuum. The cylindrical ceramic crucible tube (9 mm in height and with a 3 mm hole) is held on a macor block by a filament made of tantalum foil (thicknesses of 0.2 mm). The tantalum filament, used for resistive heating, is wound (three turns) around the crucible and connected to the two copper screws that were inserted into the macor support. The macor support together

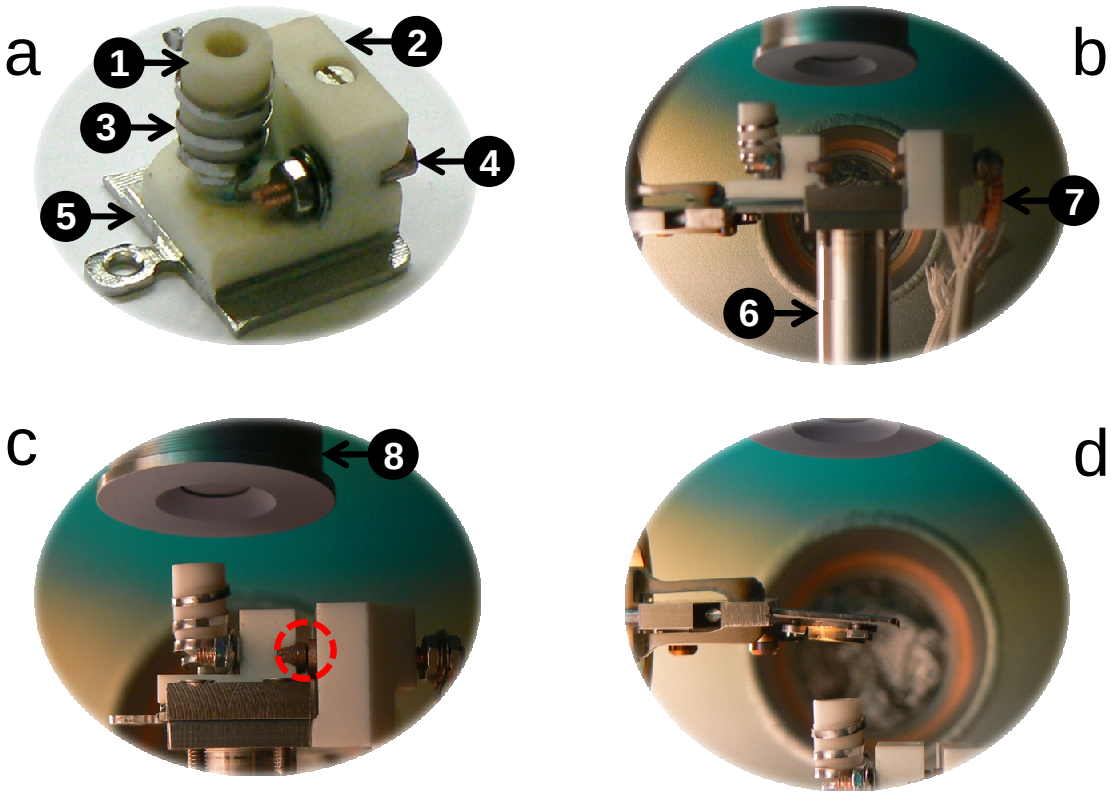

Figure 2.7: Photos illustrating: a) our molecular evaporator with its components: (1) ceramic crucible, (2) macor support, (3) tantalum foil filament, (4) copper screw, (5) Omicron sample plate. b) molecular evaporator inserted on the metallic rigid rod (6), equipped with two copper power leads feedthroughs (7). c) molecular evaporator at a certain distance from quartz balance (8). d) sample above the molecular evaporator.

with the ceramic crucible are fixed on an Omicron sample plate by means of two screws. Inside the intermediary chamber, the molecular evaporator is mounted on a metallic rigid rod which is placed in the center of a DN 40CF flange (Fig. 2.7 b). In this position (Fig. 2.7 c) the copper screws touch the copper power leads feedthrough (encircled area in Fig. 2.7 c) thus providing the electrical connection with the power supply.

A linear drive (manipulator) attached on the DN 40CF flange outside of the UHV chamber allows to manipulate vertically the molecular evaporator. This special design of our molecular evaporator allows quick and easy crucible replacement or refilling as it does not require breaking the vacuum in the main chamber. Moreover it can be introduced inside the UHV environment after baking the main chamber. This is very useful when dealing with powders that cannot

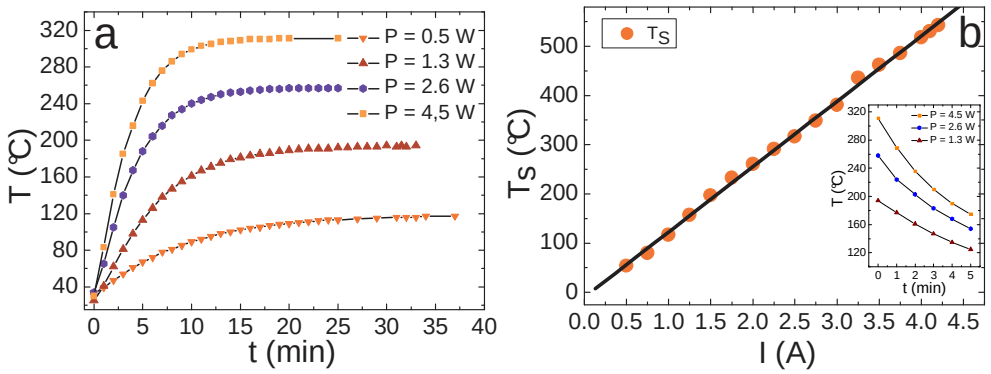

Figure 2.8: a) Temperature of the crucible as a function of time for several values of the electric power [$P = I \times U$ (W)]. b) The saturation temperature as function of the current intensity through the filament. Inset: temperature versus time after shutting down the power supply.

withstand the bakeout temperature of 120°C for the main chamber.

Before molecular deposition, the temperature is varied by applying a current to a tantalum filament wound around the crucible. The temperature calibration versus current has been done in vacuum ($P = 1 \times 10^{-7}$ mbar) using a K type (Chromel-Alumel) thermocouple introduced inside the crucible. The current through the tantalum filament was increased in steps of 0.25 A up to a value of 4.25 A. For each value of the electric power [$P = I \times U$ (W)], the temperature of the crucible needs approximately twenty minutes ($t = 20$ min) to reach a saturation value (Fig. 2.8 a). The saturation temperature increases linearly when increasing the intensity of the current through the filament (Fig. 2.8 b). The above calibration shows that temperatures between 30°C and 550°C (the maximum temperature reached during the calibration) can be reached. When the power supply is set to zero, the temperature of crucible decreases to typically about 100°C in the first five minutes as can be seen in the inset of Fig. 2.8 b, while it takes about forty minutes to go back to room temperature.

The molecular deposition has been done in the following way: $1.$) The molecular evaporator with the molecules heated to the desired temperature is kept at a given distance from a quartz balance (Fig. 2.7 c) to adjust the deposition rate. $2.$) Once the desired deposition rate is achieved, the molecular evaporator is moved down and the crystal is inserted between the quartz balance and the molecular evaporator for the deposition (Fig. 2.7 d). The crystal-molecular evaporator distance is fixed at the same value as the previous molecular evaporator-quartz balance distance. Monolayer or sub-monolayer can be achieved in this way with typically exposition times of 2 to 20 seconds.

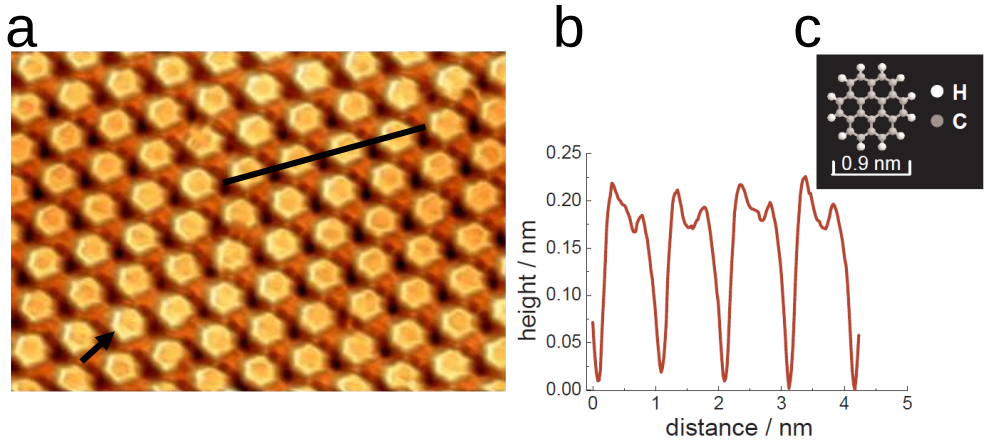

Figure 2.9: a) STM topographic image of a close packed coronene monolayer on Au(111), recorded at 77 K (V=0.5 V, I=1.0 nA, 10×7 nm^2) b) Profile along the black line in (a). c) Structure model for coronene.

The molecular evaporator has been tested by depositing coronene on the Au(111) crystal. Coronene is a polycyclic aromatic hydrocarbon consisting of seven benzene rings (Fig. 2.9 c). In ultra high vacuum (P=2×10^{-9} mbar), coronene starts to sublimated at crucible temperature of 100-110°C. For an exposition time of 10 seconds, coronene self-assembles in a densely packed monolayer with hexagonal lattice structure (Fig. 2.9 a). A submolecular high-resolution STM image acquired at nitrogen temperature (77 K) clearly proves that the coronene posses a nearly flat orientation on the surface (Fig. 2.9 a). The molecules behave as hexagonal shape in agreement with previous studies [41]. A line profile along four molecules on the monolayer (Fig. 2.9 b) reveals an apparent height of the molecule of 0.2 nm and a lattice spacing of 1.1 nm $\pm$ 0.02 nm in agreement with previous studies [42, 43, 44]. Each molecule has a hollow center with a maximum signal in the outer ring. For the back and forth scan, the left side of the molecules appears brighter (marked by the black arrow in the Fig. 2.9 a) than the right side. The same effect was also seen for coronene deposited on Ag(111) [43]. It was suggested that the molecule is not adsorbed in a planar geometry, but is somewhat tilted [43].

In conclusion our homebuilt molecular evaporator can be employed in thermal sublimation or evaporation of different compounds with a variety of evaporation temperatures.

2.5 Related deposition techniques

The studies of molecules on surfaces in UHV, deposited by an organic molecular beam, have the advantage of providing both, layer thickness control and an atomically clean substrate and environment compared to any wet chemistry deposition techniques [45]. Nevertheless, this deposition technique is often inadequate for large supramolecular entities as it leads to their decomposition before sublimation of the polycrystalline powder occurs. Therefore, an alternative approach is to use deposition methods from a solution such as: *immersion* (the sample is immersed in solution for different times and then left drying in air), *drop casting* (a droplet of solution is applied onto the surface and the solvent is slowly evaporated) and *spin coating* (a droplet of solution is placed on the substrate that is rotated in a typical experiment at a rate of 2000 rotations per minute for a certain time). During my thesis I used frequently these techniques to deposit various organo-metallic compounds in view to study their electronic and magnetic properties at a single molecular level. These deposition techniques however do not fulfill the required quality standards. Either the organo-metallic compounds have decomposed in fragments under the action of the solvent or they self-assembled in clusters, making their investigation impossible. However, organometallic complexes with improved stability can be deposited on the surfaces using the above mentioned deposition techniques. In the following an atomic force microscopy study (AFM) is presented focusing on a σ-alkynyl platinum(II) terpyridine complex (Fig. 2.10 d), that was synthesized by the chemists from Ecole Europeenne de Chimie Polymeres et Materiaux from Strasbourg in collaboration with my colleagues of the Organic Material Department.

Owing to the intense phosphorescence in the visible region of the electromagnetic spectrum, luminescent platinum-terpyridine functional material, are being widely used as electroluminescent thin films in organic light-emission devices [46, 47]. However, the fabrication of nanoscale optoelectronic devices requires nanostructured, one-dimensional ($1D$) morphologies. The main challenge in assembling large molecules into $1D$ materials lies in balancing the molecular assembly for growth along the π-stacking direction against the lateral association of side chains. The former dictates the $1D$ morphology of self-assembly, whereas the latter favors the formation of bulk assemblies. An effective way to prevent or minimize the lateral growth of molecular assembly due to side chain association is the sol-gel processing. As it was shown, our σ-alkynyl platinium(II) terpyridine complex is a very good gelator of dodecane, whereas in solid state it is liquid-crystalline over a large temperature range [48]. The diluted dode-

cane gel ($c = 0.08$ mmolL^{-1}) of the complex deposited by drop-casting on a freshly cleaved mica substrate was found to self-assembled onto molecular nanofibers with lengths of several nanometers, with no apparent orientational order (Fig. 2.10 b) and an average height of 2 nm (Fig. 2.10 c). On the highly ordered pyrolytic graphite (HOPG), the molecular nanofibers follow the preferential crystallographic directions of the underlying substrate (Fig. 2.10 e). The three-fold symmetry of the segment pattern is particularly visible at intercepts where the molecular nanofibers form angles of $60°$ and $120°$ to each other. The cross-sections show the presence of two types of molecular nanofibers corresponding to two different molecular heights, namely 2 nm and 4 nm (Fig. 2.10 f). The molecular modeling (Fig. 2.10 d) show that the 2 nm high nanofibers can be considered to be made of single molecular layers that lie flat on the surface. The 4 nm high nanofibers are made of such piled up molecular layers. The core of a single-molecular wire consists of complexes that strongly interact through platinum-platinum and platinum-acetyline contacts. The self-assembly in elongated nanofibers is driven by strong directional intermolecular interactions such as hydrogen bonding. The formation of straight molecular nanofibers on HOPG is due to alkyl chains that aligned with their molecular axis along one of the symmetry axes of the graphite [49]. As can be seen from the cross-sections (Fig. 2.10 c and 2.10 f), the nanofibers show lateral extension of several tens of nanometers. Since the full lateral extension of a single molecular wire is only about 3 nm, it can be concluded that the nanofibers are made of monolayer and bilayer stripes that comprise several molecular wires in the lateral xy direction.

In conclusion the organogel σ-alkynyl platinum(II) terpyridine complex deposited by drop casting on both mica and HOPG give rise to the formation of well-organized nanofibers several hundred nanometers in lengths thus, being a potential candidate for the fabrication of nanoscale optoelectronic devices.

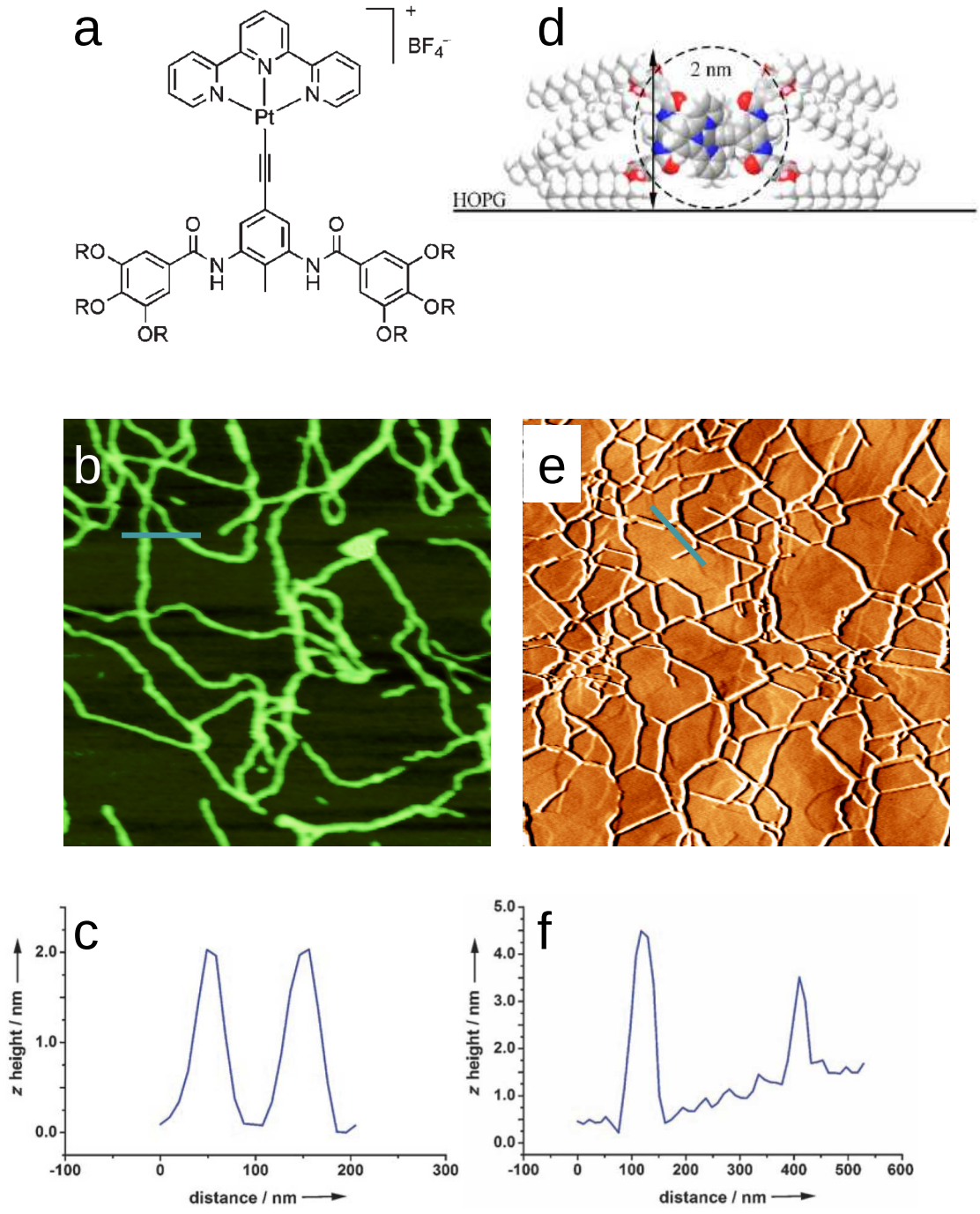

Figure 2.10: a) Schematic molecular structure of σ-alkynyl platinium(II) terpyridine complex. b) AFM tapping mode image ($2.15\ \mu$m $\times$ $2.15\ \mu$m) of a dried dilute gel of σ-alkynyl platinium(II) terpyridine complex in dodecane ($c = 0.08$ mmolL^{-1}) deposited on mica. c) Cross-section along the blue line in (b). d) CPK model of the cross-section of platinum fiber deposited on HOPG. The length of the arrow and the circle diameter are 2 nm. e) AFM tapping mode image ($5\ \mu$m $\times$ $5\ \mu$m) of a dilute gel of σ-alkynyl platinum(II) terpyridine complex in dodecane ($c = 0.08$ mmolL^{-1}) deposited on HOPG. f) Cross-section along the blue line in (e).

Bibliography

[1] M. E. Taylor. Dynamics of piezoelectric tube scanners for scanning probe microscopy. Rev. Sci. Instrum. **64**, 154 (1993).

[2] C. J. Chen, *Introduction to Scanning Tunneling Microscopy*. Oxford University Press, Oxford (1993).

[3] G. Binnig, H. Rohrer, Ch. Gerber, and E. Weibel. Surface studies by scanning tunneling microscopy. Phys. Rev. Lett. **49**, 57 (1982).

[4] A. M. Baro, G. Binnig, H. Rohrer, Ch. Gerber, E. Stoll, A. Baratoff, and F. Salvan. Real-space observation of the 2×1 structure of chemisorbed oxygen on Ni(110) by scanning tunneling microscopy. Phys. Rev. Lett. **52**, 1304 (1984).

[5] G. Binnig, H. Rohrer, Ch. Gerber, E. Weibel. (111) facets as the origin of the reconstructed Au(110) surfaces. Surface Science **131**, L379 (1983).

[6] G. Binnig, H. Rohrer, Ch. Gerber, E. Weibel. 7×7 reconstruction on Si(111) resolved in real space. Phys. Rev. Lett. **50**, 120 (1983).

[7] D. M. Eigler, C. P. Lutz, and W. E. Rudge. An atomic switch realized with a scanning tunneling microscope. Nature **352**, 600 (1991).

[8] J. R. Hahn and W. Ho. Single molecule imaging and vibrational spectroscopy with a chemically modified tip of a scanning tunneling microscope. Phys. Rev. Lett. **87**, 196102 (2001).

[9] S. W. Hla, K. F. Braun, V. Iancu, and A. Deshpande. Single atom extraction by scanning tunneling microscope tip-crash and nanoscale surface engineering. Nano Lett. **6**, 1997 (2004).

[10] J. De La Figuera, J. E. Prieto, C. Ocal, and R. Miranda. Scanning tunneling-microscopy study of the growth of cobalt on Cu(111). Phys. Rev. B **47**, 13043 (1993).

[11] A. L. Vazquez de Parga, F. J. Garcia-Vidal, and R. Miranda. Detecting electronic states at stacking faults in magnetic thin films by tunneling spectroscopy. Phys. Rev. Lett. **85**, 4365 (2000).

[12] N. N. Negulyaev, V. S. Stepanyuk, P. Bruno, L. Diekhöner, P. Wahl, and K. Kern. Bilayer growth of nanoscale Co islands on Cu(111). Phys. Rev. B **77**, 125437 (2008).

[13] M. Ö. Pedersen, I. A. Bonicke, E. Lægsgaard, I. Stensgaard, A. Ruban, J. K. Nørshov, and F. Besenbacher. Grown of Co on Cu(111): subsurface growth of trilayer Co islands. Surf. Sci. **387**, 86 (1997).

[14] O. Pietzsch, A. Kubetzka, M. Bode, and R. Wiesendanger. Spin-polarized scanning tunneling spectroscopy of nanoscale cobalt islands on Cu(111). Phys. Rev. Lett. **92**, 057202 (2004).

[15] J. Camarero, J. J. de Miguel, V. Raposo, A. Hernando, and R. Miranda. Influence of film morphology on perpendicular magnetic anisotropy. Phys. Rev. B **64**, 125406 (2001).

[16] R. Wiesendanger. *Scanning Probe Microscopy and Spectroscopy. Methods and Application*. Cambridge University Press, Cambridge (1994).

[17] R. Berndt, J. K. Gimzewski, and P. Johansson. Inelastic tunneling excitation of tip-induced plasmon modes on nobel metal surfaces. Phys. Rev. Lett. **67**, 3796 (1991).

[18] W. Ho. Single-molecule chemistry. J. of Chem. Phys. **117**, 11033 (2002).

[19] A. J. Heinrich, J. A. Gupta, C. P. Lutz, and D. M. Eigler. Single-atom spin-flip spectroscopy. Science **306**, 466 (2004).

[20] J. Kröger, L. Limot, H. Jensen, R. Berndt, S. Crampin, and E. Pehlke. Surface state electron dynamics of clean and adsorbate-covered metal surfaces studied with the scanning tunnelling microscope. Prog. Surf. Sci. **80**, 26-48 (2005).

[21] A. M. Russell, and D. A. Torchia. Harmonic analysis in systems using sensitive detectors. Review of Scientific Instruments. **33**, 442 (1962).

[22] S. D. Kevan. Evidence for a new broadening mechanism in angle resolved photoemission for Cu(111). Phys. Rev. Lett. **50**, 526 (1983).

[23] K. Giesen, F. Hage, F. J. Himpsel, H. J. Riess, and W. Steinmann. Two-photon photoemission via imagine-potential state. Phys. Rev. Lett. **55**, 300 (1985).

[24] F. Reinert, G. Nicolay, S. Schmith, D. Ehm, and W. Shen. Direct measurements of L-gap surface states on the (111) face on nobel metal by photoelectron spectroscopy. Phys. Rev. B **63**, 115415 (1990).

[25] N. V. Smith. Phase analysis of image states and surface states associated with nearly-free-electron band gaps. Phys. Rev. B **32**, 3549 (1985).

[26] W. Schockley. On the surface states associated with a periodic potential. Phys. Rev. Lett. **56**, 317 (1939).

[27] P. O. Gartland, and B. J. Slagsvold. Transitions conserving parallel momentum in photoemission from the (111) face of copper. Phys. Rev. B **12**, 4047 (1975).

[28] M. F. Crommie, C. P. Lutz and D. M. Eigler. Imaging standing waves in a two-dimensional electron gas. Nature **363**, 524 (1993).

[29] J. Kliwer, R. Berndt, E. V. Chulkov, V. M. Simkin, P. M. Echenique, and S. Crampin. Dimensionality effect in the life time of surface states. Science **288**, 1399 (2000).

[30] G. Hörmandinger. Imaging of the Cu(111) surface state in scanning tunneling spectroscopy. Phys. Rev. B. **49**, 13897 (1994).

[31] L. Bürgi, O. Jeandupeux, H. Brune and K. Kern. Probing hot-electron dynamics at surfaces with a cold scanning tunneling microscope. Phys. Rev. Lett., **82**, 4516 (1999).

[32] S. Crampin, J. Kröger, H. Jensen, and R. Berndt. Phase coherence length and quantum interference patterns at step edges. Phys. Rev. Lett. **95**, 029701 (2005).

[33] E. J. Heller, M. F. Crommie, C. P. Lutz and D. M. Eigler. Scattering and absorption of surface electron waves in quantum corrals. Nature, **369**, 464 (1994).

[34] Y. Hasegawa and Ph. Avouris. Direct observation of standing wave formation at surface steps using scanning tunneling spectroscopy. Phys. Rev. B. **71**, 1071 (1993).

[35] M. F. Crommie, C. P. Lutz, and D. M. Eigler. Confinement of electrons to quantum corrals on a metal surface. Science **262**, 218 (1993).

[36] C. R. Moon, L. S. Mattos, and B. K. Foster. Quantum phase extraction in isospectral electronic nanostructures. Science **319**, 782 (2008).

[37] H. C. Manoharan, C. P. Lutz, and D. M. Eigler. Quantum mirages formed by coherent projection of electronic structure. Nature **403**, 512 (2000).

[38] J. Kröger, L. Limot, H. Jensen, and R. Berndt. Stark effect in Au(111) and Cu(111) surface states. Phys. Rev. B. **70**, 033401 (2004).

[39] J. Kliewer, R. Berndt and S. Crampin. Scanning tunneling spectroscopy of electron resonators. New Journal of Physics **67**, 193402 (2001).

[40] D. M. Eigler, and E. G. Schweizer. Positioning single atoms with a scanning tunneling microscope. Nature **344**, 524 (1990).

[41] K. Walzer, M. Sternberg, and M. Hietschold. Formation and characterization of coronene monolayers on HOPG(0001) a,nd MoS_2(0001): a combined STM/STS and tight-binding study. Surface Science **415**, 376 (1998).

[42] S. Uemura, M. Sakata, I. Taniguchi, C. Hirayama, and M. Kunitake. In situ observation of coronene epitaxial adlayers on Au(111) surfaces prepared by the transfer of Langmuir films. Thin Solid Films **409**, 206 (2002).

[43] M. Lackinger, S. Griessl, W. M. Heck, and M. Hietschold. Coronene on Ag(111) investigated by LEED and STM in UHV. J. Phys. Chem. B **106**, 4482 (2002).

[44] W. A. English, and K. W. Hipps. Stability of a surface adlayer at elevated temperature: coronene and heptanoic acid on Au(111). J. Phys. Chem. C **112**, 2026 (2008).

[45] S. R. Forrest. Ultrathin organic films grown by organic molecular beam deposition and related techniques. Chem. Rev. **97**, 1793 (1997).

[46] D. R. McMillin, and J. J. Moore. Luminescence that lasts from $Pt(trpy)Cl^+$ derivatives (trpy=2,2',6,2"-terpyridine). Coord. Chem. Rev. **229**, 113 (2002).

[47] W. Lu, B. H. Mi, M. C. W. Chan, Z. Hui, C. M. Che, N. Zhu, and S. T. Lee. Light emitting tridentate cyclometalated platinium(II) complexes containing σ-alkynyl auxiliaries: tuning of photo and electrophosphorescence. J. Am. Chem. Soc. **126**, 4958 (2004).

[48] F. Camerel, R. Ziesel, B. Donnio, D. Guillon, M. Schmutz, C. Iacovita, and J. P. Bucher. Formation of gels and liquid crystal induced by $Pt{-}Pt$ and $\pi{-}\pi^*$ interaction in luminescent σ-alkynyl platinium(II) terpyridine complexes. Angew. Chem. Int. Ed. **46**, 2659 (2007).

[49] S. De Feyter, and F. C. De Schryver. Two-dimensional supramolecular self-assembly probed by scanning tunneling microscopy. Chem. Soc. Rev. **32**, 139 (2003).

Chapter 3

Addressing cobalt-phthalocyanine molecules on metal surfaces

This chapter is entirely dedicated to cobalt-phthalocyanine molecules. It begins with an overview of previous STM and STS studies of cobalt-phthalocyanine molecule. The results of this thesis regarding the cobalt-phthalocyanine molecules in monolayer and submonolayer coverage regime on Au(111) and Cu(111) surfaces, respectively are then presented. Some insight on the interaction occurring at the cobalt phthalocyanine-Cu(111) metal interface is obtained by comparing the STM and STS results with density function theory calculations. The second part of the chapter focuses on the adsorption of cobalt-phthalocyanine on cobalt nanoislands grown on Cu(111). After summarizing the electronic properties of these nanoislands as revealed by STS, results on growth and electronic properties of cobalt-phthalocyanine molecules on these nanoislands are presented. In the last section of the chapter, the results are summarized.

3.1 Cobalt-Phthalocyanine on coinage surfaces

3.1.1 The Cobalt-Phthalocyanine molecule

In this thesis we performed low-temperature STM and STS investigations of phthalocyanine-based organo-metallic compound, namely cobalt-phthalocyanine (Fig. 3.1). The phthalocyanine microcycle is composed of four isoindole groups, each consisting of a pyrrole group coupled to a benzene ring. These four isoindole groups are in turn connected via bridging nitrogen to

form a ring-like structure. The void left in the center of the molecule can be populated with a metal atom, which in our case is a cobalt one. The first metal-phthalocyanine compound, with a copper metal atom in the middle of the microcycle, was synthesized by the swiss chemists H. de Diesbach and E. von der Weid in 1927 [1]. Its chemical structure was determined for the first time by the X-ray diffraction technique in 1936. The diagonal passing through the central metal ion and the two central nitrogen atoms measures 1.5 nm (red dotted double arrow in Fig. 3.1). The family of the metal-phthalocyanines is a versatile class of medium size organo-metallic compounds, which have attracted considerable attention in nanoscience and material engineering. Because of their exceptional chemical and thermal stability as well as their conducting properties, they are used in many industrial applications [2, 3]. They are important compounds for optical and organic electronic devices such as organic light-emitting diodes, thin film transistors, and solar cells [4, 5]. Particularly, cobalt phthalocyanine (CoPc) is often used in gas sensing [6] and optoelectronics [2]. From a microscopic point of view, the copper-phthalocyanine (CuPc) molecule, has benefited from all the progress in microscopy for nearly a century. In 1957, using a field-emission microscope, E. Müller succeeded in his laboratory at the University of Pennsylvania to image some copper-phthalocyanine molecules deposited on a tungsten tip [7]. Further, H. Hashimoto obtained in 1974 in his laboratory of the University of Tokyo a more detailed image of CuPc, by imaging an ultrathin CuPc crystal with a transmission electron microscope. In 1987, at the IBM research laboratory in Zurich, the CuPc became the first molecule ever imaged with the new invented scanning tunneling microscope. Taking advantage on its high-spatial resolution, J. K. Gimzewski obtained the first image of an individual molecule [8]. This image of CuPc looks similar to that obtained by E. Müller thirty years ago. However, in this case the experiment is reversed: the molecule is no longer on the tip, but on the surface. Since then STM investigation of CuPc was performed by many groups with varying coverage on different substrates [9, 10, 11]. The CoPc molecule was imaged by Hipps et *al.* [12, 13]. They demonstrated the growth of a well ordered mixed monolayer of CoPc and CuPc on Au(111), in which the two molecules could be distinguish by the apparent height of their central metal atom: the Cu^{2+} ion appears has a ≈ 0.1 nm depression while the Co^{2+} ion comes out as a ≈ 0.15 nm protrusion which means that it has an enhanced conductivity compared to copper, resulting from orbital-mediated tunneling through the half-filled d_{z^2} orbital of the Co^{2+} ion. The CoPc molecule has been employed to study the self-assembled phenomena in the mixed two-dimensional monolayers on different surfaces [14, 15]. When the CoPc molecules adsorb on vicinal Au(788) surface they give rise to the

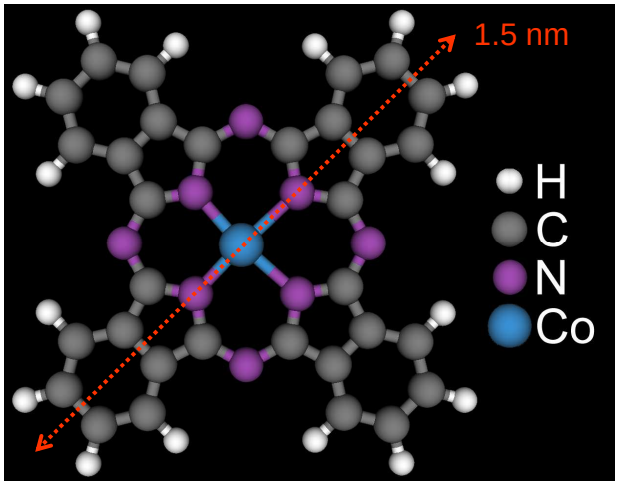

Figure 3.1: Structure model of cobalt-phthalocyanine. The red dotted double arrow indicates the diagonal of 1.5 nm.

formation of long molecular stripes along the gold steps [16].

The electronic properties of a CoPc molecule on a surface have been first studied by STS at room temperature [17]. The tunneling I-V characteristics were measured for small islands and binary monolayer films of CoPc and Co-tetraphenylporphyrin adsorbed on Au(111) surface and dI/dV spectra were calculated numerically from I. The local density of states of the molecules were discussed on the basis of spatially averaged dI/dV spectroscopy. Due mainly to the thermal drift it was very difficult to elucidate the spatial distribution of the local density of states within a single molecule. Moreover the thermal broadening of the Fermi-Dirac function at room temperature (as high as 90 meV based on Eq. 2.13 from § 2.3.2) smears the resonances in the spectra and therefore the fine structure of the electronic states cannot be correctly interpreted. To overcome these difficulties, Takada et *al.* have kept the CoPc molecules deposited on Au(111) and Co(100) single crystals at 5 K during the STS investigation [18]. In this way they have provided the first accurate spectroscopic study on single CoPc molecule. The dI/dV spectra of CoPc molecule on Au(111) surface showed four peaks corresponding to the lower lying occupied molecular orbital (HOMO-1), the highest occupied molecular orbital (HOMO), the lowest unoccupied molecular orbital (LUMO) and the d orbital of the cobalt atom. Takada et *al.* claimed that the CoPc molecule adsorbed on the Cu(100) surface showed as well adsorption induce states (§ 3.1.3). Spin-scattering process manifested themselves as a Kondo-resonance in STS was reported for the paramagnetic CoPc molecule adsorbed on both

surface or monoatomic steps of Au(111) with a high Kondo-temperature ranging from 150 K to 550 K [19, 20]. Employing *spin excitation spectroscopy* [21], Chen et *al.* have found that the CoPc molecules form one-dimensional antiferromagnetic chains in the thin film [22].

Our investigation on single CoPc molecules were performed by following a well defined protocol. In order to get familiar with the CoPc molecule, the monoloyer-coverage regime on Au(111) surface was first investigated. In the next step the CoPc molecules have been deposited with submonolayer coverage onto Cu(111). The STM image of individual molecules were used to determine the integrity and the orientation of the molecules. The STS spectra were acquired in different parts of the molecule. Its adsorption site and the electronic properties was then discussed in view of first principle calculations based on density functional theory. Finally, CoPc molecules deposited on cobalt nanoislands grown on Cu(111) surface have been studied. In the final step, the spin-polarized properties of individual CoPc molecules adsorbed on cobalt nanoislands have been explored using a spin-polarized tip (Chapter 5).

3.1.2 Monolayer of CoPc on Au(111) surface

The CoPc molecules were purchased from Alfa Aesar and had a 95% purity. Prior to deposition the purification of the source material is essential for ensuring a molecular flux with negligible impurities. In our case the CoPc powder was purified by multiple sublimations. This consists in heating the molecules to a temperature of 480°C (slightly below the sublimation temperature) and measuring the evaporation with the quartz balance. This cycle was repeated until a constant and reproducible evaporation rate could be observed. After three days, a flux of 0.1 ng/s at a distance of 1 cm from the quartz balance could be repeatedly detected. The high-ordered and defect-free CoPc monolayer was produced by evaporating CoPc onto the Au(111) substrate that was kept at room temperature. Figure 3.2 a shows a STM image of a monolayer on Au(111) observed at 77 K. The image is a part of an adlayer, which extends up to 400×400 nm^2. A monolayer is defined as the amount of deposited CoPc that entirely covers the substrate surface (one CoPc molecule covers the area of 12 gold atoms). A zigzag pattern can be clearly seen as a modulation of the monolayer contrast in the STM image. This zigzag pattern stems from the Au(111) surface reconstruction that provides evidence that the Au(111) surface reconstruction is not destroyed or lifted upon deposition of the CoPc molecules. The surface reconstruction for the Au(111) is driven by the surface energy minimization and the large tensile stress in the Au surface layer, leading to a hexagonal overlayer 4.5% denser than a (111) plane of the bulk. The

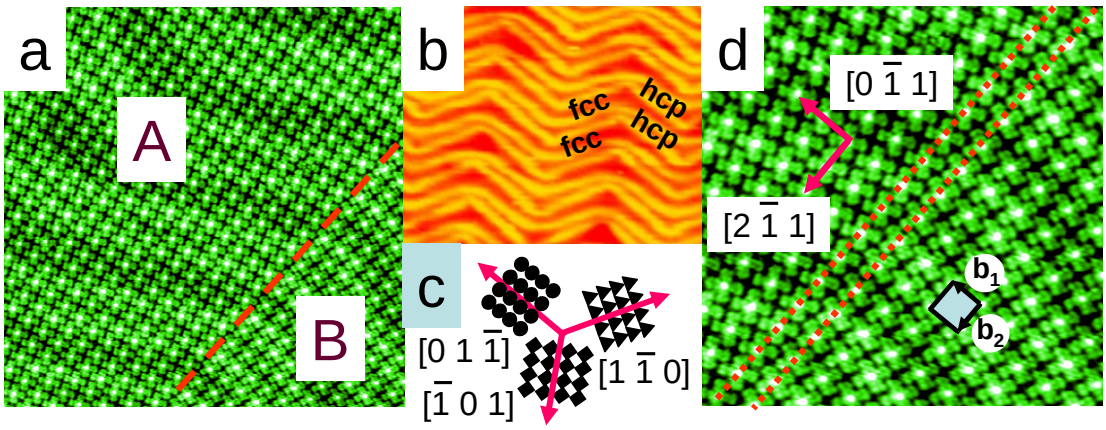

Figure 3.2: a) STM image of CoPc molecules adsorbed on Au(111). The dashed line indicate the domain boundary between two orientations: [A] and [B] (Scan size: 27 nm$\times 27$ nm; Tunneling parameters: $V = -0.8$ V, $I = 0.1$ nA). b) STM image showing the herringbone reconstructed Au(111) surface with alternating fcc and hcp stacking domains (Tunneling parameters: $V = 0.5$ V, $I = 1$ nA). c) Sketch of three symmetry-equivalent domains. d) The two line defects are marked with dotted lines. The two vectors, b_1 and b_2 forming an angle of $90°$ identify the unit cell for the square structure (Scan size: 15 nm$\times 15$ nm; Tunneling parameters: $V = -0.8$ V, $I = 0.1$ nA).

surface energy minimization produces a contraction of the interatomic distance of the surface atoms along the $[1\bar{1}0]$ direction from the bulk value of 2.89 Å to a average value of 2.75 Å. As a consequence, 23 gold atoms of the surface layer are arranged over 22 bulk lattice sites in $[1\bar{1}0]$ direction. The stress-induce uniaxial contraction of the surface along $[1\bar{1}0]$ direction, plus a longer range, mesoscopic structure of the rotated uniaxial domains that appears to further reduce isotropically the stain [23], leads to a $23 \times \sqrt{3}$ overlayer structure and the creation of alternating domains of hexagonal close packed (hcp) and face centered cubic (fcc) stacking (Fig. 3.2 b). The regions between fcc and hcp stacking domains of the topmost atomic layer are separated by soliton walls which contains stacking fault lines, often called discommensuration lines. They possess unique soliton like properties providing efficient diffusion channels for mass transport [24]. The soliton wall regions constitute the bright ridges that appear as 0.3 Å protrusions in STM images. The direction of the elevated ridges along the $[11\bar{2}]$ direction is periodically rotated by $120°$, forming the characteristic herringbone (chevron) pattern [25].

A STM image of the CoPc monolayer (Fig. 3.2 d) gives directly the real-space configuration of individual molecules and the periodic structure of the organic monolayer. The CoPc molecules

are seen to adsorb with the molecular plane parallel to the surface, in analogy with other studies on phthalocyanine monolayers [26, 28, 29]. Moreover, the observed CoPc molecules are recognized as a four-lobed pattern (related to the four aromatic rings) with a protrusion at the center (ascribed to half-filled d_{z^2} orbital of the Co^{2+}) [12, 13]. Because of the three-fold symmetry of the Au(111) substrate, three symmetry-equivalent domains of the monolayer can be observed in STM results [13, 30]. Figure 3.2 c presents a sketch of the three symmetry-equivalent domains aligned along the three symmetric directions. L. Gao et *al.* have experimentally and theoretically found two adsorption configurations of FePc molecules deposited on Au(111) surface in a submonolayer regime [31]. The theoretical calculations performed by them have indicated that the iron atom of the molecule sits either in top or bridge sites of the Au(111) surface. Later, Hu et *al.* have theoretically demonstrated that MPc (M=Fe, Ni, Cu, Mn) molecules adsorb on Au(111) surfaces in two stable and different adsorption configurations [32]. The favorable adsorption site is the hcp hollow site for FePc, NiPc, and CoPc, whereas it is the top site for MnPc. The other stable configuration which exist simultaneously was found to be either the top site for FePc, NiPc, CoPc or the hcp hollow site for MnPc respectively. In accordance with these observations, it can be concluded that the CoPc molecules can potentially adsorb in six different orientation-domains on Au(111) (three symmetric domains multiplied by two different adsorption configurations in which the central cobalt atom sits on either a top or a bridge site). Normally, there are only symmetric domain on a large terrace, i.e. the density of the symmetric domain boundary is rather low in the well-ordered monolayer. The large scale STM image (Fig. 3.2 a) shows a symmetric domain, which consists of two molecular orientation-domains, [A] and [B]. The domain boundary is indicated by the dash line in Fig. 3.2 a. A close inspection in the ordered monolayer shows that there is a line defect, marked by the double dotted lines in Fig. 3.2 d.

A quadratic periodic structure of the CoPc monolayer was found in the STM image in which the sides of the unit cell are very closely oriented to the $[21\bar{1}]$ and $[01\bar{1}]$ crystalline directions of the Au(111) lattice. This is illustrated in Fig. 3.2 d by solid arrows. A square unit cell is marked by the blue square in which the black arrows (b_1 and b_2) represent the unit cell vectors of the superstructure. Fourier transformation of several images provides a mean value for the unit cell parameters of b_1=15 $\pm$ 1 Å and b_2=15 $\pm$ 1 Å with an angle of $\beta = 90 \pm 5°$. Similar structures have been reported in previous studies concerning, e.g., iron phthalocynanine (FePc) on Au(111), Cu(111) and graphite [26, 29, 33], palladium phthalocyanine (PdPc) on graphite [34], metal-free phthalocyanine (H_2Pc) on graphite [35]. According to the epitaxial

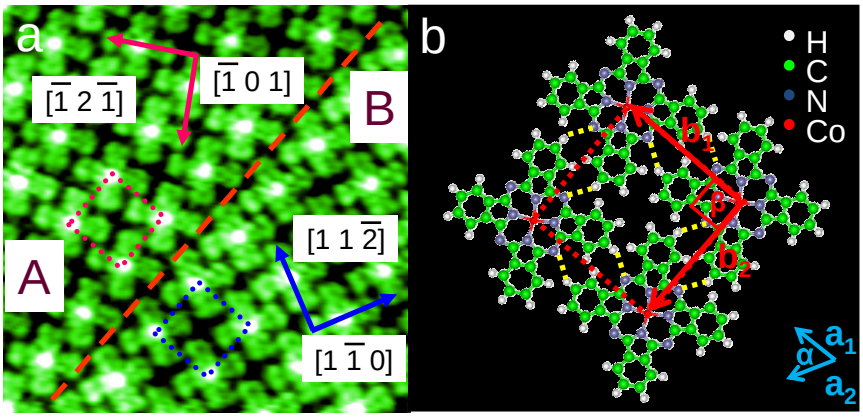

Figure 3.3: a) High-resolution STM image of CoPc molecules adsorbed on Au(111) surface showing the orientations of molecules in both of the orientation-domains. The dashed line indicate the domain boundary between the two orientation-domains: [l_1] and [l_2] (Scan size: 8 nm×8 nm; Tunneling parameters: $V = -0.8$ V, $I = 0.1$ nA). b) The model for the unit cell of CoPc molecule monolayer on Au(111). Possible attractive electrostatic interactions between the neighboring molecules are indicated by the dotted lines.

relation between the substrate and the adlayer lattice, the molecular epitaxy is classified into three, namely commensurism, coincidence and incommensurism [36, 37]. This relation of the interface can be described using the unit lattice vectors of the substrate, $\overrightarrow{a_1}$, $\overrightarrow{a_2}$, the angle α between $\overrightarrow{a_1}$ and $\overrightarrow{b_2}$, the angle β between $\overrightarrow{b_1}$ and $\overrightarrow{b_2}$,the azimuthal angle θ between $\overrightarrow{a_1}$ and $\overrightarrow{b_1}$. The vectors $\overrightarrow{b_1}$ and $\overrightarrow{b_2}$ define the lattice vectors of the adlayer. The adlayer lattice vectors with a given azimuthal angle, θ is represented as a matrix transformation $[T]$ in terms of the substrate lattice vectors.

$$\begin{bmatrix} b_1 \\ b_2 \end{bmatrix} = [T] \begin{bmatrix} a_1 \\ a_2 \end{bmatrix} = \begin{bmatrix} p & q \\ r & s \end{bmatrix} \begin{bmatrix} a_1 \\ a_2 \end{bmatrix} \tag{3.1}$$

where:

$$p = b_1 \sin(\alpha - \theta)/a_1 \sin(\alpha) \tag{3.2}$$

$$q = b_1 \sin(\beta)/a_2 \sin(\alpha) \tag{3.3}$$

$$r = b_2 \sin(\alpha - \theta - \beta)/a_1 \sin(\alpha) \tag{3.4}$$

and

$$s = b_2 \sin(\alpha + \beta)/a_2 \sin(\alpha) \tag{3.5}$$

If $det\, T$ is an integer, then the adlayer is referred as commensurism. In this case: b_1=b_2=15 Å, β=90°, a_1=a_2=2.86 Å, α=60° and θ=0°. Accordingly to Eqs. 3.2, 3.3, 3.4 and 3.5, it is found for the p, q, r and s the following values: 5, 0, -3 and 6 respectively. Therefore, a commensurate superstructure with the following matrix is proposed:

$$\begin{bmatrix} b_1 \\ b_2 \end{bmatrix} = \begin{bmatrix} 5 & 0 \\ -3 & 6 \end{bmatrix} \begin{bmatrix} a_1 \\ a_2 \end{bmatrix} \tag{3.6}$$

Figure 3.3 a represents the orientation-domain boundary and the real-space orientation of individual molecules in both [A] and [B] orientation. Two square unit cells in [A] and [B], marked by dotted lines, show the same size and lattice orientations, respectively. In contrast the orientation of CoPc molecules in [A] and [B] is different, marked by the arrows. The orientation of CoPc molecules in [A] are along the $[\bar{1}2\bar{1}]$ and $[\bar{1}01]$ directions, and those in [B] are along $[11\bar{2}]$ and $[1\bar{1}0]$ directions of the Au(111) substrate. After a close inspection of Fig. 3.3 a, it can be observed that the two square unit cells in both [A] and [B] orientation-domains are shifted apart with $1/2$ unit cell. A similar shift has been also observed by L. Gao et *al.* between the adsorption sites (top and bridge) of the two adsorption configurations of FePc on Au(111) [31]. These observations strengthens the idea that the central cobalt atom of CoPc molecules in both [A] and [B] orientaion-domains resides on different surface sites. As can be seen from the STM image (Fig. 3.3 a) even near the boundary the ordered arrangement of the molecules is still maintained. Furthermore, the chirality of [A] unit cell is opposite to that of [B] unit cell. Submolecular resolution achieved in our study has allowed us to identify that, in the densely packed structure, the molecule are oriented with the outer benzene rings of one molecule pointing toward the aza-bridging nitrogen atom in the neighboring molecules. This arrangement could suggest a electrostatic interaction between the unshared electron pair of the nitrogen atom and the net positive hydrogen atom of the phenyl group of the neighboring molecule (Fig. 3.3 b).

3.1.3 Submonolayer of CoPc on the Cu(111) surface

Figure 3.4 a shows a large-scale STM image of two Cu(111) terraces after deposition of 0.1 ML of CoPc molecules. The Cu(111) crystal kept at room temperature, was exposed for 5 seconds to molecular flux at a distance of 1 centimeter from the molecular evaporator. After the deposition the crystal was transfered to the STM chamber and cooled to 4.6 K. Isolated bright spots, which are located in random fashion, are clearly discernible. High-resolution images as displayed in Fig. 3.4 b reveal that each of these protrusion corresponds to a single CoPc molecule. In general, at a submonolayer coverage the metal-phthalocyanine molecules adsorb in a flat lying configuration, with their macrocycle parallel to the substrate plane [19, 20, 26, 27, 29]. Contrary to the monolayer image (Fig. 3.3 a) molecules are not perfectly symmetric anymore. The molecular lobes of one molecular axis (which we define as L_1) are brighter that those along the orthogonal molecular axis (L_2). The L_1 axis perfectly aligns with one of the three equivalent crystallographic axes of the sixfold symmetric Cu(111) surface. Instead L_2 is not parallel to any other axes accordingly. Within experimental resolution no indication for the vertical bending of the molecules to the substrate nor in-plane deformation were found, i.e. L_1 and L_2 enclose an angle of exactly $90°$. The findings, that CoPc molecules, at low coverage, remain isolated and do not self-assemble into highly ordered islands on terraces point out an appreciable interaction between the molecules and the Cu(111) surface. The twofold symmetric appearance of the isolated CoPc molecule denotes that its adsorption properties can differ from a molecule in a monolayer, in which the microcycle has a fourfold symmetry (§ 3.1.2).

In order to investigate the local electronic structure of the individual CoPc molecules, we have applied STS on different locations over the molecule. Five distinct dI/dV spectra are presented in Fig. 3.5. The one denoted 3 was recorded over the central cobalt atom. Spectra denoted 1 and 5 were recorded at the edge of the two adjacent molecular lobes where the benzene ring should be mostly conducting (see sketch of CoPc molecule in Fig. 3.5), whereas spectra 2 and 4 were acquired on the pyrrole group. The five dI/dV spectra have six peaks at sample biases of -1.3 V, -1.0 V, -0.63 V, -0.53 V, -0.1 V, $+0.4$ V and $+1.5$ V indicated as $H-1$, I_3, d, H, I_2, I_1 and L respectively. Since the spectrum recorded on pristine Cu(111) surface does not reveal the above features, the peaks were attributed to the molecular structure of CoPc adsorbed on the Cu(111) surface. The dI/dV spectra measured at positive bias voltages corresponds to the unoccupied states of the CoPc molecules on the surfaces. Unoccupied states of CuPc and H_2Pc molecules on Cu(110) surfaces have been studied by inverse photoemission

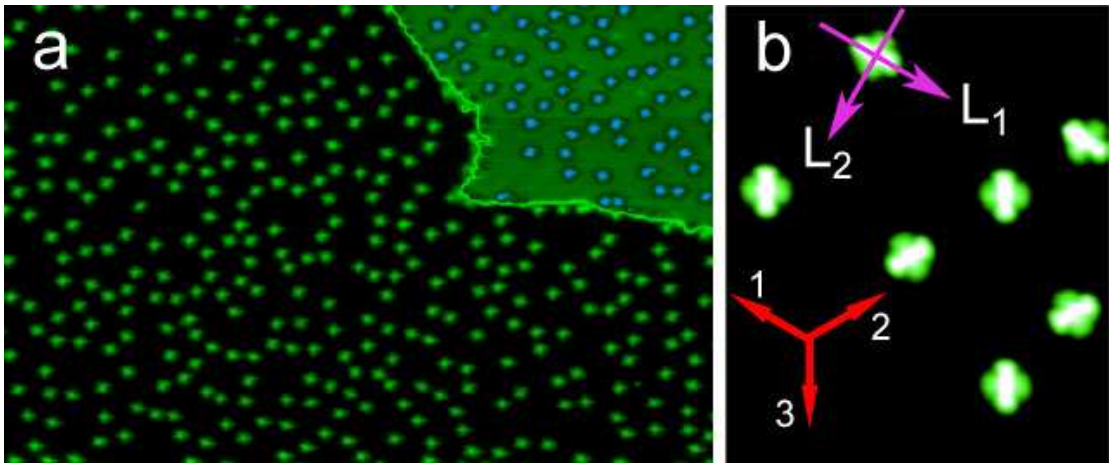

Figure 3.4: a) Large-scale STM topography of CoPc molecules on a Cu terrace (Scan size: 100 nm$\times 65$ nm; Tunneling parameters: $V = -1.0$ V, $I = 0.1$ nA). b) High-resolution STM image with intramolecular features revealing a twofold symmetry. Red arrows sketch the three crystallographic directions (110), (101), (011) of copper, whereas the orthogonal pink arrows represent the two molecular axes, L_1 and L_2 (Scan size: 14.5 nm$\times 14.5$ nm; Tunneling parameters: $V = 0.4$ V, $I = 0.7$ nA)

spectroscopy. The lowest unoccupied molecular orbital (LUMO) of H_2Pc and CuPc has been observed at 1.2 eV and 1.3 eV above E_F,respectively [38]. Nazin et *al.* have reported that the LUMO of CuPc molecules on the NiAl(110) surface is located at 0.98 V above E_F as determined from dI/dV spectra measured at 13 K [39]. In the case of single CoPc molecule adsorbed on the Au(111) and Cu(100) surfaces the LUMO was found to fall at 1.1 V [18]. Moreover, STS spectra acquired on individual CoPc molecules adsorbed on vicinal Au(788) surfaces places the LUMO at 1.4 V [16]. Compared with these results, the pronounced resonance denoted L at 1.5 V in Fig. 3.5 is assigned to the LUMO. For negative sample voltages, i.e., for the occupied sample states, the dI/dV spectra show well defined peaks. The peak at -0.53 V below the Fermi level and labeled H in the Fig. 3.5 is attributed to the highest occupied molecular orbital (HOMO). A similar feature was found for CoPc molecules on Au(111) and Cu(100) surfaces [18]. Therefore the HOMO-LUMO gap for the CoPc molecule adsorbed on Cu(111) surface amounts to ≈ 2 V which agrees well with previous studies [17, 18]. The resonance denoted as $H-1$ and located at -1.3 V is then the lower lying occupied molecular orbital (HOMO-1). The spectrum labeled 3 in Fig. 3.5 acquired with the tip positioned above the central cobalt atom of the CoPc molecule is dominated in its negative part by a broad

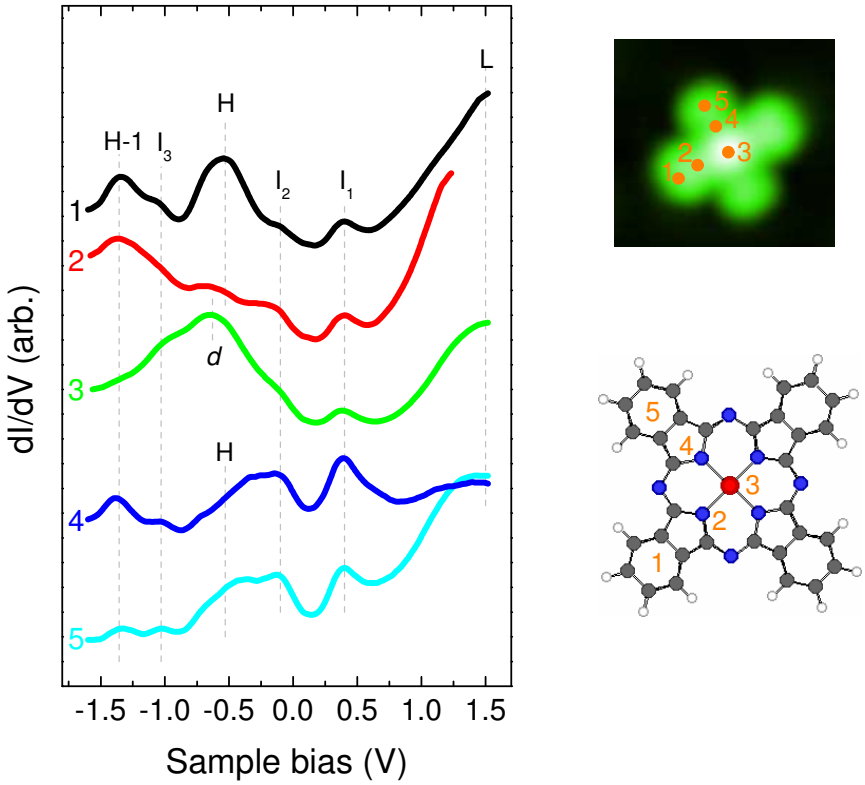

Figure 3.5: dI/dV spectra over an isolated CoPc molecule adsorbed on the Cu(111) surface, whereby 1, 2, 4 and 5 are different locations over the macrocycle and 3 is right over the central cobalt atom (the five locations are indicated on the image and on the chemical structure). The spectra are vertically shifted for clarity. Labels to the resonance are described in the text. Feedback loop parameters: $V = -1.0$ V, $I = 0.5$ nA.

resonance centered at -0.63 V. In agreement with previous measurements [16, 17, 18, 19], the origin of this resonance is assigned to the cobalt d_{z^2} orbital. The position of this resonance is shifted further away from the Fermi energy compared to CoPc molecule adsorbed on Au(788), Au(111) and Cu(110) where it was observed at -0.18 V, -0.3 V and -0.45 V respectively [16, 18]. This indicates that the central cobalt atom is differently coupled with the Cu(111) surface as expect. Indeed, when increasing the distance of the cobalt atom to the surface in the Co-TBrPP molecule [cobalt 5,10,15,20-Tetrakis-(4-bromophenyl)-porphyrin], a fourfold flat molecule similar to CoPc, a significant shift of the d_{z^2} resonance occurs [41]. Finally, there are three relatively intense resonances on all five spectra coming out at $+0.4$ V, -0.1 V and -1.0 V, noted I_1, I_2 and I_3, respectively. Takada et *al.* [18] observed two similar resonances

at the Fermi energy and at $+0.1$ V for the CoPc molecules adsorbed on the Cu(100) surface. They have assigned these resonances to adsorption-induced states. More exactly it is thought that the resonances arise from the hybridization between the LUMO of the CoPc molecule and the electronic states of the Cu(100) surface. It was also reported that the dI/dV spectra of C_{60} molecules on Ag(100) and Cu(111) surfaces present adsorption-induced states while those on the Au(111) surface have no additional peaks around E_F [42, 43, 44]. Based on these experimental observations we speculate that the I_1, I_2 and I_3 resonances are generated by the hybridization of either the LUMO, HOMO or HOMO-1 molecular orbitals with the Cu(111) surface electronic states. In the gas phase the electronic structure of the ligands of the CoPc molecule are highly symmetric and homogeneous. The fact that the spectra 1 , 5, and 2, 4 differ from each other, indicates that the four-fold symmetry of the CoPc molecule is not preserved upon adsorption. A reduction to the twofold symmetry was reported for single CuPc molecules adsorbed on the Cu(111) substrate [45], whereas for single FePc adsorbed on the Cu(111) substrate, the symmetry reduction is nearly lifted but faintly present [29, 46].

To gather more information about the symmetry loss, we have acquired images at biases where resonances occur in the spectra as reported in Fig. 3.5. We have chosen five biases: -1.4 V (close to the HOMO-1), -1.0 V (I_3), -0.5 V (close to the HOMO and the cobalt d_{z^2} resonance), -0.1 V (I_2), and $+1.5$ V (LUMO). Figure 3.6 presents the topographic images of the molecule together with the apparent height profiles along two axes (L_1 and L_2) of the molecule. Images recorded at -1.4 V and -1.0 V of CoPc are quite similar. In the lateral profiles, the lobes along the two axes are equivalent, and the cobalt atom appears as a protrusion ≈ 0.5 nm high in the center of the molecule. The image acquired at -0.5 V is similar to the previous ones, but the overall apparent height of CoPc is diminished as the HOMO-1 orbital no longer contributes to the tunneling. The signal coming from the cobalt atom dominates the profile and the asymmetry along the two axes starts to appear. The relative apparent height of the phthalocyanine ligands compared to the one of the cobalt atom is different for the two directions. On the image taken at -0.1 V, the cobalt atom has the same height as the phthalocyanine ligand, since the Co d_{z^2} orbital is no longer participating to the tunneling process. The asymmetry between the axes becomes evident, if we look to the topographic image taken at $+0.4$ V. It is however reversed compared to -0.5 V. In the $+0.4$ V image the organic legs are brighter along L_1, whereas at -0.5 V they are brighter along L_2. The bias dependence hints to an electronic effect rather than a structural effect (bending of the molecule along one axis) for explaining the asymmetry. Within this image the apparent height profile along L_2 is

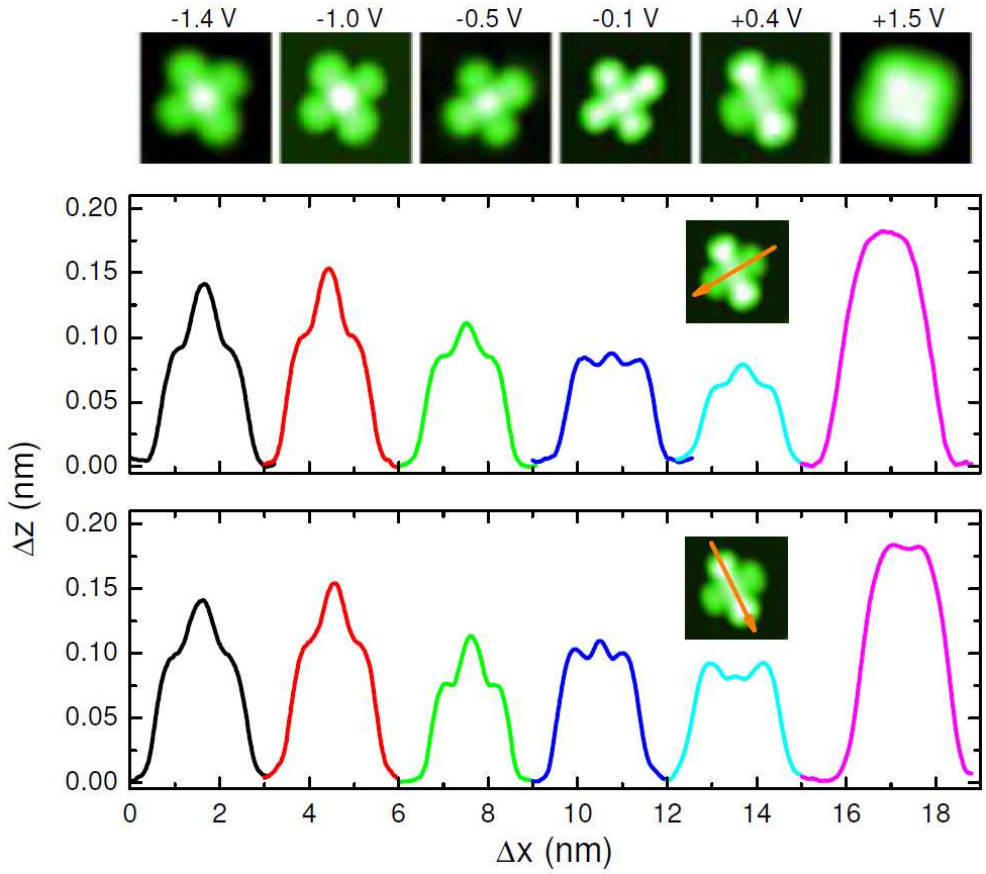

Figure 3.6: Top panel: topographic images of CoPc on Cu(111) (3.6 nm$\times 3.6$ nm) at different biases, noted above the images. Middle panel: apparent height profiles along L_2, indicated by the orange arrow on the inset image. Bottom panel: apparent height profiles along L_1, indicated by the orange arrow on the inset image. The profiles are horizontally shifted for clarity.

dominated by central part of the molecule, whereas along L_1 it is dominated by the aromatic cycle. At $+1.5$ V, the intramolecular contrast is lost. The apparent height of the molecule is the highest we observed within the bias range investigated, and only slight differences are observed along the two axes.

In conclusion, the CoPc molecule adopts a two-fold symmetry once it is adsorbed on Cu(111). This produces a spatial inhomogeneity of the electronic structure within its skeleton. Further, it seems that the carrier transport properties at the interface between a single CoPc molecule and a Cu(111) surface will strongly depend on the intramolecular position where the molecule is in contact with the surface. The difference in electronic behavior of the ad-

jacent molecular lobes can be assigned to a different substrate coupling and lattice matching properties.

To gain further insight in the coupling of the CoPc molecules with the Cu(111) surface, first principle calculation based on density functional theory by means of PWSCF package have been performed. The computation has been carried out by Thomas Brumme within a collaboration with the group of Prof. Dr. Jens Kortus at the Institut für Theoretische Physik which is part of Techniche Universität Bergakademie from Freiberg (Germany). The next paragraph presents a summary of these theoretical calculations essential to the interpretation of the experimental results. More details can be found in Ref. [47].

3.1.4 Modeling the adsorption of CoPc on the Cu(111) surface

Before determining and understanding how the CoPc molecule is coupled with Cu(111), a description of the electronic structure of the free-standing molecule is necessary. The coordinates given in Ref. [48] were used as a starting geometry for the structural relaxation. The periodic boundary conditions were chosen so that the influence of the neighboring molecules is negligible. The optimized molecular structure of the CoPc molecule is illustrated in Fig. 3.7 a, where the central cobalt atom is bonded to four nitrogen atoms.

The splitting of the degenerated $3d$-orbitals of single planar CoPc molecules are as follows: d_{z^2}, d_{xy}, d_{xz}/d_{yz} and $d_{x^2-y^2}$ (from the highest to lowest energy). Taking the molecule to lie in the xy plane, the d_{xz}/d_{yz} orbitals have π character and the rest may be considered of σ type. The molecular orbital theory has been used to calculate the electronic structure of the CoPc molecule. Within this theory the organic ligands and the transition cobalt atom can form a covalent bond. Additionally, π-bonds have been considered. As shown in the Figs. 3.7 b and 3.8, between -6 eV and -4 eV there is a hibridization between cobalt $d_{x^2-y^2}$ and nitrogen p_x/p_y orbitals. Furthermore, one can identify π-bonding between the cobalt d_{xz}/d_{yz} orbitals and p_z orbital of nitrogen at about -0.33 eV and -0.16 eV (Figs. 3.7 b and 3.8). The states near E_F and at 1.7 eV are their corresponding anti-bonding states. The calculation yields a d_{z^2} orbital as the lowest unoccupied molecular orbital (LUMO) and d^*_{xz}/d^*_{yz} orbital as the highest occupied molecular orbital (HOMO) (Fig. 3.8). Projected densities of states of the cobalt metal atom in the free CoPc molecule are spin-polarized, which indicate the existence of a local magnetic moment in this molecule. Indeed, the unpaired spin of the cobalt d_{z^2} orbital gives rise to a magnetic moment of about 1.09 Bohr magnetons (μ_B). This value is in between the

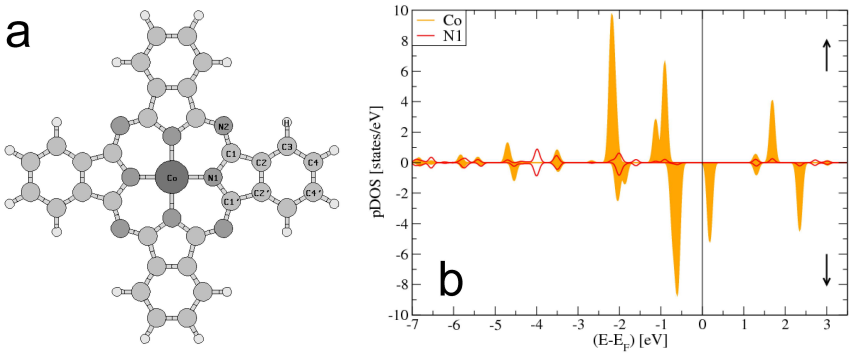

Figure 3.7: a) Molecular geometry of Cobalt Phthalocyanine. b) Spin resolved projected density of states (PDOS) of cobalt d-orbitals and the nitrogen p-orbitals in the free-standing CoPc molecule. Positive values of the pDOS correspond to spin up and negative values to spin down.

ones found for the metal atom in free FePc and CuPc, which where $2.03\ \mu_B$ and $0.54\ \mu_B$, respectively [32]. The central cobalt atom is a hole donor in the material, so the π electrons from the phthalocyanine inner ring may fill the metal d orbitals. Such a situation could explain the observed low spin state of the CoPc molecule compared to Co^{2+} ($4.8\ \mu_B$).

A periodic slab model has been employed to describe the adsorption of CoPc on Cu(111). It consists of a supercell containing a total of 249 atoms: one CoPc molecule with 57 atoms, as well as a three copper-metal-layer slab in the (111) orientation, with 64 atoms per rectangular layer. The CoPc molecule was placed about 2 Å above the copper metal slab. During the geometry optimization only the atoms of the lowest copper layer of the metal slab were held fixed at their position according to their bulk values. The space between the different CoPc molecules of the repeated cells was about 6 Å vacuum, which is wide enough to avoid interactions between them. A single atom deposited on surface oriented in (111) direction prefers to sit on hollow site, either hexagonal close-packed (hcp) or face-centered cubic (fcc) lattice sites. In our case the cobalt atom placed in the middle of the phthalocyanine cavity is surrounded by four identical organic ligands, which consist of a pyrrole group coupled to a benzene ring and connected to each other via nitrogen atoms. Therefore the CoPc molecule-Cu(111) surface interaction can be dominated by the benzene rings, the outer or the inner (those who belong to the pyrrole groups) nitrogen atoms or the central cobalt atom itself. The competition between theses interactions can drive the entire CoPc molecule to sit with the central cobalt atom on three different positions: top, hollow and bridge position. The bond lengths from the central cobalt atom to the next surface copper atom were found to be 2.45 Å, 2.60 Å and 2.70 Å in

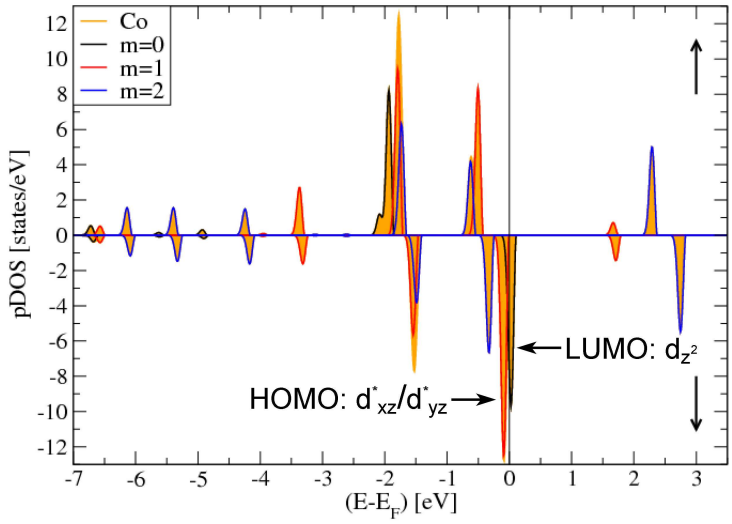

Figure 3.8: Spin resolved projected density of states (PDOS) of cobalt d-orbitals in the CoPc molecule. For clarity the d-contribution is split into different values of m, which deliver information on the d-states involved ($m = 0$: d_{z^2}, $m = 1$: d_π=d_{xz}/d_{yz}, $m = 2$: d_{xy}, $d_{x^2-y^2}$). Positive values of the PDOS correspond to spin up and negative values to spin down.

top, bridge and hollow position respectively, suggesting that the interaction between the central cobalt atom and the copper surface may be stronger for the top position (Fig. 3.9 b). If the orientation of the benzene rings is chosen in such a way to enhance the interaction between them and the underlying substrate, the CoPc molecule can even adopt the hollow position. However, in both cases (top and hollow position) the bonds formed by the central cobalt atom and the benzene rings with the surface copper atoms are not strong enough to fix the entire CoPc molecule in such positions. At this point the nitrogen atoms come into play, providing the most efficient interaction with the underneath surface copper atoms. The tendency of all nitrogen atoms to adopt a top position guides the entire CoPc molecule towards the bridge position (Fig. 3.9 a). In this position, the p_z orbitals of the nitrogen atoms can hybridize with the $d_{3z^2-r^2}$-orbitals of the surface copper atoms. Due to these possible bonds to the surface the system can save energy, explaining why the adsorption energy in the bridge configuration has the lowest value (408 meV lower than that in top configuration). Contrary to our case, CoPc as well as NiPc and CuPc [32] prefers to adsorb onto the Au(111) surface in a hollow position. The difference with Cu(111) can be explained by the small misfit which occurs between the CoPc molecule and the Au(111) surface below, not every nitrogen atom being in such a favorable

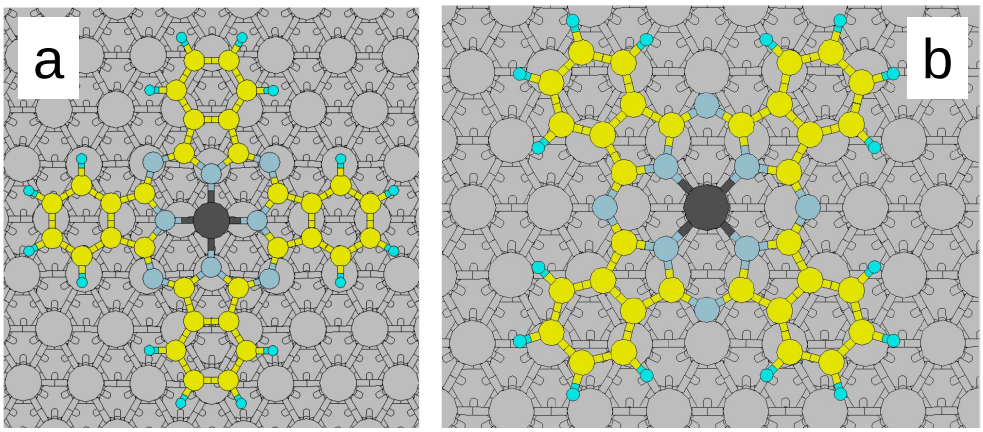

Figure 3.9: CoPc molecule adsorbed on a Cu(111) surface: a) bridge position and b) top position. Grey-Cu, black-Co, dark-blue-N, yellow-C and light blue-H.

position as in Cu(111). A detailed inspection of the bridge position reveals that the two inner nitrogen atoms, belonging to the molecular axis which is perpendicular on the direction given by the bridge copper atoms, are placed on top of surface copper atoms, whereas two inner nitrogen atoms aligned along orthogonal molecular axis (that parallel to the direction given by the bridge copper atoms) are in less favorable position (Fig. 3.9 a). This might suggest that the coupling strength between the molecular structure and the copper surface underneath may vary between the two orthogonal molecular axes.

The interaction between the CoPc molecule and the Cu(111) surface changes the electronic structure and magnetic property of the CoPc molecule. When the CoPc molecule is adsorbed on Cu(111), its magnetic moment is completely canceled by the molecule-surface interaction, which indicates that there is either a direct bond between the central cobalt and the copper surface or a charge transfer between the CoPc molecule and the surface. In the first case the LUMO of the CoPc molecule (d_{z^2}) becomes occupied while in the second case the half-filled orbital is emptied. The spin-polarized partial density of states of the cobalt atom in the free CoPc have revealed that the spin-down states were filled more than the spin-up states (Fig. 3.8). However, the filling difference disappeared for the CoPc adsorbed on Cu(111) surface (Fig. 3.10), so that the magnetic moment of the molecule changes from $1.09\ \mu_B$ to $0.0\ \mu_B$.

The partial density of states of the nitrogen atom bonded to the central cobalt atom and of both the copper atoms beneath is presented in Fig. 3.11. The two copper atoms, which form the bridge, have states at the cobalt d_{z^2} peak near -1 eV. The broad density of states

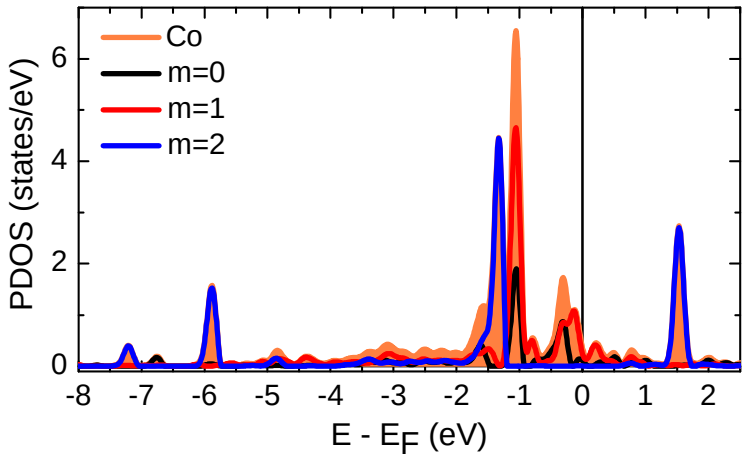

Figure 3.10: Projected density of states (PDOS) of cobalt d-orbitals in the CoPc molecule adsorbed on Cu(111) surface in bridge position. The m-resolved d-contribution is very different to those of a free CoPc molecule (Fig. 3.8). Because of direct bond to the surface the d_{z^2}-orbital is no longer the LUMO. Now it splits into a bonding and anti-bonding state. Since the geometry of the molecule is changed, the d_π-orbitals are not degenerated anymore.

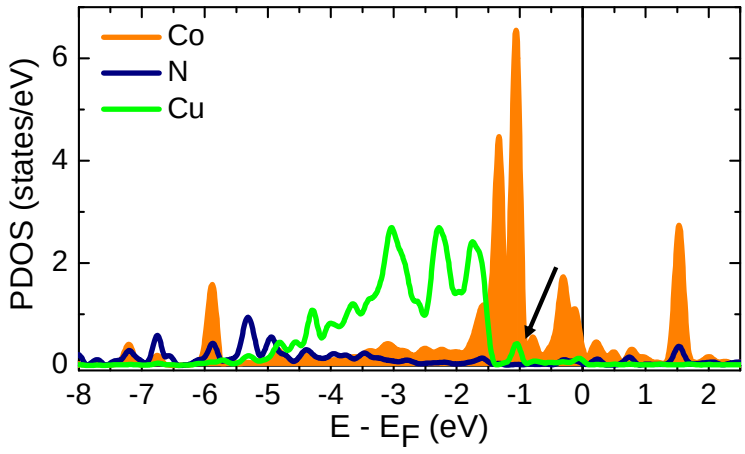

Figure 3.11: Projected density of states (PDOS) of the cobalt and nitrogen of CoPc molecule and one of the copper atom forming the bridge. One can clearly see that the copper atom has states (indicated by black arrow) at the same energy as the cobalt d_{z^2}-orbital (Fig. 3.10). The hybridization between the p-orbitals of the nitrogen and the cobalt can be identified as suggest by the occurrence of peaks at the same energy.

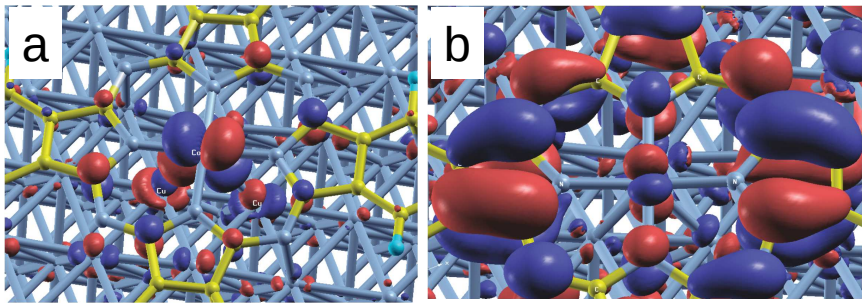

Figure 3.12: a) Isosurface plot of an anti-bonding combination of surface d_{z^2}-orbital and cobalt d_π-orbitals at $(E-E_F)$=-1.0582 eV. b) Isosurface plot of the eigenfunction of the eigenstate at $(E-E_F)$=0.2533 eV. The state at this energy is an anti-binding combination of the d_π-orbitals with the ligand orbital. Blue corresponds to negative phase and red to positive.

between -5 eV and -2 eV is dominated by the hybridization of the d_π-orbital with nitrogen p-states and surface copper states. The prominent peaks at -5.7 eV and -5 eV correspond to a bonding combination of nitrogen p_x/p_y and cobalt $d_{x^2-y^2}/d_{xy}$. In the isosurface-plots of the eigenfunctions given in Figs. 3.12 a and 3.12 b are shown some possible tunneling paths in a STM experiment. The current can flow either directly trough the central cobalt atom or first to the benzene rings and then to the surface. A close inspection of the isosurface-plot showed in the Fig. 3.12 b, reveals a asymmetric distribution of the molecular orbital along the ligands (benzene rigs) of the two molecular axes. One can identify big charge densities along the ligand (benzene rings) of one molecular axis, while small charge densities exist along the ligand (benzene rigs) of the orthogonal molecular axis. This suggest that the tunneling current flows differently across the two molecular axis. Comparing both the calculated isosurface-plot (Fig. 3.12 b) and the experimental topographic image taken at $+0.4$ V (Fig. 3.6), one can speculate on how the tunneling process takes place across the two molecular axes. The apparent height profile along L_1 is dominated by the ligands (see the two pronounced protrusion at the sites of the benzene rings), and in analogy with the isosurface-plot, this is due to the big charge densities located over the corresponding ligands. A significant signal stems from the central Co atom, but can be neglected at this energy compared to the one coming from the ligands (benzene rings). Therefore, a big part of the tunneling current across the L_1 flows directly trough the ligands (benzene rings). Regarding the orthogonal molecular axis, L_2, the ligands conduct very little (small charge densities above them) and the apparent height profile is dominated by the cobalt atom. The tunneling current thereby flows through the d_π-orbitals

of the central cobalt atom. As can be seen from Fig. 3.9 a, the incommensurability of molecule (fourfold symmetry) and surface (sixfold symmetry) results in a different atomic configuration underneath two perpendicular molecular axes. Therefore, the hybridization (interaction) of the molecular orbitals with the different atomic structure underneath is the consequence of symmetry-reduction of molecular structure from fourfold (gas phase) to twofold (adsorbed on surface).

3.2 The cobalt nanoislands

3.2.1 Electronic properties

The differential conductance acquired in the middle of Co nanoislands, either faulted or unfaulted, is dominated by three distinct peaks: two located below Fermi level and one above (Fig. 3.13 a) [49]. Peaks labeled 1 and 2 have their origin in the same minority d band split at the intersection with the Cu(111) bulk band (Fig. 3.13 b). The former peak, labeled 1, has a spin-polarized nature and is given by the hybridization of sp-minority states with the minority d band situated in the bulk band gap [50, 51]. A surface state with similar character has been observed with STS on Co(0001) [52], on Fe(001) and Cr(111) [53] and on self-organized Co nanoclusters on Au(111) [54] and Pt(111) [55]. Peak 2 appears due to a resonant overlapping of Cu(111) bulk states with the Co minority d band [51]. In the first STS study on Co nanoislands, a smooth featureless spectrum was observed [56]. Since this experiment was performed at room temperature and the surface states are known to be very sensitive to contaminations, it is likely that Co-Cu intermixing is the reason why none of the two peaks was observed. Peak 3 is in the positive part of the spectrum and stems from an unoccupied Co minority d band [51]. All three peaks are located in the first half of the Brillouin zone. Beside the states revealed by STS, a free-electron-like, mostly unoccupied state of sp-majority character can be visible in the STM through Friedel oscillations in the local density of states (LDOS) over a wide energy range [50, 49].

As demonstrated earlier [54], the stacking order of bilayer Co nanoislands on (111) noble metal surfaces plays a key role since some peaks in the density of states are shifted by as much as 60 meV. In the case of the Co nanoislands grown on Cu(111) only two stacking sequences have to be considered in terms of faulted and unfaulted nanoislands. The spectra for the two types of islands (faulted and unfaulted) are quite similar and only differ for negative biases by

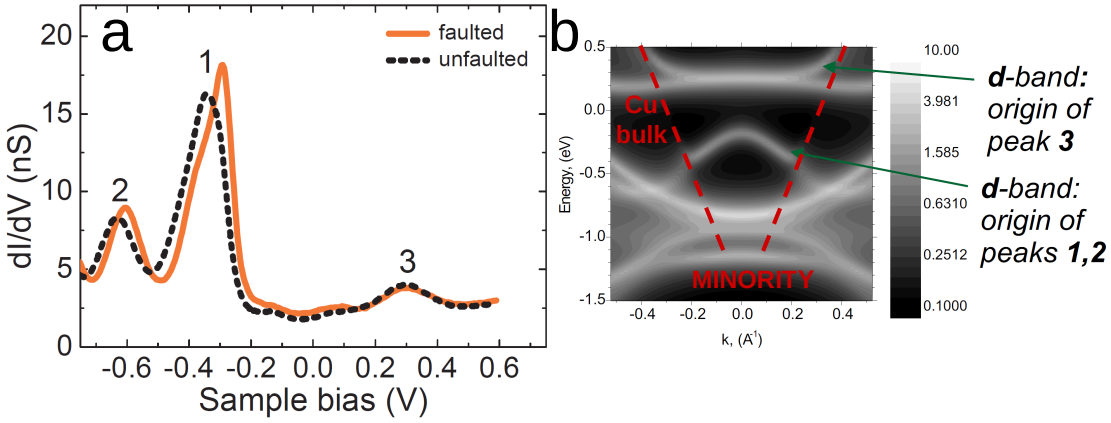

Figure 3.13: a) dI/dV spectra over Co nanoislands (faulted: solid line; unfaulted: dashed line). Feedback loop opened at $I = 1.5$ nA, $V = 0.6$ V. b) Spectra density map of Co nanoislnad (minority channel).

a shift in the position of peaks 1 and 2. On unfaulted islands, peaks 1 and 2 are centered at $-0.31\ V$ and $-0.64\ V$ respectively, while on the faulted islands, they increase the intensity and are found at $-0.28\ V$ and $-0.60\ V$ respectively.

The spectra presented in Fig. 3.13 a were recorded on the Co nanoislands of same size. In fact, beside the fact that the cobalt nanoislands have different crystallographic stacking, it has been shown that their surface states vary with their size [51]. As it can be seen in Fig. 3.14 a and 3.14 b, faulted and unfaulted nanoislands have their peaks 1 and 2 shifting downward in energy when the island size decreases. In the case of an unfaulted nanoisland the shift of peak 1 is monotonical over 0.09 V, whereas a faulted nanoisland shows a stepper increase of the shift followed by an asymptotic behavior for nanoislands larger than 13 nm (Fig. 3.14 b). The theoretical calculations have established that the driving force for the observed shift is the size-dependent Co-Co relaxations in the nanoislands. The initial stage of the growth process of the Co nanoislands on Cu(111) at room temperature is affected by the lattice mismatch between the nanoisland and the substrate as well as the bonding interactions in the nanoisland-substrate interface (ligand effect). During the growth process of nanoislands, the cobalt atoms tend to keep their intrinsic bond length and at the same time, to adopt the lattice parameter of the underlying Cu(111) substrate. The competition between these two processes leads to strain relaxation in the cobalt nanoislands. The strain relaxation induces an inhomogeneous distribution of the in-plane cobalt bond length over the nanoisland, except for an inner region around the center of the nanoisland, where a nearly homogeneous distribution of the bond

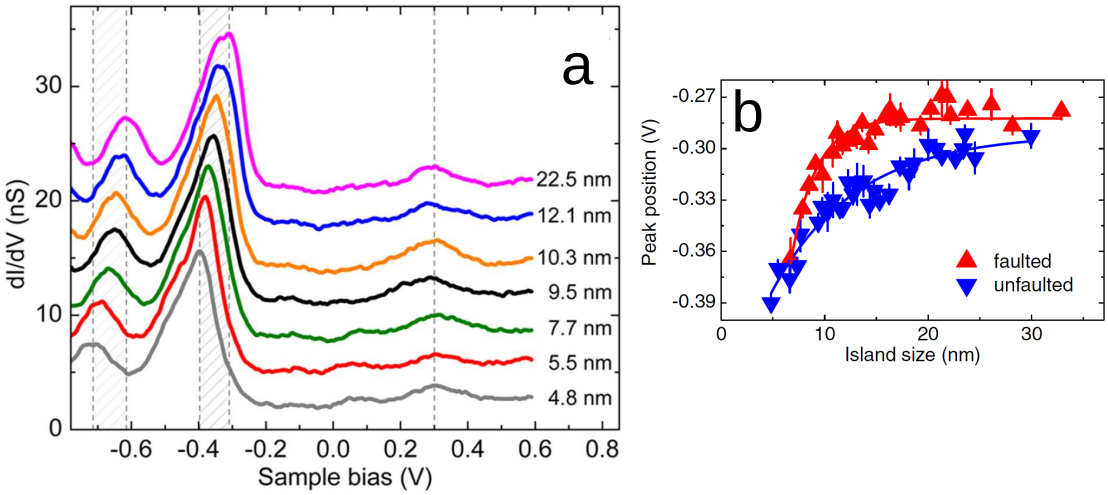

Figure 3.14: a) dI/dV spectra acquired on unfaulted nanoislands of increasing size. The spectra are vertically shifted for clarity. b) Peak position (labeled 1) versus island size (up triangles: faulted; down triangles: unfaulted). Solid lines are a guide to the eye. Data are binned by steps of 0.5 nm (from [51]).

length exist. The average in-plane cobalt bond length r of the inner region varies with the nanoisland size. With increasing island size, r increases towards the ideal bond length of bulk Cu ($r_0 = 0.255$ nm). In the framework of a tight-binding model, the width of bulk energy band, neglecting the crystal-field contribution, can be expressed by the following expression:

$$\Delta E(,r) = 2\, Z_b\, \beta_0\, exp(-q\, r) \tag{3.7}$$

where Z_b is the coordination number, β_0 is the transfer integral, q is a positive material-dependent constant and r is in our case the in-plane Co-Co bond length [57]. For occupied electronic states the transfer integral is negative ($\beta_0 < 0$). On the most close-packed surfaces, the LDOS are weakly perturbed with respect to the bulk ones. They are slightly narrowed because the coordination number changes when passing from bulk to surface ($Z_s < Z_b$). However, the Eq. 3.7 can be applied for the surface minority d-band. The LDOS can be also characterized by their moments:

$$\mu_p = \int_{-\infty}^{+\infty} \epsilon^p \rho(\epsilon)\, d\epsilon \tag{3.8}$$

where $\rho(\epsilon)$ is the LDOS. According to this equation: the zero moment,

$$\mu_0 = \int_{-\infty}^{+\infty} \rho(\epsilon)\, d\epsilon = 1 \tag{3.9}$$

is alway one, owing to the normalization condition of the atomic orbitals basis; the first moment,

$$\mu_1 = \int_{-\infty}^{+\infty} \rho(\epsilon)\epsilon\, d\epsilon = \bar{\epsilon} \tag{3.10}$$

is the center of gravity of LDOS, and the second moment:

$$\mu_2 = \int_{-\infty}^{+\infty} \rho(\epsilon)\epsilon^2\, d\epsilon = \overline{\epsilon^2} \tag{3.11}$$

is the mean square deviation of the LDOS and, hence, is a measure of the *moment of inertia* of the LDOS with the center of gravity. A straightforward calculation gives for the second moment of the LDOS the following expression:

$$\mu_2 = Z\beta_0^2\, exp(-2q\, r) \approx \Delta E^2 \tag{3.12}$$

Following Eq. 3.7, the increase of r with nanoisland size causes a reduction in the minority d-band width. According to the Eqs. 3.11 and 3.12 the modification of the minority d-band width induces a energy shift towards the Fermi level. Contrary to peaks 1 and 2 , the position of peak 3 is unchanged. This follows from the flat nature of the unoccupied minority d-band around the Γ point (Fig. 3.13 b), i.e. $\beta_0 \rightarrow 0$ and $\Delta E = 0$.

It experimentally and theoretically has been shown that the strain in the surface can modify the chemisorption properties considerably [58, 59, 60]. By depositing a reactive metal on a less reactive metal, the strained overlayers will provide a surface with a higher chemical reactivity than both of the components. This can be the reason why all the deposited molecules adsorbed preferentially on the strained Co nanoislands, rather than on copper as shown in the next section of this chapter.

In conclusion the electronic properties of the Co nanoislands are effected by both their size-dependent relaxation and stacking. In order to eliminate the electronic contrast provided

by these effects, one can work on hcp islands with lateral dimensions larger or equal to 12 nm.

3.2.2 CoPc molecules on the nanoislands

The CoPc/Co nanoislands/Cu(111) system has been realized as follows: in a first step the cobalt nanoislands were grown on the Cu(111) surface as described in Chapter 2. Subsequently the surface held at room temperature and located 1 centimeter above the molecular evaporator was exposed for 40 seconds to a molecular flux of 0.02 ng/s. Finally, the crystal was transfered in the STM chamber and slowly cooled down to 4.6 K. In the large scale STM topographic image displayed in Fig. 3.15 a, bright spots distributed over the cobalt nanoislands are clearly visible. A close up image of a cobalt nanoisland is presented in Fig. 3.15 b. It shows that after decorating the step edges of the cobalt nanoisland because of the high adsorption energy on the step edges, the CoPc molecules preferentially adsorb on top of the cobalt nanoisland. In view of our purpose to explore the electronic and magnetic properties of a CoPc molecule adsorbed on a cobalt nanoisland, this was very encouraging. At the step edges, the majority of the CoPc molecules bind with two ligands on the copper surface while the other two ligands are anchored at the cobalt nanoisland edge. The CoPc molecules adsorbed on the cobalt nanoisland reveal sub-molecular contrast with a bright cobalt center surrounded by four lobes. The molecular plane of the CoPc molecule is parallel to the cobalt nanoisland surface, i.e., all the ligands are attached to it. At typical island coverage of 10 molecules for an area of $(10$ nm$)^2$, no CoPc molecules were found to adsorb on the Cu(111) surface.

To understand the preferential adsorption of CoPc on the cobalt nanoislands, it is interesting to refer to the so-called d-band model introduced by Hummer and Nørskov [61, 62, 63]. The model has its starting point in the interaction of adsorbate electrons with the valence states of surface atoms. In the metal, the highly itinerant s and p-band electrons form a broad band of states whereas the d-band electrons form a relatively narrow band owing to the small coupling matrix element between the more localized d orbitals. The coupling between the adsorbate and the surface usually includes two steps. First, the adsorbate is coupled to the broad metal sp-band. Density functional calculations have shown that this interaction leads to a broadening and a downshift in energy of the metal-adsorbate derived states. Second, the renormalized adsorbate states are then coupled to the narrow metal d-band. This interaction is well-described by the formation of bonding and antibonding states. If the coupling to the metal sp-band can be considered to be essentially similar for the transition and noble metals,

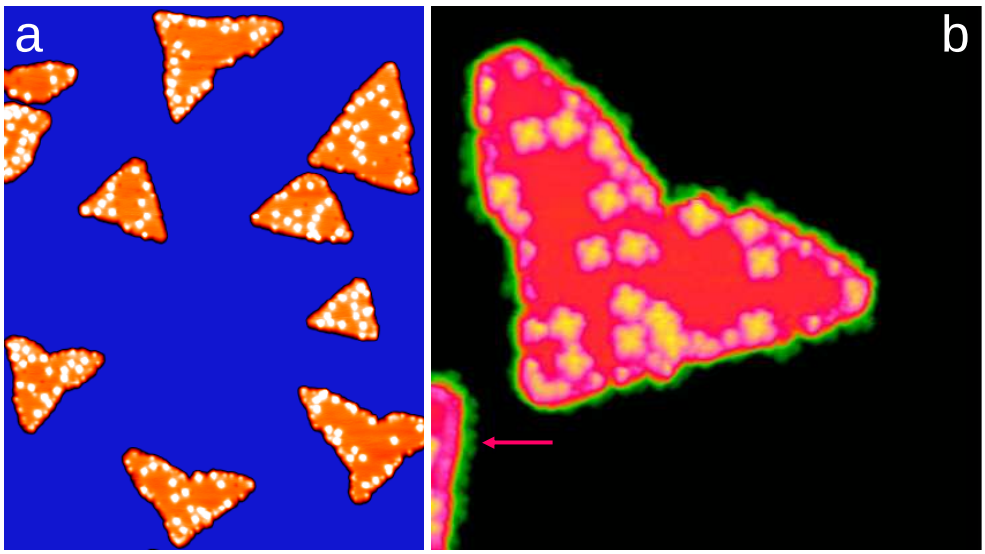

Figure 3.15: a) Large-scale STM topography depicting the CoPc molecules adsorbed on the cobalt nanoisland grown on Cu(111) surface (Scan size: 100 nm$\times 77$ nm; Tunneling parameters: $V = -1.0$ V, $I = 1.0$ nA). b) High-resolution STM image of a cobalt nanoisland decorated with CoPc molecules. Red arrow indicates the CoPc molecule adsorbed at the step edges of the cobalt nanoisland (Scan size: 28 nm$\times 28$ nm; Tunneling parameters: $V = 0.1$ V, $I = 1.0$ nA).

trends in the interaction energy between an adsorbate and a metal surface are governed by the coupling to the metal d-band. According to the d-band model, the key parameter for evaluating bond strengths between adsorbates and transition metal surfaces is the (energy) position of the d-band center with respect to the Fermi energy, $\epsilon_d - \epsilon_F$. The noble metals exhibit a low-lying d-band center, because the d-band is filled with electrons. Copper is indeed a noble metal because the d-band center is low-lying so that the interaction with virtually any adsorbate gives rise to a large fraction of antibonding states, which would therefore result in a weaker binding energy of the adsorbate to the surface. On the contrary, if the d-band center is close to the Fermi level, a large fraction of the antibonding states between the adsorbate and the surface will be pushed above the Fermi level and empty, resulting in a strong bond to the surface. Therefore a possible route for modifying the reactivity of the metal surface is to alter the energy of the d-band center relative to the Fermi level. The cobalt nanoislands have their minority $d_{3z^2-r^2}$ band close to Fermi level, thus providing a more reactive surface to adsorbates than the Cu(111) surface. This might then explain the presence of CoPc for cobalt nanoislands.

Such a conclusion is corroborated also by the similar behavior of C_{60} molecules (Fig. 3.16 a).

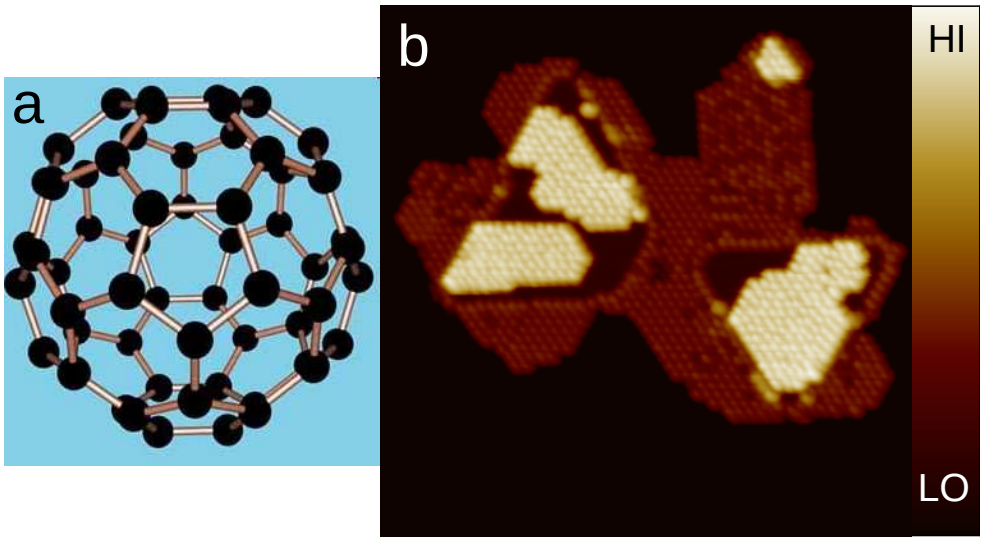

Figure 3.16: a) Structural model of C_{60} molecule. b) STM topography showing the C_{60} molecules adsorbed on the cobalt nanoisland and on Cu(111) surface (Scan size: 26 nm$\times 26$ nm; Tunneling parameters: $V = 1.9$ V, $I = 1.0$ nA).

As you can see in the Fig. 3.16 b, the cobalt nanoisland is partially covered with C_{60} molecules. Based on the STM images acquired with lower coverage of C_{60}, we can conclude that the C_{60} molecules favor also an adsorption on the cobalt nanoisland.

Another route for tuning the reactivity of a metal surface is changing the width of the d-band. The later can be done by subjecting the metal to strain. Strained metal surfaces can be achieved experimentally by growing pseudomorphic overlayers of one metal on top of a single-crystal substrate that has different lattice constants. Compressive or tensile stain will lead to an increased or diminished of the d-electron orbitals overlap of the metal atoms [64, 65, 66]. The altered overlaps will change the local width of the d-band according to the tight-binding theory (Eq. 3.7). To keep the band-filling constant (unchanged), the d-band center is shifted downwards when a metal is subjected to compressive strain and, correspondingly, upwards for tensile strain for more than half filled bands. We have seen in the section 2.2 of this chapter that, when the cobalt nanoislands size increase, their lattice expands, following a concurrent up-shift of the metal d states [51]. Therefore one can expect an increase of the surface reactivity of the cobalt nanoislands with their size.

The differential conductance, dI/dV, acquired with the tungsten tip positioned above the central cobalt atom of the CoPc molecule adsorbed on the cobalt nanoisland, is shown in the

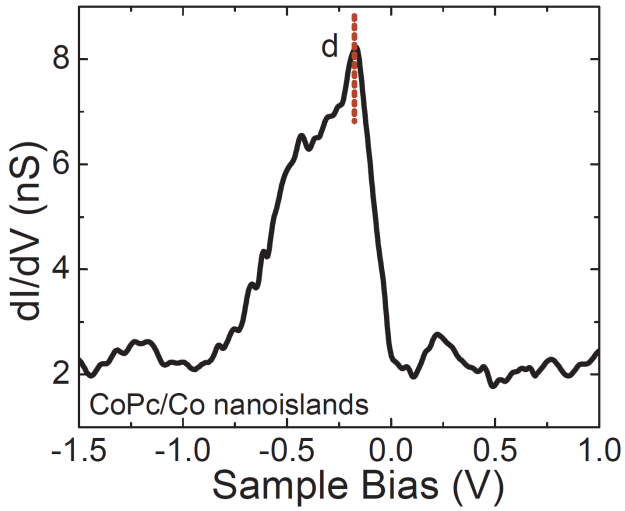

Figure 3.17: a) dI/dV spectra over the center of CoPc molecule adsorbed on the cobalt nanoisland. Feedback loop parameters: V=-1.0 V, I=0.5 nA

Fig. 3.17. As for CoPc molecule adsorbed on Cu(111) surface, the spectrum is likely dominated by a broad d-electronic resonance. While it is located at -0.63 V on Cu(111) surface, the resonance on the cobalt nanoisland is shifted towards the Fermi level and falls at -0.19 V. This indicates that the central cobalt atom is coupled to the underlying cobalt surface. Therefore there is good chance that the cobalt atom is spin-polarized when CoPc molecules resides on the cobalt nanoislands. Details about the adsorption site and coupling of the CoPc molecule on/with the cobalt nanoislands will be given in Chapter 5, where a spin-polarized STM and STS analysis on CoPc molecule is presented.

3.3 Conclusion

CoPc molecules were studied by means of STM and STS at low temperature (77 K and 4.6 K) in two configurations: a self-assembled structure on Au(111) surface and isolated molecules on both Cu(111) and cobalt nanoislands. For each investigated phase, our results show that the CoPc molecules adsorb with the molecular plane parallel to the surface. The images of the CoPc molecules adsorbed on all three surfaces are dominated by the central cobalt atom that, via the $3d$ orbital gives a major contribution to the tunneling current at negative bias. Evaporation of the CoPc molecules onto a Au(111) surface kept at room temperature results in

the formation of a densely-packed monolayer on the surface with a molecular unit cell of square symmetry. For this square adsorption phase the molecules are oriented with the benzene ring towards the aza-bridge nitrogen atom of the neighboring molecules. At low coverage, isolated CoPc molecules in three equivalent molecular orientations are found on Cu(111), reflecting the substrate symmetry. Therefore, attractive molecule-molecule interaction can be disregarded whereas a strong molecule-substrate interaction governs the adsorption. Upon the adsorption on Cu(111) surface, the four-fold symmetry of CoPc molecules (presented in the gas phase) is reduced to a two-fold symmetry, thereby one of the molecular axes is imaged brighter that the orthogonal molecular axis. It was determined through first principle calculations based on density functional theory that the energetically favored adsorption position of CoPc molecule on the hexagonal Cu(111) surface corresponds to the central cobalt atom between two copper atoms (bridge position). In fact the CoPc molecule is guided on the bridge position by the both inner and outer nitrogen atoms which are then located on top of underlying copper atoms. The loss in symmetry was not only seen in the topographic images (particularly on that acquired at -0.1 V and $+0.4$ V) but also in the electronic properties which were proven to vary with and within molecular axis. Spectra of the differential conductivity (dI/dV) on individual CoPc molecules revealed signatures of LUMO, HOMO, cobalt d-orbitals and HOMO-1. Asides these resonances, the dI/dV curves showed three electronic states, two around the Fermi energy and one between peaks related to HOMO-1 and HOMO, probably arising from the hybridization of either LUMO, HOMO or HOMO-1 molecular orbitals with the Cu(111) surface electronic states. Once the CoPc molecule is adsorbed on Cu(111) surface, most of its energy levels are strongly altered by the substrate surface. The direct chemical bonding of the CoPc molecule with the surface, realized at binding energy between -2 to -5 eV, led to a loss of the magnetization of the central cobalt atom. The calculated isosurface-plot possible indicates that the benzene rings and the cobalt atom provide the current paths into the tunneling process. The incommensurability of the molecular and surface symmetry leads to a different interaction between both molecular axes and the surface atoms underneath inducing therefore a reduction of molecular symmetry. Finally, the deposition of a sub-monolayer amount of CoPc molecules on cobalt nanoislands/Cu(111) system led to preferential adsorption on more reactive cobalt, either along the step edges or on top of the nanoislands, thus making the investigation by STS possible. Contrary to the Cu(111) surface, the peak position of the d-resonance of CoPc on the cobalt nanoislans was found to be deviated towards the Fermi level.

Bibliography

[1] H. de Diesbach, and E. von der Weid. Quelques sels complexes des o-dinitriles avec la cuivre et la pyridine. Helvetica Chimica Acta **10**, 886 (1927).

[2] C. C. Leznoff, and A. B. P. Lever. *Phthalocyanines. Propeties and Applications*. VHC Publishers, New York (1989-1996).

[3] J. Simon,and J. J. Andre *Molecular Semiconductors*. Springer Verlag, Berlin (1985).

[4] B. Crone, A. Dodabalapur, ,Y. Y. Lin, R. W. Filas, Z. Bao, A. LaDuca, R. Sarpeshkar, H. E. Katz, and W. Li. Large scale complementarity integrate circuits based on organic transistors. Nature **403**, 521 (2000).

[5] J. Blochwitz, M. Pfeiffer, T. Fritz, and K. Leo. Low voltage organic light emitting diodes featuring doped phthalocyanine as hole transport material. Appl. Phys. Lett. **73**, 739 (2001).

[6] R. D. Gould, and N. A. Ibrahim. The electrical response of evaporated cobalt phthalocyanine thin films on exposure to NO_2. Thin Solid Films **432**, 398 (2001).

[7] A. J. Melmed, E. W. Müller. Study the molecular pattern in the field emission microscope. J. Chem. Phys. **29**, 1037 (1958).

[8] J. K. Gimzewski, E. Stoll, and R. R. Schlittler. Scanning tunneling microscopy of individual molecules of copper phthalocyanine adsorbed on polycrystalline silver surface. Surface Science, **181**, 267 (1987).

[9] P. H. Lipel, R. J. Wilson, M. D. Miller, Ch. Wöll, and S. Chiang. High-resolution imaging of copper-phthalocyanine by scanning-tunneling microscopy. Phys. Rev. Lett. **62**, 171 (1989).

[10] C. Ludwig, R. Strohmaier, J. Petersen, B. Gompf, and W. Eisenmenger. Epitaxy and scanning tunneling microscopy image contrast of copper-phthalocyanine on graphite and MoS_2. J. Vac. Sci. Technol. B **12**, 1963 (1994).

[11] M. Böhringer, R. Berndt, and W. D. Schneider. Transition from three-dimensional to two-dimensional faceting of Ag(110) induced by Cu-phthalocyanine. Phys. Rev. B **55**, 1384 (1997).

[12] K. W. Hipps, X. Lu, X. D. Wang, and U. Mazur. Metal d-orbital occupation-dependent images in the scanning tunneling microscopy of metal phthalocyanines. J. Phys. Chem. **100**, 11207 (1996).

[13] X. Lu, K. W. Hipps, X. D. Wang, and U. Mazur. Scanning tunneling microscopy of metal phthalocyanines: d^7 and d^9 cases. J. Am. Chem. Soc. **118**, 7197 (1996).

[14] L. Scudiero, K. W. Hipps, and D. E. Barlow. A self-organized two-dimensional bimolecular structure. J. Phys. Chem. B **107**, 2903 (2003).

[15] K. Suto, S. Yoshimoto, and K. Itaya. Two-dimensional self-organization of phthalocyanine and porphyrin: dependence on the crystallographic orientation of Au. J. Am. Chem. Soc. **125**, 14976 (2003).

[16] J. Kröger, H. Jensen, N. Néel, and R. Berndt. Self-organization of cobalt-phthalocyanine on a vicinal gold surface revealed by scanning tunneling microscopy. Surface Science **601**, 4180 (2007).

[17] D. E. Barlow, L. Scudiero, and K. W. Hipps. Scanning tunneling microscopy study of the structure and orbital mediated tunneling spectra of Co(II) Phthalocyanine and Co(II) Tetraphenylporphyrin on Au(111): mixed composition films. Langmuir **20**, 4413 (2004).

[18] M. Takada, and H. Tada. Scanning tunneling microscopy and spectroscopy of phthalocyanine molecules on metal surfaces. Jpn. J. Appl. Phys. **44**, 5332.

[19] A. Zhao, Q. Li, L. Chen, H. Xiang, W. Wang, S. Pan, B. Wang, X. Xiao, J. Yang, J. G. Hou, and Q. Zhu. Controlling the Kondo effect of an adsorbate magnetic ion through its chemical bounding. Science **309**, 1542 (2005).

[20] A. Zhao, Z. Hu, B. Wang, x. Xiao, J. Yang, and J. G. Hou. Kondo effect in single cobalt phthalocyanine molecules adsorbed on Au(111) monoatomic steps. J. Chem. Phys. **128**, 234705 (2008).

[21] A. J. Heinrich, J. A. Gupta, C. P. Lutz, and D. M. Eigler. Single-atom spin-flip spectroscopy. Science **306**, 466 (2004).

[22] X. Chen, Y. S. Fu, S. H. Ji, T. Zhang, P. Cheng, X. C. Ma, X. L. Zou, W. H. Duan, J. F. Jia, and Q. K. Xue. Probing superexchange interaction in molecular magnets by spin-flip spectroscopy and microscopy. Phys. Rev. Lett. **101**, 197208, (2008).

[23] H. Bulou, and C. Goyhenex. Local strain analysis of the herringbone reconstruction of Au(111) through atomistic simulations. Phys. Rew. B, **65**, 045407 (2002).

[24] H. Bulou, and J. P. Bucher. Long range substrate mediated mass transport on metal surfaces induced by adatom clusters. Phys. Rew. Lett., **96**, 076102 (2006).

[25] J. V. Barth, H. Brune, G. Ertl, and R. J. Behm. Scanning tunneling microscopy observation on the reconstructed Au(111) surface. Atomic-structure, long range superstructure, rotational domains, and surface-defect. Phys. Rev.B **42**, 9307 (1990).

[26] Z. H. Cheng, L. Gao, Z. T. Deng, Q. Liu, N. Jiang, X. Lin, X. B. He, S. X. Du, and H. J. Gao. Epitaxial growth of iron phthalocyanine at the initial stage on Au(111) surface. J. Phys. Chem. C **111**, 2656 (2007).

[27] Z. H. Cheng, L. Gao, Z. T. Deng, N. Jiang, Q. Liu, D. X. Shi, S. X. Du, H. M. Guo, and H. J. Gao. Adsoption behavior of iron phthalocyanine on Au(111) surface at submonolayer coverage. J. Phys. Chem. C **111**, 9240 (2007).

[28] M. Takada, and H. Tada. Low temperature scanning tunneling microscopy of phthalocyanine multilayers on Au(111) surfaces. Chem. Phys. Lett. **392**, 265 (2004).

[29] A. Scarfato, S. H. Chang, S. Kuck, J. Brede, G. Hoffman, and R. Wiesendanger. Scanning tunneling microscope study of iron (II) phthalocyanine growth on metals and insulating surfaces. Surface Science **602**, 607 (2008).

[30] S. C. B. Mannsfeld, and T. Fritz. Understanding organic-inorganic heteroepitaxial growth of molecules on crystalline substrates: experiment and theory. Phys. Rev. B **71**, 235405 (2005).

[31] L. Gao, W. Ji, Y. B. Hu, Z. H. Cheng, Q. Liu, N. Jiang, X. Lin, W. Guo, S. X. Du, W. A. Hofer, X. C. Xie, and H. J. Gao. Site-specific Kondo effect at ambient temperatures in iron-based molecules. Phys. Rev. Lett. **99**, 106402 (2007).

[32] Z. Hu, B. Li, A. Zhao, J. Yang, and J. G. Hou. Electronic and magnetic properties of metal phthalocyanine on Au(111) surface: a first-principles study. J. Phys. Chem. C **112**, 13650 (2008).

[33] J. Åhlung, J. Schnadt, K. Nilson, E. Göthelid, J. Schiessling, F. Besenbacher, N. Mårtensson, and C. Puglia. The adsoption of iron phthalocyanine on graphite: a scanning tunneling microscopy study. Surface Science **601**, 3661 (2007).

[34] T. G. Gopakumar, M. Lackinger, M. Hacker, F. Müller, and M. Hietschold. Adsorption of palladium phthalocyanine on graphite: STM and LEED study. J. Phys. Chem. B. **108**, 7839 (2004).

[35] K. Nilson, J. Åhlung, B. Brena, E. Göthelid, J. Schiessling, N. Mårtensson, and C. Puglia. Scanning tunneling microscopy study on metal-free phthalocyanine monolayer structures on graphite. J. Chem. Phys. **127**, 114702 (2007).

[36] D. E. Hooks, T. Fritz, and M. D. Ward. Epitaxy and molecular organization on solid substrates. Adv. Mater. **13**, 227 (2001).

[37] A. C. Hiller, and M. D. Ward. Epitaxial interactions between molecular overlayers and ordered substrates. Phys. Rev. B **54**, 14037 (1996).

[38] M. L. M. Rocco, K. H. Frank, P. Yannoulis, and E. E. Koch. Unoccupied electronic structure of phthalocyanine films. J. Chem. Phys. **93**, 6859 (1990).

[39] G. V. Nazin, X. H. Qiu, and W. Ho. Visualization and spectroscopy of a metal-molecule-metal bridge. Science **302**, 77 (2003).

[40] M. S. Liao, and S. Scheiner. Electronic structure and bonding in metal phthalocyanines, metal=Fe, Co, Ni, Cu, Zn, Mg. J. Chem. Phys. **114**, 9780 (2001).

[41] V. Iancu, A. Deshpande, S. W. Hla. Manipulating Kondo temperature via single molecule switching. Nano Lett. **6**, 820 (2006).

[42] X. Lu, M. Grobis, K. H. Khoo, S. G. Louie, and M. F. Crommie. Spatially mapping the spectral density of a single C_{60} molecule. Phys. Rev. Lett. **90**, 096802 (2003).

[43] C. Silien, N. A. Pradhan, P. A. Thiry, and W. Ho. Influence of adsorbate-substrate interaction on the local electronic structure of C_{60} studied by low-temperature STM. Phys. Rev. B **69**, 115434 (2004).

[44] X. Lu, M. Grobis, K. H. Khoo, S. G. Louie, and M. F. Crommie. Charge transfer and screening in individual C_{60} molecules on metal substrates: A scanning tunneling spectroscopy and theoretical study. Phys. Rev. B **70**, 115418 (2004).

[45] H. Karacuban, M. Lange, J. Schaffert, O. Weingart, Th. Wagner, and R. Möller. Substrate-induced symmetry reduction of CuPc on Cu(111): an LT-STM study. Surface Science **603**, L39 (2009).

[46] S. H. Chang, S. Kuck, J. Brede, L. Lichtenstein, G. Hoffman, and R. Wiesendanger. Symmetry reduction of metal phthalocyanines on metals. Phys. Rev. B **78**, 233409 (2008).

[47] T. Brumme. *Calculation of STM spectra: Co-Phthalocyanine on metallic surfaces*. Diploma thesis, TU Bergakademie Freiberg (2008).

[48] G. A. Williams, B. N. Figgis, R. Mason, S. A. Mason, and P. E. Fielding. Structure of phthalocyanine(II) at 4.3 K. A neutron-diffraction study. J. Chem. Soc., Dalton Trans., 1688 (1980).

[49] O. Pietzsch, A. Kubetzka, M. Bode, and R. Wiesendanger. Spin-polarized scanning tunneling spectroscopy of nanoscale cobalt islands on Cu(111). Phys. Rev. Lett. **92**, 057202 (2004).

[50] L. Diekhöner, M. A. Schneider, A. N. Baranov, V. N. Stepanyuk, P. Bruno, and K. Kern. Surface states of cobalt nanoislands on Cu(111). Phys. Rev. Lett. **90**, 236801 (2003).

[51] M. V. Rastei, B. Heinrich, L. Limot, P. A. Ignatiev, V. N. Stepanyuk, P. Bruno, and J. P. Bucher. Size-dependent surface states of strained cobalt nanoislands on Cu(111). Phys. Rev. Lett. **99**, 246102 (2007).

[52] S. N. Okuno, T. Kishi, and K. Tanaka. Spin-polarized tunneling spectroscopy of Co(0001) surface state. Phys. Rev. Lett. **88**, 066803 (2002).

[53] J. A. Strocio, D. T. Pierce, A. Davies, M. Weinert, and R. J. Celotta. Tunneling Spectroscopy of bcc (001) surface states. Phys. Rev. Lett. **75**, 2960 (1995).

[54] M. V. Rastei, J. P. Bucher, P. A. Ignatiev, V. N. Stepanyuk, and P. Bruno. Surface electronic states in Co nanoclusters on Au(111): Scanning tunneling spectroscopy measurements and (ab initio) calculation. Phys. Rev. B **75**, 045436 (2007).

[55] F. Meier, K. von Bergmann, P. Ferriani, J. Wiebe, M. Bode, K. Hashimoto, S. Heize, and R. Wiesendanger. Spin-dependent electronic and magnetic properties of Co nanostructure on Pt(111) studied by spin-rezolved scanning tunneling spectroscopy. Phys. Rev. B **74**, 195411 (2006).

[56] A. L. Vazquez de Parga, F. J. Garcia-Vidal, and R. Miranda. Detecting electronic states at stacking faults in magnetic thin films by tunneling spectroscopy. Phys. Rev. Lett. **85**, 4365 (2000).

[57] M. C. Desjonqueres, and D. Spanjaard. *Concepts in Surface Physics*. 2nd Edition Springer (1996).

[58] E. Kampshoff, E. Hahn, and K. Kern. Correlation between surface stress and the vibration shift of CO chemisorbed on Cu surfaces. Phys. Rev. Lett. **73**, 704 (1994).

[59] J. H. Larsen, and I. Chorkendorff. Increased dissociation probability of CH_4 on Co/Cu(111). Surface Science **405**, 62 (1998).

[60] M. Mavrikakis, B. Hammer, and J. K. Nørskov. Effect of strain on the reactivity of metal surfaces. Phys. Rev. Lett. **81**, 2819 (1998).

[61] J. K. Nørskov. Covalent effects in the effective-medium theory of chemical binding: Hydrogen heats of solution in the 3d metals. Phys. Rev. B **26**, 2875 (1982).

[62] B. Hammer, Y. Morikawa, and J. K. Nørskov. CO Chemisorption at Metal Surfaces and Overlayers. Phys. Rev. Lett. **76**, 2141 (1996).

[63] B. Hammer and J. K. Nørskov. Theoretical Surface Science and CatalysisŮCalculation and Concepts. Advances in Catalysis **45**, 71 (2000).

[64] L. A. Kibler, A. M. El-Aziz, R. Hoyer, and D. M. Kolb. Tuning reaction rates by lateral strain in a palladium monolayer. Angew. Chem. Int. Ed. **44**, 2080 (2005).

[65] M. Ø. Pedersen, S. Helveg, A. Ruban, E. Lægsgaard, J. K. Nørskov, and F. Besenbacher. How a gold substrate can increase the reactivity of a Pt overlayer. Surface Science **426**, 395 (1999).

[66] F. Buatier de Mongeot, M. Scherer, B. Gleich, E. Kopatzki, and R. J. Behm. CO adsorption and oxidation on bimetallic Pt/Ru(0001) surfaces - a combined STM and TPD/TPR study. Surface Science **411**, 249 (1998).

Chapter 4

Electron tunneling between a spin-polarized tip and surface

This chapter starts by highlighting some of the benchmark experiments in spin-dependent electron tunneling. Follows then a presentation of the first experiment which led to the development of spin-polarized scanning tunneling microscopy (SP-STM), a reliable tool for investigating the surface magnetism of systems with reduced dimensionality down to the atomic level. The first section of the chapter ends with a discussion on SP-STM in constant-current mode. It will be shown that a higher magnetic sensitivity is gained in the images by employing spin-polarized scanning tunneling spectroscopy (SP-STS). The theoretical framework of the spectroscopic imaging mode is introduced in the second section of the chapter, which also includes a study of the spin-polarized properties of ferromagnetic cobalt nanoislands relevant for this thesis. The chapter closes with a section on the role of the tip-apex geometry in the spin-polarized electron tunneling of a tip/vacuum/surface magnetic junction. In particular, two types of geometry are discussed: a blunt tip, viewed as a surface of small area and a sharp tip, defined as one single atom added onto the surface.

4.1 Spin-dependent electron tunneling

4.1.1 Overview

Since a complete historical and conceptual background for spin-dependent electron tunneling is beyond the scope of this section, we limit our presentation to the most relevant experiments that developed this exciting research field. Spin-dependent electron tunneling was inaugurated in 1970 by the pioneering experiments of Tedrow and Meservey [1, 2, 3]. They conducted tunneling measurements on ferromagnet/insulator/superconductor (FM/I/S) tunnel junctions. A thin superconducting aluminum (Al) film was used to detect the spin-polarization of the tunneling current originating from various ferromagnetic electrodes across an alumina insulating barrier (Al_2O_3). An important step forward was done by Jullière in 1975, who reported the first conductance measurements on a ferromagnet/insulator/ferromagnet (FM/I/FM) tunnel junction [4]. Jullière proposed that the tunneling current between two ferromagnetic electrodes (Co and Fe) with different coercive fields separated by an insulator (a Ge semiconducting slab) depends on the relative orientation of the magnetization of both electrodes, which was controlled by an external magnetic field. His experiment showed that the electrical resistance of the tunnel junction was lower when the magnetizations of both ferromagnetic leads were in a parallel orientation, rather than in an antiparallel configuration ($R_P < R_{AP}$). This was the tunneling magnetoresistance effect (TMR). In order to interpret his results, Jullière proposed a simple theoretical model, which is based on two assumptions. First, he assumed that the spin of the electrons is preserved in the tunneling process. Thus, he suggested that the tunneling process of spin-up ($\uparrow$) and spin-down ($\downarrow$) electrons must be regarded as independent. Second, he assumed that the conductance for a particular spin orientation is proportional to the product of the density of states of the two ferromagnetic electrodes. According to the assumptions, the conductance for the parallel (G_P) and antiparallel (G_{AP}) alignment, can be written as follows: $G_P \propto (\Delta_\uparrow)^2 + (\delta_\downarrow)^2$ (Fig. 4.1 a) and $G_{AP} \propto \Delta_\uparrow \delta_\uparrow + \delta_\downarrow \Delta_\downarrow$ (Fig. 4.1 b), respectively, where Δ and δ represent the amplitude of the density of states for both spin-up and spin-down electrons. Considering that $\Delta >> \delta$, then $G_P \propto \Delta^2$ while $G_{AP} \propto 2\Delta\delta$. From a simple inspection, it can be seen that the conductance for a parallel (G_P) magnetizations alignment will be always greater than the conductance for an antiparallel (G_{AP}) magnetizations alignment: $G_P > G_{AP}$. Following the majority of researchers, the TMR can be defined as the conductance difference between parallel and antiparallel magnetization alignment, normalized by the conductance for

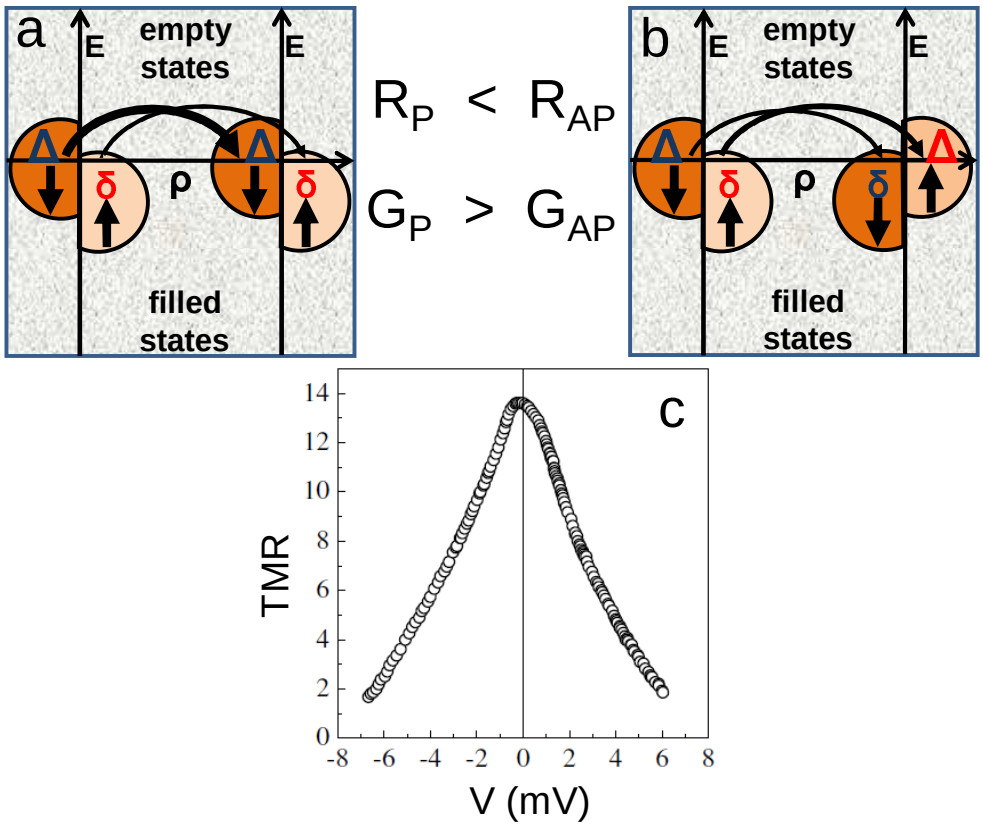

Figure 4.1: Principle of spin-polarized tunneling between magnetic electrodes that exhibit a) a parallel and b) an antiparallel magnetization. c) The original demonstration of the TMR effect. The relative conductance change due to an applied magnetic field versus applied bias in a Fe/Ge/Co junction at 4.2 K (from [4]).

antiparallel alignment, i.e:

$$TMR \equiv \frac{G_P - G_{AP}}{G_{AP}} = \frac{R_{AP} - R_P}{R_P} \tag{4.1}$$

where $G_P = 1/R_P$ and $G_{AP} = 1/R_{AP}$.

The maximum TMR was found to be about 14% at zero bias [4], but decreased very rapidly with increasing bias voltage (Fig. 4.1 c). The practical realization of a magnetic tunnel junction with a high magnetoresistance (up to 30% at 4.2 K) had to wait until 1995 once considerable progress had been made in deposition and nanopatterning techniques [5]. A magnetic tunnel junction made of an amorphous Al_2O_3 insulating layer in between two ferromagnetic metal layers reached a limit of tunnel magnetoresistance around 70% at room temperature [6]. Much

larger effects were later obtained with a single-crystal MgO barrier [7, 8].

The TMR effect in conjunction with the giant magnetoresistance (GMR) effect, discovered in 1988 by the noble price winners Albert Fert and Peter Grünberg in Fe/Cr magnetic multilayers [9] and in Fe/Cr/Fe trilayers respectively [10] have boosted the technology of magnetic storage media and brought new products in the market as: hard-disk read-heads, magnetic field sensors, magnetic memory chips, etc.. The new important field of interest that emerged in applied research, namely the analysis and characterization of high-density magnetic data storage devices together with the increasing demand of storage density in technology development, which is achievable through smaller magnetic units, have requested an advanced knowledge of the physics of magnetic nanostructures. The reduction in size and in shape goes in hand with a reduction of coordination for the magnetic atoms and leads to an important role of the underlying substrate. Therefore, the magnetic properties of nanostructures cannot be rationalized without taking into account the dimensionality, size, and shape of the nanostructures as well as the structural and electronic properties of the substrate. More than this, the study of laterally structured nanomagnetic systems (that form the TMR and GMR devices) of only one or zero dimension was hampered in that moment by a lack of an adequate magnetic imaging technique being able to provide a resolution comparable with size of entities that can be produced in a controlled fashion. At this point spin-polarized scanning tunneling microscopy (SP-STM) came into play as a powerful tool to study magnetism down to the atomic scale.

In 1990, Wiesendanger et *al.* have performed the first experiments which revealed the opportunities the scanning tunneling microscopy could provide when using spin-polarized tips [11]. The ferromagnetic/insulator/ferromagnetic tunnel junction is here replaced by a ferromagnetic tip and sample, and the insulator barrier by a vacuum barrier. Figure 4.2 a shows a measurement of step heights on the Cr(001) surface in the constant-current mode. With a non-spin-polarized tip all of the monoatomic steps were found to have the same height of 0.149 ± 0.008 nm in good agreement with the layer separation in bulk of 0.144 nm. However, when a ferromagnetic CrO_2 tip is employed, two different step heights occur in the constant-current images, 0.12 nm and 0.16 nm respectively (lower right set of height profiles in Fig. 4.2 a). This can be explained by taking into account the spin structure in the bulk of Cr. Chromium crystallizes in the cubic body centered crystal structure. The magnetic moments of the outer corner atoms of the unit cell, exhibit all antiparallel orientation relative to the magnetic moment of the center atoms of the unit cell (Fig. 4.2 b). When cutting the crystal on a (100) surface, one exposes on each terrace only surface atoms with one spin polarization. However, on neighboring terraces the

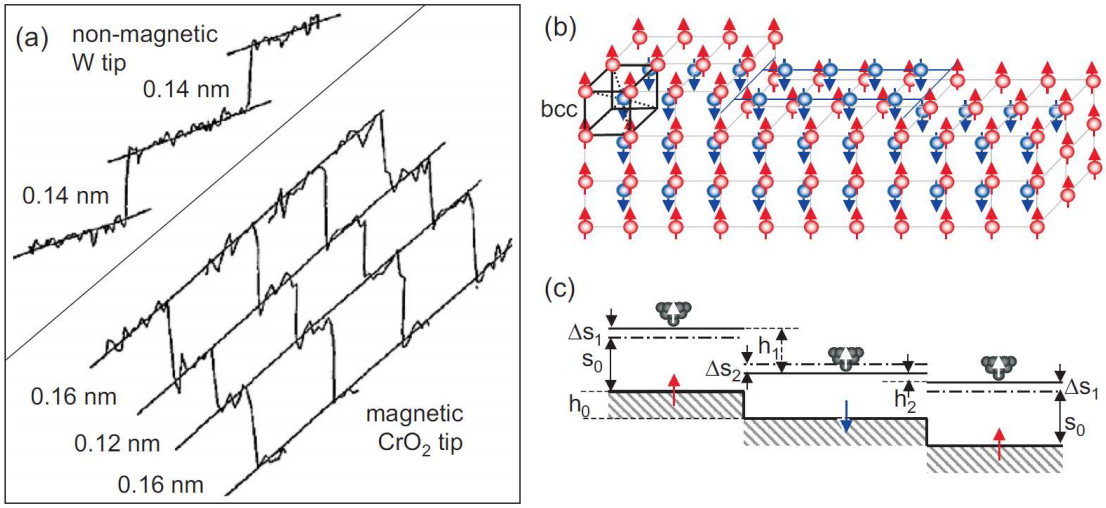

Figure 4.2: a) In the lower right corner line scans over three-layer high steps are shown. They were obtained with a spin-polarized CrO_2 tip. Two different step heights are observed. When the surface is imaged with a W tip only one step height is found (upper left corner) (from [11]). b) Topological antiferromagnetic order of the Cr(001) surface with terraces separated by monoatomic layer high steps. Different terraces are magnetized in opposite direction (from [12]). c) Schematic drawing of a ferromagnetic tip scanning over alternatively magnetized terraces separated by monoatomic-layer-high steps (step height h_0).

exposed atoms have opposite spin polarizations (magnetic moments) [12]. As a result the spin polarized current varies on terraces of opposite magnetizations, and a spin-polarized contrast appears in the topography. The tip-sample distance is either increased by Δs_1 or decreased by Δs_2 (Fig. 4.2 c). Consequently two different step heights labeled h_1 and h_2 are observed (Fig. 4.2 c). The alternating apparent step height of Cr(001) has also recently been observed with Fe coated thin film tips at a low bias voltage [13]. Another sample investigated in the constant-current mode by Wiesendanger et *al.* was the (001) surface of a natural magnetite (Fe_3O_4) single crystal. Atomically-resolved images obtained on FeO planes revealed atomic sites of different magnetic moments [14]. Later on, the potential of spin-polarized scanning tunneling microscopy (SP-STM) was exploited with great success to resolve the antiferromagnetic order of a single monoatomic layer of Mn grown pseudomorphically on W(110) surface [15].

4.1.2 The constant-current mode

Although the results mentioned above convincingly prove that spin-sensitive tunneling is possible in the constant-current mode and thus SP-STM in general, the sensitivity of this operating mode is usually limited. In the following some arguments are given to back this statement. According to Wortmann et *al.* [16] when the tip and the sample are spin-polarized, the tunneling current can be expressed within the Tersoff-Hamann [17] approximation (constant LDOS for the tip) by:

$$I(\vec{r}_T, eV) \propto \int_0^{eV} n_T n_S(\vec{r}_T, E)dE + \int_0^{eV} \vec{m}_T \vec{m}_S(\vec{r}_T, E)dE \tag{4.2}$$

where, $\vec{m}_T \vec{m}_S(\vec{r}_T, E) = m_T m_S(\vec{r}_T, E)\cos\theta(\vec{r}_T)$, with $\theta(\vec{r}_T)$ being the angle between the magnetization directions of both tip and surface. In Eq. 4.2 $n_T = \rho_T^{\uparrow} + \rho_T^{\downarrow}$ and $n_S(\vec{r}_T, E) = \rho_S^{\uparrow}(\vec{r}_T, E) + \rho_S^{\downarrow}(\vec{r}_T, E)$ are the total LDOS of the tip and sample at the location $\vec{r}_T$ of the tip, while $|\vec{m}_T| = \rho_T^{\uparrow} - \rho_T^{\downarrow}$ and $|\vec{m}_S(\vec{r}_T, E)| = \rho_S^{\uparrow}(\vec{r}_T, E) - \rho_S^{\downarrow}(\vec{r}_T, E)$ are aligned with the magnetization of the tip, $\vec{M}_T = \int_{-\infty}^{0} \vec{m}_T(E)dE$ and of the sample, $\vec{M}_S(\vec{r}_T) = \int_{-\infty}^{0} \vec{m}_S(\vec{r}_T, E)dE$, respectively. Note that $\vec{m}_T$ and $\vec{m}_S(\vec{r}_T, E)$ are aligned with their corresponding magnetization, but do not necessarily have the same orientation as their magnetization. Thus it is possible that the tunnel current can be increased (decreased) even though the magnetizations of both tip and sample are antiparallel (parallel). All energies in the Eq. 4.2 are taken with respect to E_F. Here, above, $\rho_T^{\uparrow}$, $\rho_T^{\downarrow}$ and $\rho_S^{\uparrow}(\vec{r}_T, E)$, $\rho_S^{\downarrow}(\vec{r}_T, E)$ represent the density of states for both spin orientations ($\uparrow$ and $\downarrow$) of tip and sample, respectively. Using the following relations:

$$\mathcal{N}_S(\vec{r}_T, eV) = \int_0^{eV} n_S(\vec{r}_T, E)dE \tag{4.3}$$

and

$$\vec{\mathcal{M}}_S(\vec{r}_T, eV) = \int_0^{eV} \vec{m}_S(\vec{r}_T, E)dE \tag{4.4}$$

which represent the energy-integrated LDOS of the sample at the location $\vec{r}_T$ of the tip and the vector of energy-integrated spin-polarized LDOS of the sample [$\vec{\mathcal{M}}_S(\vec{r}_T, eV) \rightarrow -\vec{M}_S(\vec{r}_T)$, when $eV \rightarrow -\infty$], respectively, Eq. 4.2 can be rewritten as:

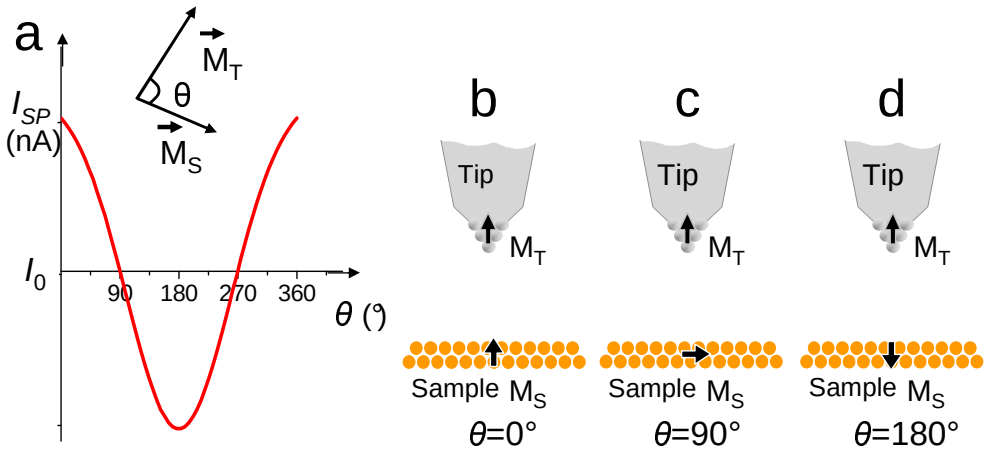

Figure 4.3: a) Angular dependence of the spin-polarized current I_{SP}. Sketch of a: b) parallel, c) orthogonal and d) antiparallel alignment of the spin-polarized electrodes.

$$I(\vec{r}_T, eV) \propto n_T \mathcal{N}_S(\vec{r}_T, eV) + \vec{m}_T \vec{\mathcal{M}}_S(\vec{r}_T, eV) \propto I_0(\vec{r}_T, V) + I_{SP}(\vec{r}_T, eV, \theta) \tag{4.5}$$

Equation 4.5 contains the sum of two terms, a contribution which is not spin-polarized (I_0) and a contribution which is spin-polarized (I_{SP}). In the case of non-spin-polarized STM experiments, i.e., using either a non-spin-polarized tip or sample, the second term, I_{SP} in the Eq. 4.5 vanishes and the current reduces to the result of the Tersoff-Hamann model [17] (§ 2.3.1). Since, in general, tip and sample will not share the same magnetization axis, the cosine of the angle θ between the magnetization directions of both tip and sample enters in Eqs. 4.2 and 4.5. Whereas the magnetization direction of the tip can be assumed fix, in most cases the sample magnetization may change as a function of position, and accordingly the angle between them is a function of the lateral tip position, $\theta = \theta(x, y)$. Figure 4.3 a shows the angular dependence of the I_{SP} for two spin-polarized electrodes displayed as the sample surface and the STM tip. The spin-polarized contribution is maximal for a collinear configuration $\vec{M}_T \parallel \vec{M}_S$, i.e. θ=0° for the parallel case (↑↑) (Fig. 4.3 b), or θ=180° for the antiparallel case (↑↓) (Fig. 4.3 d), while it vanishes for $\vec{M}_T \perp \vec{M}_S$, i.e. θ=90° (Fig. 4.3 c). This also agrees with Jullière's predictions.

4.1.3 Loss of magnetic contrast

According to Eq. 4.5, the total current, I, in SP-STM is governed by the energy integrated quantities $\mathcal{N}_S$ and $\vec{\mathcal{M}}_S$. The non-polarized part (I_0) of the total tunneling current or $\mathcal{N}_S$ increases monotonously with increasing bias voltage (V), while the polarized part (I_{SP}) or $\vec{\mathcal{M}}_S$ may stay constant; thus the constant current image will be dominated by I_0 when moving away from the Fermi level. As an example we can consider the spin-polarized contrast obtained by imaging in constant-current mode cobalt nanoislands grown on Au(111). It was shown that an amount of 0.3 monolayers of cobalt atoms dropped on Au(111) kept at room temperature gives rise to nanoislands two-atomic-layer high [18, 19, 20]. These self-organized cobalt nanoislands (Fig. 5.7 a) possess an easy-magnetization axis perpendicular to the Au(111) surface with either a up or down magnetization [21, 22]. When employing bulk ferromagnetic Ni tips magnetized perpendicularly to the surface plane [23], the constant current SP-STM image showed a bimodal distribution (Fig. 5.7 c) of the nanoislands apparent heights (Fig. 5.7 b). The spin-polarized contrast discernible in the apparent height between cobalt nanoislands with opposite polarization is typically $\Delta z = 0.28$ Å (Fig. 5.7 c). Cobalt nanoislands grown on Cu(111) (Fig. 4.6 a) apparently do not exhibit a spin-polarized contrast in constant-current mode. Even though a magnetic tip is employed, the constant current SP-STM image taken at -0.35 V exhibits a unique nanoislands apparent height of $z = 4$ Å. A possible explanation for this difference can be given by recalling that the intensity of the spin-polarized contrast obtained in constant current mode for bilayer cobalt nanoislands can be correlated with their spin-polarized electronic properties. The cobalt nanoislands of hcp and fcc stacking are characterized by a surface state having a spin-polarized nature and located at -0.28 V and -0.35 V, respectively (§ 3.2.1). For the self-organized cobalt nanoislands on Au(111) this surface state is shifted toward Fermi level up to either -0.15 V or -0.085 V depending on the stacking order [24]. Supposing that the magnetic contrast $\Delta I_{SP} = I_{SP,\uparrow} - I_{SP,\downarrow}$ [where $I_{SP,\uparrow}$ and $I_{SP,\downarrow}$ are the spin-polarized current for parallel (Fig. 4.3 b) and antiparallel (Fig. 4.3 d) case, respectively] has the same value for the cobalt nanoislands grown on both Au(111) and Cu(111) surface, the ratio $\Delta I_{SP}/I_0$ decreases as bias voltage (V) increases, and thus the intensity of the spin-polarized contrast depends on the position of the spin-polarized surface state relative to Fermi level. In the case of the cobalt nanoislands grown on Au(111) surface, a bias voltage of -0.2 V is enough to efficiently tunnel in its spin-polarized surface states and thus, a spin-polarized contrast is obtained in the constant-current image (Fig. 5.7 b). However on Cu(111), one needs to increase the bias voltage up to

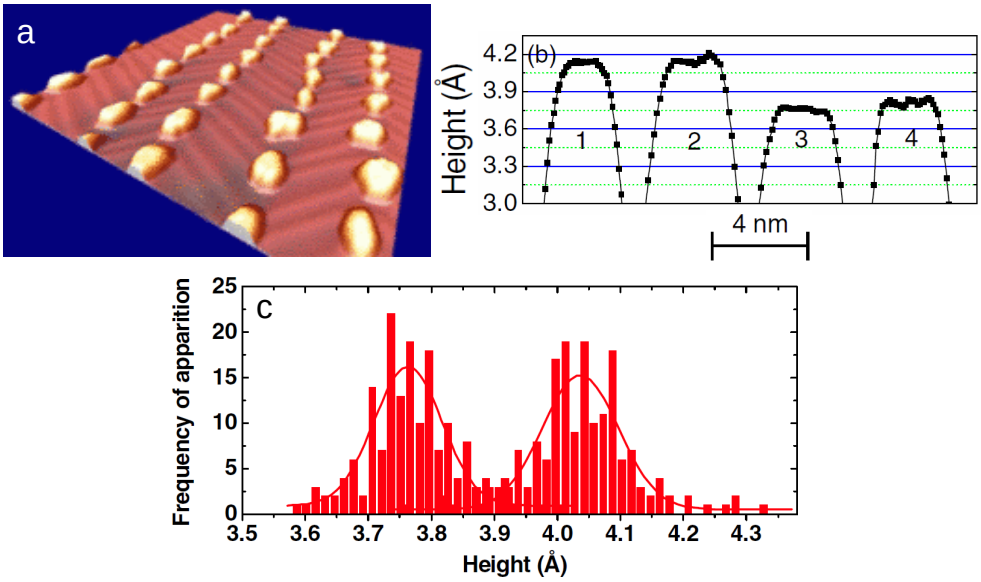

Figure 4.4: a) Constant-current STM image of self-organized Co nanoislands on Au(111) (Scan size : 42×42 nm^2; Tunneling parameters: $V = -0.215$ V, $I = 0.25$ nA). b) Cross section over four spin-polarized Co nanoislands. c) Histogram over many images of the height distribution obtained with the spin-polarized Ni tip, clearly showing two peaks separated by $\Delta z \approx 0.28$ Å (from [23]).

-0.35 V, leading to an increase of I_0. Consequently, the spin-polarized contrast is lost. With increasing bias voltage, the expected spin-polarized contrast of $\Delta z = 0.2$ Å for these nanoislands is gradually annihilated up to a complete cancellation. Aside the above effect, one needs to account for the noise level, which can be higher than the magnetic corrugation. Therefore, the constant-current mode of SP-STM employed, especially away from the Fermi level not well suited for a clear separation between topological and spin-polarized contributions to the measured signal. In order to reveal atomic-scale spin structure it is preferable to image perfect flat surfaces at low biases (a few mV) and high tunneling currents (tens of nA). For a higher spin sensitivity it is therefore desirable to turn to the spin-polarized differential conductivity, which will be presented in the next section of this chapter.

4.2 Spin-polarized scanning tunneling spectroscopy

4.2.1 Using the differential conductance

The difficulties of separating electronic from spin-polarized information can be overcome by measuring the local differential conductance dI/dV with a spin-polarized tip. It allows to find out the energy range of high polarization. Within the spin-polarized tunneling model the differential conductance (the LDOS of tip being again assumed constant) [16] is:

$$\frac{dI}{dV}(\vec{r}_T, eV) = n_T n_S(\vec{r}_T, eV) + \vec{m}_T \vec{m}_S(\vec{r}_T, eV) \tag{4.6}$$

The differential conductance, given by the Eq. 4.6, is directly proportional to n_S and $\vec{m}_S$ at an energy eV, contrary to Eq. 4.5 where the tunneling current is governed by the energy integrated quantities $\mathcal{N}_S$ and $\vec{\mathcal{M}}_S$. As mentioned and shown in the previous section of this chapter, in the constant-current mode, I_0 increases with V while the spin-polarized contribution may stay constant. On the contrary, in spectroscopic dI/dV measurements the voltage can be adjusted as to maximize the spin-polarized contribution $\vec{m}_S$ over the spin averaged contribution n_S. The voltage for such a range of high polarization can be extracted from spectral curves measured on oppositely magnetized nanostructures (Fig. 4.6 b). Even if the differential conductance dI/dV in the spin-polarized measurement is also separated in an unpolarized (spin-averaged) part and a spin-polarized part (Eq. 4.6), the sensitivity of the SP-STS mode is higher than the constant-current mode because the spin-poalrized contrast is directly correlated to the spin-polarized part of the differential conductance, and not obtained from the logarithmic dependency of the tunnel current on the tip-sample separation. Thus, the SP-STS approach is particularly suited to image the spin-polarized contrast of nanostructures by selectively probing features of the local density of states exhibiting a high spin polarization. The two modes of the SP-STM operation are schematically represented in Fig. 4.5.

Historically, the spin-polarized scanning tunneling spectroscopy (SP-STS) was first demonstrated on the exchange-split surface state of ferromagnetic Gd(0001) thin films, using ferromagnetic iron (Fe) probe tips in a low-temperature scanning tunneling microscope operated at 20 K [25]. Further, the SP-STS was employed to study the spin-polarized properties of nanoparticles. The nanoscale iron islands with a height of two atomic layers, grown on a stepped W(110) surface were the first exploited by SP-STS [26]. Recently, the SP-STS demonstrated its ability to detect stationary spin-polarized states of individual magnetic adatoms adsorbed on a magnetic

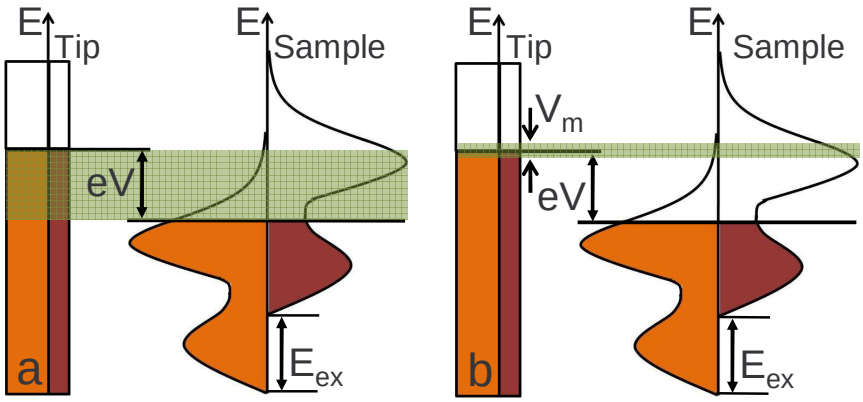

Figure 4.5: a) Constant-current measurement. All the states in the interval $E_F, E_F + eV$ and indicated by the green-shaded area contribute to the signal. b) Spectroscopy measurement. The dI/dV signal is acquired at $E = eV$ as indicated by narrow green-shaded area.

[27] or a nonmagnetic [28] metallic substrate, respectively. In the following the SP-STS will be applied to magnetic cobalt nanoislands grown on Cu(111) surface, whereas in Chapter 5 of this thesis the SP-STS will be extended to individual cobalt-phthalocynanine molecules residing on magnetic cobalt nanoislands. Hereafter we focus on the SP-STS of the cobalt nanoislands.

4.2.2 SP-STS of cobalt nanoislands

In order to be able to identify the spin-polarized contribution to the dI/dV signal one must first understand the electronic properties of the cobalt nanoislands by using a non-spin-polarized probe tip. As a matter of fact, in § 3.2.1, we have seen that the spectrum, acquired in the middle of either fcc or hcp cobalt nanoisland with a tungsten (W) tip, is dominated in its negative part by a strong peak caused by an occupied d_{z^2}-like state of minority character. Within measurement accuracy, no variation between spectra acquired on different cobalt nanoislands of the same size and stacking was found. In contrast, when a spin-polarized tip is used, a significant variation between different cobalt nanoislands of same size and stacking shows up. Namely, two distinct spectra for each cobalt nanoislands type is found, which will hereafter be referred to as $\uparrow$ and $\downarrow$. Figure 4.6 b (upper panel) shows only the spectra acquired on cobalt nanoislands of hcp stacking and marked by X in the topographic image (Fig. 4.6 a). Both spectra are identical as far as the positions of the main peak is concerned, but differ in intensity. While the differential conductivity at the peak position amounts to only $dI/dV = 11$ nS for

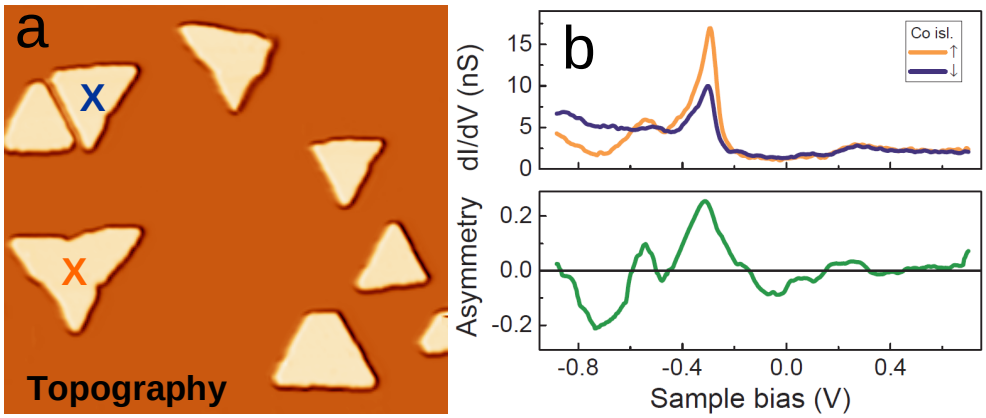

Figure 4.6: a) Constant-current SP-STM image of Co nanoislands on Cu(111) recorded with spin-polarized Co-coated Ni tip at 4.6 K (Scan size : 90×76 nm^2; Tunneling parameters: $V = -0.35$ V, $I = 1.0$ nA). b) upper panel: Typical spin-polarized dI/dV over two Co nanoislands of opposite polarization (noted $\uparrow$ and $\downarrow$). Feedback loop opened at 0.6 V and 0.5 nA. bottom panel: Asymmetry arising from opposite spin-polarization of the cobalt nanoislands.

the spectra of type $\downarrow$, it is enhanced by about 35% to $dI/dV = 17$ nS for type $\uparrow$. The relative intensities between both types of spectra invert for below -0.6 V. The variation in the two spectra is caused by spin-polarized tunneling between the spin-polarized tip and the magnetic cobalt nanoisland. According to Eq. 4.6 the two spectra correspond then to different orientations of the tip and sample magnetizations. However, since the spin-polarized contrast depends on the bias we cannot identify which cobalt nanoislands have a magnetization parallel to the tip magnetization and which have a magnetization antiparallel. The differential conductivity can be performed over each pixel of the topographic image (Fig. 4.6 a), the resulting image being a so-called dI/dV map (§ 2.3.3). If the dI/dV map is realized at a sample bias of -0.28 V, where the conductance differs strongly between two spin orientations, a spin-polarized contrast is obtained. The nanoislands appear as bright yellow in Fig. 4.7 a, or dark yellow. A reversal in the spin-polarized contrast is revealed if recording a dI/dV map at a lower sample bias (-0.72 V): the nanoisland which previously was bright, is now dim and vice versa (Fig. 4.7 b).

Based on the spectra presented in the upper panel of Fig. 4.6 b the experimental asymmetry can be estimated by:

$$A(V) \equiv \frac{dI/dV_{\uparrow}(V) - dI/dV_{\downarrow}(V)}{dI/dV_{\uparrow}(V) + dI/dV_{\downarrow}(V)} \tag{4.7}$$

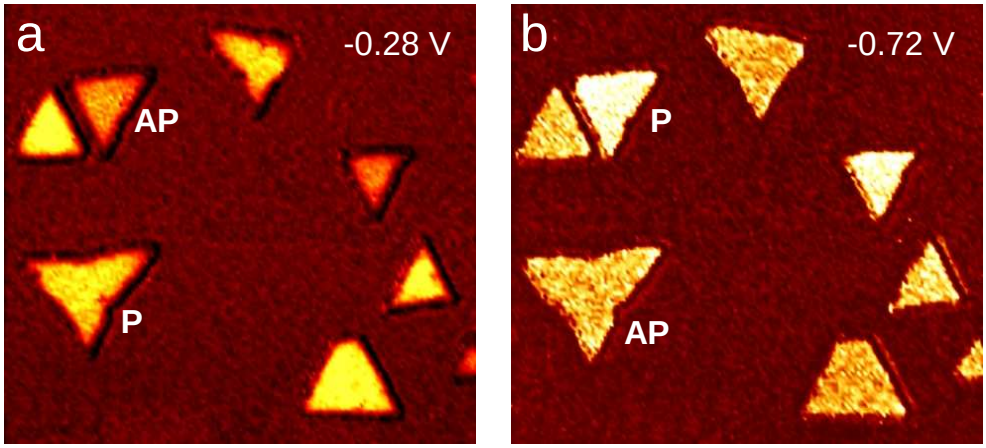

Figure 4.7: Spin-polarized dI/dV maps of cobalt nanoislands at a) -0.28 V and b) -0.72 V.

where $dI/dV_{\uparrow(\downarrow)}(V)$ is the intensity of the dI/dV signal measured above opposite spin-polarized cobalt nanoislands $(\uparrow,\downarrow)$ with respect to the magnetic tip. The result is shown in the bottom panel of Fig. 4.6 b. The asymmetry exhibits a maximum positive value at a sample bias of -0.28 V (at bias voltage just bellow the main peak position of the surface state) and a minimum negative value at -0.61 V, which results in images of opposite contrast (Fig. 4.7 a and Fig. 4.7 b). A strong oscillatory behavior is observed over the whole energy range with a sign reversal of the spin polarization occurring at 0.31 V, 0.14 V, -0.14 V, -0.45 V, -0.50 V -0.59 V and -0.87 V. Accordingly, the spin-polarization of the magnetic junction varies with bias voltage.

4.2.3 The spin-polarized tip

It was confirmed by measurements under a external applied magnetic field that these cobalt nanoislands are ferromagnetic with strong perpendicular magnetic anisotropy [29]. An out-of-plane magnetization was also found for the two-layer-high cobalt nanoislands grown on the Pt(111) surface [30, 31]. In order to be sensitive to the perpendicular sample magnetization, the tip apex should be magnetized perpendicular to its axis. In the previous studies on cobalt nanoislands grown on a Cu(111) surface, a polycrystalline tungsten (W) tip coated with an antiferromagnetic chromium (Cr) film of 75 ± 50 monolayers thickness was used to provide magnetic sensitivity [29, 32]. In this thesis for the out-of-plane spin-resolved measurement, Co-coated Ni tips were employed. The polycrystalline Ni wires were chemically etched *ex*

situ and then cleaned *in situ* by annealing and argon ion bombardment. The Ni tips were then magnetically coated by electron beam evaporation with a few monolayers of Co and subsequently magnetized by fields directed parallel to the tip axis produced by a magnet (0.3 T) resulting in a sensitivity to the perpendicular component of sample magnetization. During the experiments we have seen that among 10 prepared tips, only one tip had a proper sensitivity to the perpendicular component of the sample magnetization. This implies a time ranging from a few days to a full month for fulfilling the conditions necessary to obtained spin-polarized dI/dV maps (Fig. 4.7 a and 4.7 b).

Bulk ferromagnetic tips produce a stray field, which can potentially cause field-induced magnetization reversals of the nanostructures under investigation. However the stray field can be minimized by using tips either covered with a magnetic thin film with a thickness comparable to or lower than the tip-sample distance or made of a material exhibiting a low saturation magnetization [33]. In the case of a few monolayers Co-coated Ni tips, both conditions are fulfilled. It was shown experimentally that massive Ni tips with such characteristics, do not perturb the magnetization state of Co nanoislands self-organized on the Au(111) surface [23]. Another advantage of the cobalt coating for the present study is uniformization of the material employed in the magnetic tunnel junction. Based on this idea, we have also chosen cobalt phthalocyanine as the molecule to place in between the two cobalt magnetic electrodes.

From the above results it can be deduced that these cobalt nanoislands coexist in two states of opposite spin: with their collective spins pointing either up or down. The tip of scanning tunneling microscope is sensitive to both states and potentially sensitive to the spin states of single objects hosted on the nanoislands. The spin of these objects, i.e. atoms or molecules can either align or anti-align with the underlying nanoisland collective spins. In this way, spin transport can be studied across individual atoms and molecules. The first attempt in this direction has been done by Yayon et *al.* [27]. They could observe stationary spin-polarized states of individual iron and chromium atoms deposited onto the cobalt nanoislands. Current flowing from the adatoms into the STM tip is larger or smaller depending on whether the tip spin-polarization is aligned parallel or antiparallel to the polarization of the individual magnetic adatoms being probed. The origin of these stationary spin-polarized states has been studied both experimentally and theoretically by Heinrich et *al.* [36].

4.3 Influence of tip-structure on the magnetic junction

4.3.1 Experimental versus theoretical asymmetry

As evidenced in the previous sections the scanning tunneling microscope constitutes an ideal model magnetic junction to perform spin-polarized electron tunneling experiments. The ultra-high vacuum environment and the low temperature provides an ultra-clean and stable environment, in which the TMR effect is produced across a simple vacuum barrier, whose width can be controlled in a precise way. Moreover the atomic resolution of the SP-STM allows to directly perform spin-dependent tunneling across very small objects such as individual atoms and molecules. With the recent development of subkelvin microscopes, it has also become possible to get single-spin sensitivity, i.e. to study the ground-state of single magnetic atoms and to probe the magnetic interactions at extremely small energy scales simultaneously [28, 34, 35].

SP-STM also presents a strong structural asymmetry between the two magnetic electrodes. If one of them can be chosen as atomically flat (the surface) the other one, the tip, can have different geometries. Although one can judge whether the tip apex is atomically sharp through the images, the real structure (nearest neighbors, next nearest neighbors, etc. of the apex atom) is unknown. The variation of the tip apex geometry induces changes of its electronic structure in the energy range of interest. Moreover, according to the Jullière model, the TMR effect is derived from the density of states of two magnetic leads (surface and tip) [4]. Therefore, the uncertainty of the tip apex geometry and its effect on the density of states at the Fermi level will influence the TMR effect in the SP-STM magnetic junction. In order to illustrate this, four experimental magnetic asymmetries obtained by spin-dependent tunneling into cobalt nanoislands of opposite polarization with four different spin-polarized Co-coated Ni tips are plotted in Fig. 4.8. As can be observed, in the positive bias range the magnetic asymmetries follow a quite similar oscillatory behavior. Strong differences occur in the negative bias range. The typical oscillatory behavior is preserved, but the sign reversal of the spin-polarization changes from five to three times. The distinct maxima occurring close to the energetic position (-0.28 V) of the dominant peak (label 1) of minority character exhibits different values suggesting that the four spin-polarized tips may give different spin-polarized contrast. Instead, the distinct minima not only change their values but shift in energy. From the above observations it appears that the magnetic asymmetry of the magnetic tunnel junction, in particular in the negative bias range, is very sensitive to the modification of the Co tip-apex

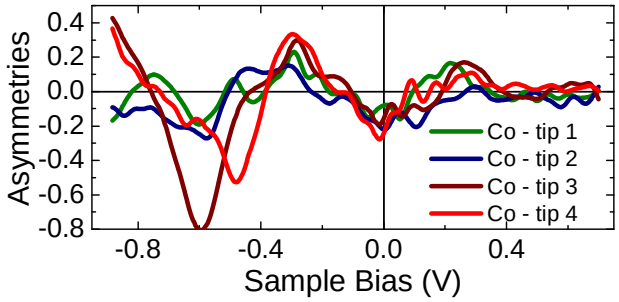

Figure 4.8: Experimental magnetic asymmetries arising from opposite polarization of the cobalt nanoislands recorded with four different spin-polarized Co-coated Ni tips.

geometry.

To further illustrate the decisive role of the atomic configurations of the tip apex on the magnetic asymmetry, or polarization of a magnetic tunnel junction, we have performed calculations using a simple model. We consider two particular configurations of the magnetic tunnel junction, which reflect two different geometries of the tip. The first magnetic tunnel junction consists of a blunt cobalt tip, a vacuum spacer and a cobalt nanoisland (Fig. 4.9 a). A blunt tip, shown in Fig. 4.9 a, can involve several atoms forming an atomically flat surface at the tip apex. For this reason, one can geometrically model the blunt tip apex as being a cobalt nanoisland placed on a Cu(111) surface. Thus, similar to a planar magnetic tunnel junction, one can suppose that the spin-polarized tunneling current in a SP-STM magnetic junction with a blunt magnetic tip occurs between two atomically flat magnetic cobalt nanoislands. Very often, in a STM experiment, a "sharp" tip is desirable rather than a blunt one for an improved spatial resolution. This is required, especially, when single atoms or molecules are to be probed. Therefore, in the second magnetic tunnel junction we employ a "sharp" magnetic tip, a vacuum spacer and a cobalt nanoisland (Fig. 4.9 b). The "sharp" tip is obtained by adding a single cobalt atom on the surface of a blunt cobalt tip. The geometry of a "sharp" magnetic tip, can be regarded as being equivalent with an magnetic adatom sitting in the middle of a cobalt nanoisland (Fig. 4.9 b). Since the tunneling current is exponentially dependent on the tip-surface distance, most of the spin-polarized tunneling current is carried between the magnetic apical atom and the surface.

In the discussion made so far, the tip has been assumed as being electronically featureless, i.e. both the LDOS as well as spin-polarization were considered constant over the voltage range of interest. However, real tips are likely to posses a nontrivial energetic structure. Thereby,

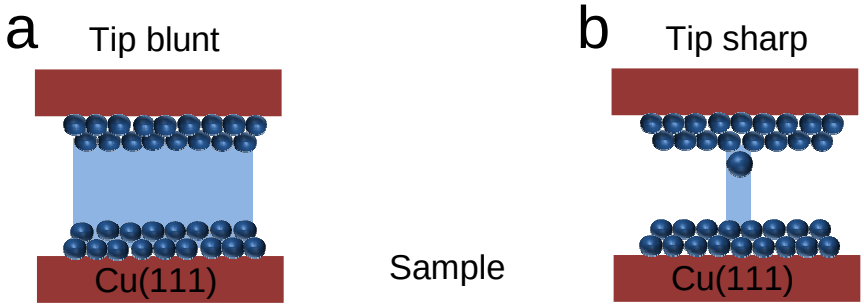

Figure 4.9: Sketch of magnetic tunnel junction consisting of a cobalt a) blunt tip or b) sharp tip, vacuum barrier and a cobalt flat surface.

in our reasoning, we have taken into account a non-constant tip LDOS. In such conditions, Eq. 4.2, which gives the tunneling current inside the magnetic tunnel junction, becomes:

$$I(\vec{r}_T, eV) \propto \int_0^{eV} n_T(\vec{r}_T, E - eV) n_S(\vec{r}_T, E) dE + \int_0^{eV} \vec{m}_T(\vec{r}_T, E - eV) \vec{m}_S(\vec{r}_T, E) dE \quad (4.8)$$

where $\vec{m}_T(\vec{r}_T, E - eV)\vec{m}_S(\vec{r}_T, E)$ are either parallel (Fig. 4.3 b) or antiparallel (Fig. 4.3 d). Based on the Eq. 4.7, the asymmetry of the differential conductivity dI/dV can be expressed as:

$$A(V) \equiv \frac{\frac{d}{dV}\int_0^{eV} \vec{m}_T(\vec{r}_T, E - eV)\vec{m}_S(\vec{r}_T, E)dE}{\frac{d}{dV}\int_0^{eV} n_T(\vec{r}_T, E - eV) n_S(\vec{r}_T, E)dE} \quad (4.9)$$

Note that in the above equation, $\vec{r}_T$ is the position of the tip apex with respect to the surface plane and n_T represents the LDOS of the tip, while n_S is the sample LDOS at the tip position. The total LDOS of both minority and majority character for the tip and the sample has been provided by the Pavel A. Ignatiev from the group of Prof. Patrick Bruno and Dr. Valeri Stepanyuk at the Max Planck Institute of Microstructure Physics of Halle, Germany. *Ab initio* calculations based on the density functional theory implemented in the multiple-scattering KKR Green's function method were conducted, improved by employing the full potential approximation. In the calculations, the cobalt nanoisland is treated as an infinite cobalt bilayer of either hcp or fcc stacking placed on a semi-infinite Cu(111) substrate. The LDOS for the blunt tip is presented in Fig. 4.10 a, while the LDOS for the atomically "sharp"

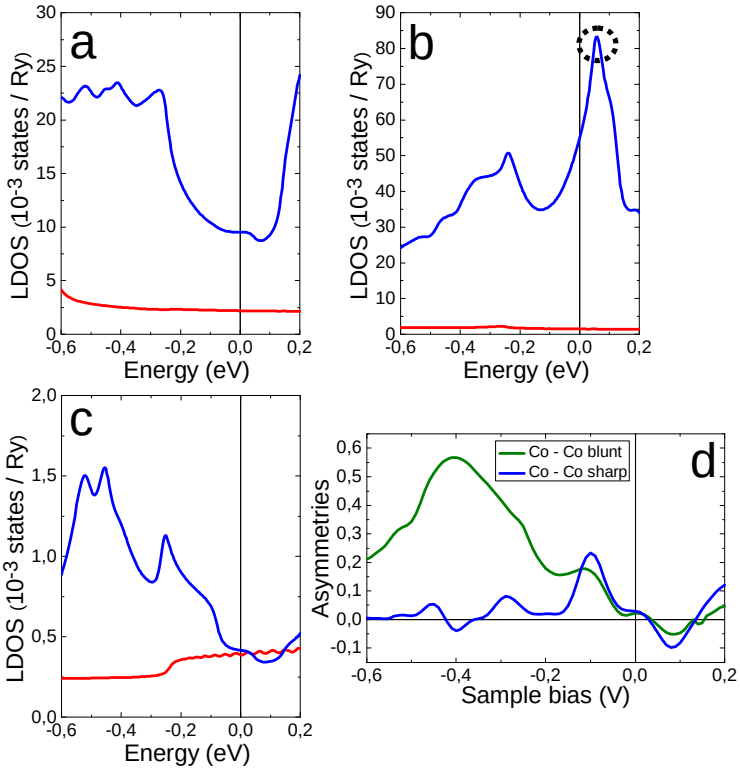

Figure 4.10: Calculated spin-polarized LDOS of a) a hcp cobalt nanoisland mimicking a blunt tip in our model. b) an atom on a cobalt nanoisland mimicking a sharp tip in our model. c) a hcp cobalt nanoisland at $|\vec{r}_T| = 0.63$ nm in vacuum. (minority in red and majority in blue) d) Calculated magnetic asymmetries corresponding to both blunt and sharp tip.

tip is presented in Fig. 4.10 b. Figure 4.10 c represents the LDOS of the cobalt nanoislands in vacuum. i.e at position $\vec{r}_T$. These LDOS are the relevant quantities needed to evaluate the asymmetry of Eq. 4.9, the distance $|\vec{r}_T|$ being 0.63 nm. Over the energy range of interest, the LDOS of the blunt tip (Fig. 4.10 a) is dominated by d-states of minority character (blue curve). The majority contribution, instead comes from sp-states that have a negligible amplitude (red curve) compared to the minority d-states. The LDOS of the "sharp" tip (Fig. 4.10 b) is as well dominated by d-states of minority character, which have an amplitude three times higher than those of the blunt tip. They are composed of surface-induced states and atomic-like states [36]. In particular, the dominant peak in the positive energy range close to Fermi level (denoted by the dotted black circle in Fig. 4.10 c) is a atomic-like d_{z^2} resonance. The LDOS of the sample is also dominated by d-states of minority character, the majority states being of sp-character. Fig. 4.10 a and 4.10 c, which depict the LDOS of the nanoislands at the surface position and

in vacuum, may be linked by remarking that the d-states decay faster into vacuum compared to sp-states. Therefore the ratio between majority and minority channels changes between the two LDOS, the decay favoring the spin-polarized majority channel.

The two integrals appearing in the expression of the asymmetry (Eq. 4.9) were calculated using Maple software over a voltage range of -0.6 V to 0.2 V. In Fig. 4.10 d are plotted the two magnetic asymmetries calculated according to Eq. 4.9 for both magnetic tunnel junctions sketched in Fig. 4.9 a and 4.9b. It can be observed that both magnetic asymmetries have a similar behavior in the positive voltage range, while in the negative part they behave differently. The magnetic asymmetry calculated for a blunt tip presents a positive value, while the magnetic asymmetry for the "sharp" tip has an oscillatory behavior, with, remarkably, a sign reversal occurring at -0.35 V and -0.42 V in rough accordance with the experimental data of Fig. 4.8. The differences probably arise from the atomic-like resonance appearing in the LDOS of the "sharp" tip and absent in the LDOS of the blunt tip. Both magnetic asymmetries differ also in intensity for this voltage range, suggesting that the blunt cobalt tip may give a higher spin-polarized contrast between two cobalt nanoislands with opposite magnetization than the "sharp" cobalt tip. Overall, this simple model proves that the spin-polarized contrast depends crucially on the tip apex geometry.

Despite this encouraging result, further improvements of the model are necessary. Indeed, inaccuracies may arise from $1.)$ an inaccurate modeling of the tip-apex geometry, and $2.)$ the Tersoff-Hamman approach used in our calculations. It is likely that the apex of the tip might be composed of a cluster of either pyramidal or tetragonal, or a more complex shape. These apices may possess atomic-like resonances falling at different energies depending on their respective geometry, and a tip-dependent magnetic asymmetry may arise then as seen experimentally in Fig. 4.8. Concerning the Tersoff-Hamman approximation, one should recall that the differential conductance depends on the tunneling transmission matrix [37], which we have neglected so far:

$$\frac{dI}{dV} \propto \sum_{\nu,\mu} |M_{\mu\nu}|^2 \delta(E_\mu^L - E_\nu^R)\delta(E_\mu^L - E_F) \tag{4.10}$$

with

$$M_{\mu\nu} = \frac{\hbar}{2m} \int \int_S (\psi_\mu^{L^*} \nabla \psi_\nu^R - \psi_\nu^R \nabla \psi_\mu^{L^*}) dS \tag{4.11}$$

In the above equations, ψ_ν^R (ψ_μ^L) is the eigenfunction for the right (left) electrode corresponding to energy $E_\nu^R(E_\mu^L)$. These matrix elements depend on the states involved in the tunneling process (s, p_z, d_{z^2}, etc. [38]) and on the spin. This introduces in the tunneling current selection rules based on symmetry as we show in the next paragraph. More importantly, the matrix elements and therefore the transmission probability linked to it, will depend on the relative orientation of the magnetization of both tip and sample, and an oscillatory behavior of the magnetic asymmetry of the tunnel junction is then possible.

4.3.2 Towards a realistic model

An attempt to describe the origin of the magnetoresistance occurring in a SP-STM junction, from a theoretical point of view, was done by Enkovaara et *al.* [39]. They have considered a Fe/vacuum/Cr tunnel structure oriented in the (001) direction with an antiferromagnetic Cr blunt tip. Their calculations are based on two approaches: $1.)$ Motivated by the fact that both electrodes have localized surface states [40], the authors calculate the conductance of the magnetic junction within a Bardeen tunneling Hamiltonian formalism [41]. $2.)$ The spin-resolved transmission probability encompasses electronic states having the same symmetry on both sides of the barrier [42, 43]. The role of the symmetry is to determine the number of nodes of the wave function in the plane perpendicular to the decay direction. The s-like states have therefore smaller attenuation rate, while the p-like states with more nodes are more attenuated and the d-like states typically even more. Following this symmetry criteria one can regroup the atomic orbitals as follow: the Δ_1 symmetry regrouping s, p_z, d_{z^2} orbitals, the Δ_5 regrouping p_x, p_y, d_{xz}, d_{yz}, the Δ_2 regrouping $d_{x^2-y^2}$ and the $\Delta_{2'}$ regrouping d_{xy}. The attenuation or the decay of the electronic wave function into the vacuum for the symmetries will be different and follow: $\Delta_1 < \Delta_5 < \Delta_{2,2'}$.

As can be seen in the Fig. 4.11, the Δ_1 bands (which decay slowest into the vacuum) start at the $\overline{\Gamma}$-point at binding energies around -1.0 eV ($+1.5$ eV) for Fe majority (minority) bulk states, and 1.1 eV for Cr, and are dispersing upwards in energy. In the case of Cr, the Δ_1 band is spin-degenerated. Additionally, the surface states of both magnetic electrodes are of Δ_1 symmetry as well. Owing to the surface magnetism of Cr, its surface states are exchange split. In the parallel magnetic alignment, the Δ_1 band of the Fe majority bulk states start to overlap with the Δ_1 band of Cr bulk states at around 1.1 eV above Fermi level. At this energy

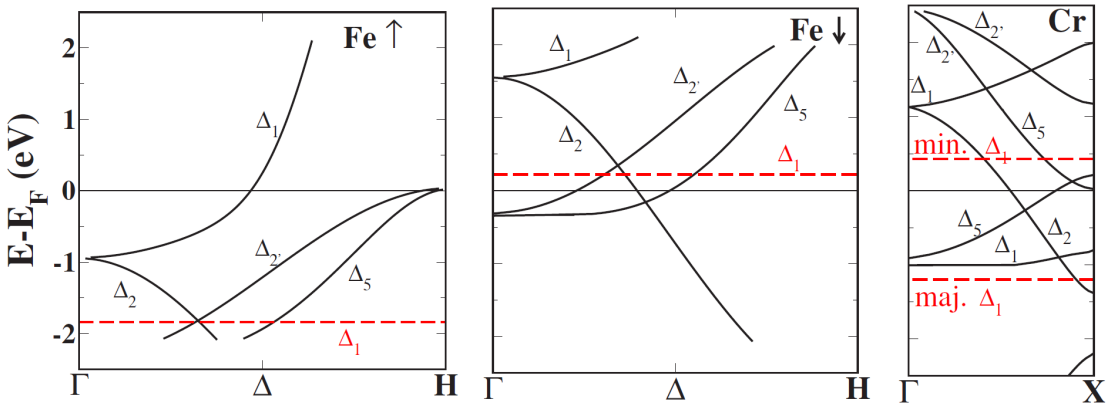

Figure 4.11: Bulk band structures projecting onto $\overline{\Gamma}$ point. The positions of the surface states are indicated by the horizontal red dashed lines. The left panel shows the Fe majority bands, the central one the Fe minority states and the right panel the Cr bands (from [39]).

a significant transmission probability arises and strongly increases at higher energies (follow the green solid line in the left panel of the Fig. 4.12). For the minority channel, the overlap begins higher in energy and the transmission probability starts to increase at around 1.5 eV (follow the blue dashed line in left panel of the Fig. 4.12). Since the Δ_1 band of Cr is spin-degenerate, the energy of maximum transmission for both spin directions is the same (right panel of the Fig. 4.12). Significant difference between the transmission probability of the two magnetic alignments occurs when one accounts for the contribution of the Cr surface states to the tunneling process. In the parallel configuration, the Δ_1 surface state of Cr above Fermi level is of spin-down character and cannot tunnel into the Δ_1 band of the Fe spin-up bulk states due to spin-conservation during the tunneling process. Contrary, in the antiparallel magnetic alignment of tip and sample, this surface state, which is now of spin-up character, contributes to the tunneling process. It crosses the Δ_1 band of Fe majority bulk states and give rises to a narrow peak (located at 0.43 eV) in the majority channel of transmission probability (follow the green solid line in right panel of the Fig. 4.12). The Fe surface states do not tunnel into bulk Cr states and thus they do not contribute to the current as well. Therefore, due to the surface magnetism of the Cr, the transmission probability depends on the magnetization alignment of tip and sample.

The study described above shows the complexity of spin-polarized tunneling in SP-STM magnetic junctions. It suggests that the key point in determining the magnetic signal in SP-STM magnetic junctions is the symmetry and state selective tunneling of the electronic states

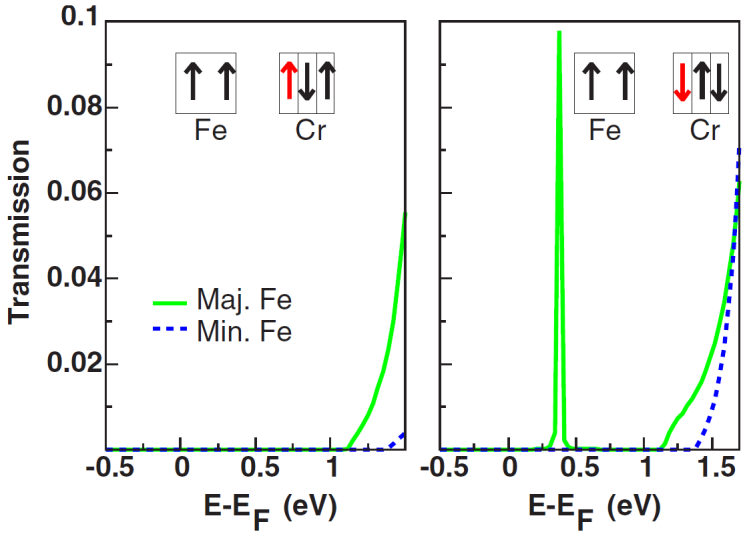

Figure 4.12: Spin-resolved transmission probabilities at $\overline{\Gamma}$ as a function of the electron energy for parallel (left panel) and antiparallel (right panel) alignment of tip and sample magnetization. The green solid and blue dashed curve shows the majority and minority spin channel, respectively (from [39]).

of both electrodes. For the Fe/vacuum/Cr junction the magnetization dependent barrier at the Cr interface contributes to a TMR ratio which is positive (higher conductance for parallel alignment between Fe and Cr surface) with an estimated value larger than 100%. The TMR ratio due to the surface state is negative. Due to the uncertainly of the tip geometry and its effect on the surface state, in practice the contribution of d_{z^2} surface state to spin dependent tunneling is very hard to predict. Although predicted for Cr, this probably applies also to the Co tip based on Fig. 4.9 a.

4.4 Conclusion

The experimental method of spin-polarized scanning tunneling microscopy (SP-STS), which combines high lateral resolution with magnetic sensitivity as well as the access to the electronic structure has been applied to cobalt-double layer nanoislands grown epitaxially on the Cu(111) surface. Since cobalt nanoislands are known to exhibit an out-of-plane magnetization, tips which are magnetized perpendicular to the surface, i.e. Co-coated Ni tip at a Co coverage of a few monolayers have been used. Spin-polarized spectra performed with such magnetic

tip, have allowed to identify two magnetically different cobalt nanoislands types (of the same stacking): either spin up or spin down polarized with respect to the surface plane, in accordance with the previous observations reported in the literature [29, 32, 27]. In addition, the dI/dV maps recorded at energy of the prominent peak below E_F, show that the cobalt nanoislands are spin-polarized in opposite directions. As predicted by the oscillatory behavior of the magnetic asymmetry of the junction and shown by the dI/dV map acquired lower in energy, the spin-polarized contrast of the cobalt nanoislands reverse, indicating that the spin-polarization of the magnetic junction varies with bias voltage. The coexistence of spin up and spin down cobalt nanoislands make them an ideal magnetic system where the tunneling magnetoresistance effect can be probed without employing a external magnetic field. Moreover, this study can be extended to single atoms [27, 36] and molecules (see Chapter 5).

Our simple calculations have shown the important role played by the tip-apex geometry in the magnetic asymmetry of the magnetic tunneling junction. For the geometries considered, the main difference occurred in the negative voltage range. While the magnetic asymmetry calculated with a blunt tip has a positive value and a higher intensity, the magnetic asymmetry obtained with the sharp tip changes sign and displays an oscillatory behavior. As expected, our calculation did not reproduce entirely the experimental magnetic asymmetry. We have indicated some directions for improving the model. Such calculation are however behind the scope of this thesis, a recent theoretical study showing the complexity of such a phenomenon.

Bibliography

[1] P. M. Tedrow, R. Meservey, and P. Fulde. Magnetic field splitting of the quasiparticle states in superconducting aluminum films. Phys. Rev. Lett. **25**, 1270 (1970).

[2] P. M. Tedrow, and R. Meservey. Spin-dependent tunneling into ferromagnetic nickel. Phys. Rev. Lett. **26**, 192 (1971).

[3] P. M. Tedrow, and R. Meservey. Spin polarization of electrons tunneling from films Fe, Co, Ni, and Gd. Phys. Rev. B **7**, 318 (1973).

[4] M. Jullière. Tunneling between ferromagnetic films. Phys. Lett. A **54**, 225 (1975).

[5] M. S. Moodera, L. R. Kinder, T. M. Wong, and R. Meservey. Large magnetoresistance at room temperature in ferromagnetic thin film tunnel junctions. Phys. Rev. Lett. **74**, 3273 (1995).

[6] T. Miyazaki, and N. Tezuka. Giant magnetic tunneling effect in Fe/Al_2O_3/Fe junction. J. Magn. Magn. Mater. **139**, L231 (1995).

[7] S. S. P. Park, C. Kaiser, A. Panchula, P. M. Rice, B. Hughes, M. Samant, and S. H. Yang. Giant tunneling magnetoresistance at room temperature with MgO(100) tunnel barriers. Nature Mater. **3**, 862 (2004).

[8] S. Yuasa, T. Nagahama, A. Fukushima, Y. Suzuki, and K. Ando. Giant room-temperature magnetoresistance in single-crystal Fe/MgO/Fe magnetic tunnel junction. Nature Mater. **3**, 868 (2004).

[9] M. N. Baibich, J. M. Broto, A. Fert, F. Nguyen Van Dau, F. Petroff, P. Eitenne, G. Greuzet, A. Friederich, and J. Chazelas. Giant magnetoresistance of (001)Fe/(001)Cr magnetic superlattices. Phys. Rev. Lett. **61**, 2472 (1988).

[10] G. Binash, P. Grünberg, F. Saurenbach, and W. Zinn. Enhanced magnetoresistance in layered magnetic structures with antiferromagnetic interlayer exchange. Phys. Rev. B **39**, 4828 (1989).

[11] R. Wiesendanger, H. J. Güntherodt, G. Güntherodt, R. J. Gambino, and R. Ruf. Observation of vacuum tunneling of spin-polarized electrons with the scanning tunneling microscope. Phys. Rev. Lett. **65**, 247 (1990).

[12] S. Blügel, D. Pescia, and P. H. Dederichs. Ferromagnetism versus antiferromagnetism of the Cr(001) surface. Phys. Rev. B **39**, 1392 (1989).

[13] M. Kleiber, M. Bode, R. Ravlić, and R. Wiesendanger. Topology-induced spin frustrations at the Cr(001) surface studied by spin-polarized scanning tunneling spectroscopy. Phys. Rev. Lett. **85**, 4606 (2000).

[14] R. Wiesenganger, I. V. Shvets, D. Bürgler, G. Tarrach, H. J. Güntherodt, J. M. D. Coey, and S. Gräser. Topographic and magnetic-sensitive scanning tunneling microscope study of magnetite. Science **255**, 583 (1992)

[15] S. Heinze, M. Bode, A. Kubetza, O. Pietzch, X. Nie, S. Blügel, and R. Wiesendanger. Real-space imaging of two-dimensional antiferromagnetism on the atomic scale. Science **288**, 1805 (2000).

[16] D. Wortmann, S. Heinze, Ph. Kurz, G. Bihlmayer, and S. Blügel. Resolving complex atomic-scale spin structures by spin-polarized scanning tunneling microscopy. Phys. Rev. Lett. **86**, 4132 (2001).

[17] J. Tersoff, and D. Hamann. Theory and application for the scanning tunneling microscope. Phys. Rev. Lett. **50**, 1998 (1983).

[18] B. Voigtländer, G. Meyer, and N. M. Amer. Epitaxial growth of thin magnetic cobalt films on Au(111) studied by scanning tunneling microscopy. Phys. Rev. B **44**, 10354 (1991).

[19] I. Chado, C. Goyhenex, H. Bulou and J. P. Bucher. Cluster critical size effect during growth on a heterogeneous surface. Phys. Rev. B **69**, 085413 (2004).

[20] H. Bulou and J. P. Bucher. Long range substrate mediated mass transport on metal surfaces induced by adatom clusters. Phys. Rev. Lett. **96**, 076102 (2006).

[21] H. A. Dürr, S. S. Dhesi, E. Dudzik, D. Knabben, G. van der Laan, J. B. Goedkoop, and F. U. Hillebrecht. Spin and orbital magnetization in self-assembled Co clusters on Au(111). Phys. Rev. B **59**, R701 (1999).

[22] T. Koide, H. Miyauchi, J. Okamoto, T. Shidara, A. Fujimori, H. Fukutani, K. Amemiya, H. Takeshita, S. Yuasa, T. Katayama, and Y. Suzuki. Direct determination of interfacial magnetic moments with a magnetic phase transition in Co nanoclusters on Au(111). Phys. Rev. Lett. **87**, 257201 (2001).

[23] M. V. Rastei, and J. P. Bucher. Spin-polarized tunneling investigation of nanometer Co cluster by means of a Ni bulk tip. J. Phys.: Condens. Matter **18** L619 (2006).

[24] M. V. Rastei, J. P. Bucher, P. A. Ignatiev, V. N. Stepanyuk, and P. Bruno. Surface electronic states in Co nanoclusters on Au(111): Scanning tunneling spectroscopy measurements and ab initio calculations. Phys. Rev. B **75**, 045436 (2007).

[25] M. Bode, M. Getzlaff, and R. Wiesendanger. Spin-polarized vacuum tunneling into the exchange-split surface states of Gd(0001). Phys. Rev. Lett. **81**, 4256 (1998).

[26] A. Kubetzka, O. Pietzsch, M. Bode, and R. Wiesendanger. Magnetism of nanoscale Fe islands studied by spin-polarized scanning tunneling spectroscopy. Phys. Rev. B **63**, 140407 (2001).

[27] Y. Yayon, V. W. Brar, L. Senapati, S. C. Erwin, and M. F. Crommie. Observing spin polarization of individual magnetic adatoms. Phys. Rev. Lett. **99**, 067202 (2007).

[28] F. Meier, L. Zhou, J. Wiebe, and R. Wiesendanger. Revealing magnetic interactions from single-atom magnetization curves. Science **320**, 82 (2008).

[29] O. Pietzsch, A. Kubetzka, M. Bode, and R. Wiesendanger. Spin-polarized scanning tunneling spectroscopy of nanoscale cobalt islands on Cu(111). Phys. Rev. Lett. **92**, 057202 (2004).

[30] S. Rusponi, T. Cren, N. Weiss, M. Epple, P. Buluschek, L. Claude, and H. Brune. The remarkable difference between surface and step atoms in the magnetic anisotropy of two-dimensional nanostructures. Nat. Mater. **2**, 546 (2003)

[31] S. Rusponi, N. Weiss, T. Cren, M. Epple, and H. Brune. High tunnel magnetoresistance in spin-polarized scanning tunneling microscopy of Co nanoparticles on Pt(111). Appl. Phys. Lett. **87**, 162514 (2005).

[32] O. Pietzsch, S. Okatov, A. Kubetzka, M. Bode, S. Heinze, A. Lichtenstein, and R. Wiesendanger. Spin-resolved electronic structure of nanoscale cobalt islands on Cu(111). Phys. Rev. Lett. **96**, 237203 (2006).

[33] A. Wadas, and H. J. Hug. Model for the stray field from magnetic tips used in magnetic force microscopy. J. Appl. Phys. **72**, 203 (1992).

[34] C. F. Hirjibehedin, C. P. Lutz, and A. J. Heinrich. Spin coupling in engineered atomic structures. Science **312**, 1021 (2006).

[35] C. F. Hirjibehedin, C.-Y. Lin, A. F. Otte, M. Ternes, C. P. Lutz, B. A. Jones, and A. J. Heinrich. Large magnetic anisotropy of a single atomic spin embedded in a surface molecular network. Science **317**, 1199 (2007).

[36] B. W. Heinrich, C. Iacovita, M. V. Rastei, L. Limot, P. A. Ignatiev, V. S. Stepanyuk, P. Bruno, and J. P. Bucher. Spin structure of an atomic protrusion: Probing single atoms on cobalt nanoislands. Phys. Rev. B. **79**, 113401 (2009).

[37] M. C. Desjonqueres, and D. Spanjaard. *Concepts in Surface Physics*. 2nd Edition Springer (1996).

[38] C. J. Chen. Tunneling matrix elements in three-dimensional space: The derivative rule and the sum rule. Phys. Rev. B **42**, 8841 (1996).

[39] J. Enkovaara, D. Wortmann, and S. Blügel. Spin-polarized tunneling between an antiferromagnet and a ferromagnet: first-principles calculations and transport theory. Phys. Rev. B **76**, 054437 (2007).

[40] J. A. Stroscio, D. T. Pierce, A. Davies, R. J. Celotta, and M. Weinert. Tunneling spectroscopy of bcc (001) surface states. Phys. Rev. Lett. **75**, 2960 (1995).

[41] J. Bardeen. Tunneling from a many-particle point of view. Phys. Rev. Lett. **6**, 57 (1960).

[42] P. Mavropoulos, N. Papanikolau, and P. H. Dederichs. Complex band structure and tunneling through ferromagnet /insulator /ferromagnet junctions. Phys. Rev. Lett. **85**, 1088 (2000).

[43] W. H. Butler, X. G. Zhang, T. C. Schulthess, and J. M. MacLaren. Reduction of electron tunneling current due to lateral variation of the wave function. Phys. Rev. B **63**, 092402 (2001).

Chapter 5

Spin-tunneling into a single molecule

The chapter is divided in two sections that comprise experimental and theoretical results. The first section starts with an introduction of the CoPc/Co nanoislands system focusing on the magnetic properties of the nanoislands in parallel with a discussion on the adsorption of CoPc. The next paragraphs include the experimental results which demonstrate the existence of stationary spin-polarization states for CoPc adsorbed on the cobalt nanoislands. Particularly, it is shown how the detection and visualization of these stationary molecular states of opposite polarization is possible. The spatial distribution of the spin-polarized signal over the CoPc is also presented. In a following section, the experimental results are confronted to DFT calculations. These are presented in three different paragraphs. Firstly the adsorption geometry of the CoPc molecules on the cobalt surface is discussed. Follows then a discussion about the interaction occurring at the CoPc/Co surface interface emphasizing the origin of the experimentally observed spin-polarized stationary states. Finally, the nature of the magnetic exchange interaction between CoPc molecule and the magnetic cobalt surface is examined. The chapter ends with a summary of the results.

5.1 Addressing single CoPc molecule by SP-STS

5.1.1 CoPc/Co nanoislands system

With the deposition of submonolayer quantities of Co on Cu(111) kept at room temperature, triangular double-layer-high cobalt nanoislands of fcc and hcp stacking sequences and with a lateral extension from a few nanometers up to 30 nm can be formed. This particular shape of the cobalt nanoislands on Cu(111) surface provides a flat magnetic surface, which can be used to host either molecules or atoms. As we have seen in the previous chapter (§ 4.2.2), the cobalt nanoislands, from a magnetic point of view, coexist in two opposite states. Previous studies by SP-STM under an external applied magnetic field, have revealed that the cobalt nanoislands are ferromagnetic with their magnetization pointing either parallel or antiparallel along the sample normal [1]. The opposite states were distinguished spectroscopically via a contrast arising from the spin-polarized surface d-state of minority character centered at -0.28 V below the Fermi energy. At this voltage, the cobalt nanoislands displaying a higher magnitude in the d resonance (denoted $\uparrow$) have $\vec{m}_S$ oriented parallel ($\theta = 0°$) with respect to the corresponding $\vec{m}_T$ of the tip, while for those exhibiting a lower magnitude of the d resonance (denoted $\downarrow$), the $\vec{m}_S$ is antiparallel oriented ($\theta = 180°$) with respect to $\vec{m}_T$ of the tip. According to Eq. 4.6 (§ 4.2.1) we have in fact:

$$dI/dV_{\uparrow}(\vec{r}_T, -0.28) = n_T n_S + m_T m_S \quad > \quad dI/dV_{\downarrow}(\vec{r}_T, -0.28) = n_T n_S - m_T m_S \qquad (5.1)$$

The magnetic field required to switch the magnetization direction of the cobalt nanoislands depends on their size and ranges between 1.0 T and 1.75 T [1]. A single paramagnetic molecule (for example, CoPc) placed on such a nanoisland will couple with it, so that the direction of its magnetization becomes fixed in time, and is therefore potentially detectable by SP-STS. As shown in the previous chapter, the fact that $\vec{m}_T$ and $\vec{m}_S$ are found to be parallel (antiparallel) for a given voltage allows to determine the alignment of the corresponding magnetizations. In order to deduce the relative orientation of the magnetizations of the tip and of the cobalt nanoislands, an external magnetic field is needed. Nevertheless, the cobalt nanoislands provide a calibrated substrate where two opposite spin-polarized states ($\uparrow$ and $\downarrow$ with respect to the tip and sample plane) are easily accessed.

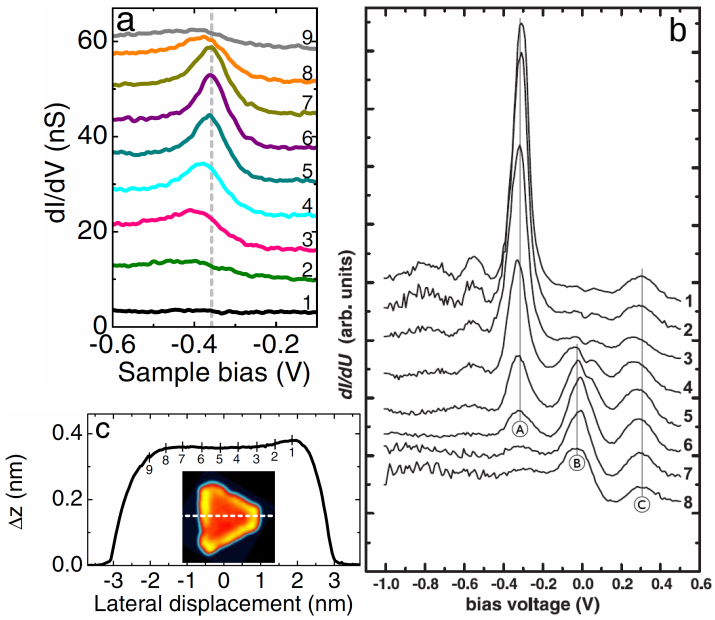

Figure 5.1: a) dI/dV spectra (vertically shifted for clarity) acquired across the Co nanoisland from corner to edge as depicted by the numbers in (b). The dashed line is centered on the position of the d resonance acquired in the nanoisland center (spectra $5-7$) b) Line profile across the Co nanoisland displayed in the inset (from [3]). c) dI/dV spectra (vertically shifted for clarity) measured over one Co nanoisland from edge to inner region. Labels (A), (B) and (C) mark characteristic features: (A) d resonance of the Co nanoislands, (B) zero bias peak existing exclusively in the rim area and (C) minority peak observed on the Co nanoisland as well as in the rim area (from [2]).

The CoPc molecules on the cobalt nanoislands/Cu(111) system have been analyzed in a submonolayer regime. As presented in Chapter 3, at a low coverage of about 0.1 monolayer, the adsorption of the CoPc molecules leads, in a first step, to a preferential occupation of the step edges of the cobalt nanoislands. Secondly, the remaining CoPc molecules prefer to adsorb on top of the cobalt nanoislands as isolated adsorbates, allowing to address and characterize individually each molecule. We have chosen to investigate single CoPc molecules adsorbed around the center of the cobalt nanoislands, far from their edges and corners. The reason is that the cobalt nanoislands are bounded by a rim area with a typical apparent width of 1.7 ± 0.2 nm, i.e. several atomic rows wide with an increased apparent height (Fig. 5.1 c). The electronic structure and the spin-polarized properties of this rim differs from that of the nanoisland's interior [2, 3]. In

these regions, the typical d-resonance (labeled A in Fig. 5.1 b) moves progressively downward in energy while its amplitude is strongly attenuated until disappearance at the edges and the corners (Fig. 5.1 a and 5.1 b). As shown by Rastei et *al.* [3], this particular trend in the d resonance starts at 1.0 nm from the edges and at 2.5 nm from the corners (Fig. 5.1 a and c). In the same time, a new peak, energetically located right at the Fermi level (labeled B in Fig. 5.1 b), emerges in the rim area. This new peak, found neither in the inner region of the cobalt nanoisland nor on Cu(111) surface, has a spin-polarized nature [2]. The spin-polarized contrast close to its energy is inverse, compared to that of the main d resonance (Fig. 5.2 a). When a rim exhibits a positive (negative) asymmetry, the inner region has a negative (positive) asymmetry. The contrast inversion does not mean that both the rim and the inner areas have different magnetizations oriented in an opposite way. It simply shows that, at the Fermi level, the $\vec{m}_S$ of the rim and of the inner area are parallel and antiparallel, respectively with $\vec{m}_T$. Additionally, the in plane Co-Co bound length is inhomogeneously distributed in the rim [3], therefore the four organic ligands of a CoPc molecules adsorbed inside this region experience a different atomic configuration of the substrate underneath. Therefore, in order to simplify the study we have concentrated our attention on individual CoPc molecules adsorbed in the inner region of the cobalt nanoisland. This region is characterized by a nearly homogeneous distribution of Co-Co in plane bond length, where the d resonance has the same amplitude and energetic position and more importantly the spin-polarization is homogeneously distributed everywhere inside its perimeter (Fig. 5.2 a).

One of the great advantages to work at low CoPc coverage is that free areas of the cobalt nanoislands are still available between the adsorbated molecules. This is very important since prior to molecular investigations, one should test and know the spin-polarized status of the cobalt nanoislands. This would not be possible if the entire surface of the nanoisland is covered with molecules. Moreover, the cobalt surface can be exploited to thoroughly test for contamination which may occur during molecular deposition. In fact it has been reported that the surface states of magnetic surfaces are very sensitive to contaminations [4, 5]. Recently, Sicot et *al.* have shown that the adsorption of hydrogen on a cobalt nanoisland drastically affects its surface states [6]. In particular, the d resonance is strongly reduced in intensity and shifted lower in energy (Fig. 5.2 b). On the other hand, it has been reported that the deposition of a monolayer of oxygen on Co(111) surface induces a reversal of its spin polarization. The strong binding, forming between oxygen and cobalt, creates an interface band in the majority-spin channel which strongly enhances the tunneling current in this channel. As a result, the spectroscopic fingerprint

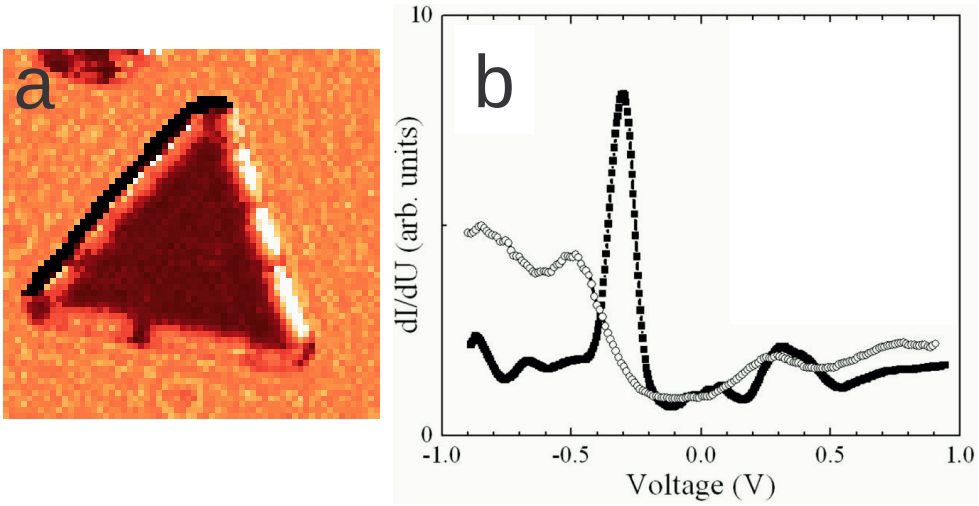

Figure 5.2: a) Typical spin-polarized dI/dV map over one $\uparrow$ cobalt nanoislands taken at -0.01 V revealing a spin contrast of both the rim and the central area. The rim area appears bright while the rest of the nanoisland dim (from [2]). b) dI/dV spectra at 5 K on cobalt nanoisland before (square) and after (open circles) H_2 exposure (from [6]).

of the pristine surface changes. Since the d-like surface states is very sensitive to adsorption of hydrogen and oxygen, the presence of such adsorbats on a cobalt surface can therefore lead to an erroneous interpretation of the data when studying spin-polarized properties. In our case, the dI/dV spectra, acquired on a cobalt nanoisland after CoPc deposition either on the free areas or at very close vicinity of single CoPc, look similar with the one obtained on pristine surface: the d resonances have the same intensity and are located at the same energy. This suggests that $1.)$ the cobalt surface is not contaminated during the deposition of molecules and $2.)$ the presence of CoPc molecules on it do not alter its electronic and spin-polarized properties. Thus, our system, CoPc/cobalt nanoislands is clean and ideal for spin-polarized studies.

In our studies one needs also to account for two specific effects of the cobalt nanoislands, namely size-dependent relaxation [3] and stacking [7], that might influence the spin-polarized properties of CoPc molecules. Regarding the first effect, we have not observed any differences in the spectra acquired on CoPc molecules adsorbed on cobalt nanoislands of different sizes. We have however chosen to investigate CoPc molecules residing on cobalt nanoislands bigger than 10 nm in order to have same reference spectrum over the nanoislands. Moreover, these nanoislands, can host a significant number of CoPc molecules in their central part, which is very advantageous for statistical measurements, and can supply enough free space for checking their

spin-polarized status. On the contrary, we have observed two distinct spectra corresponding to CoPc molecules placed on cobalt nanoislands of different stacking. These will be presented later in this chapter.

5.1.2 Detection of spin-polarized states

The study of single CoPc molecules by SP-STS has been done by imposing two criteria to the selection of the nanoislands. As mentioned above, cobalt nanoislands with a given crystallographic stacking and specific lateral dimensions were chosen. Moreover, since we do not dispose of an external magnetic field to invert the magnetizations direction of the cobalt nanoislands, nanoislands of opposite magnetization are needed, ideally located in close vicinity. To characterize their spin-polarized status we use SP-STS as described in § 4.2.

Taking advantage of the submolecular spatial resolution provided by STM, we have analyzed the spin-polarized properties over an entire CoPc molecule. In the following we focus on the dI/dV spectra acquired by positioning the spin-polarized tip in the middle of CoPc, that means over the Co atom. It has been seen in § 3.2.2, that such a dI/dV spectrum measured with a tungsten tip displays in the negative voltage range, close to Fermi energy, a broad resonance. This resonance is also detected in the dI/dV spectra taken with spin-polarized Co-coated Ni tips (Fig. 5.3 b). The intensity of the resonance is found to be different for CoPc molecules adsorbed on cobalt nanoislands of opposite spin-polarization [8]. As can be seen in the Fig. 5.3 b, all CoPc molecules residing on $\uparrow$ cobalt nanoislands reveal a resonance, which differs from the molecules on $\downarrow$ cobalt nanoislands. Similar with the d resonance of cobalt nanoislands, this result indicates that the molecular resonance is spin-polarized. The CoPc molecules, as revealed by spin-polarized tips, have therefore a spin-polarized structure close to Fermi energy. While the spin-polarized resonance is fairly reproducible, the structure at lower biases was found to be tip dependent. As shown in § 4.3.1, this observation arises from different atomic configuration of the cluster at the very end of the tip, which cannot be totally controlled experimentally so far.

The observation of the spin-polarized steady states by SP-STS over the CoPc suggests that the molecular magnetization is pinned either up or down. This implies that the cobalt magnetic moment of a single paramagnetic CoPc molecules is magnetically coupled to the nanoislands magnetization. As explained in § 4.1.2 and § 4.2.2 the absolute orientation of the magnetization of the cobalt nanoislands cannot be determined by SP-STS even though an external magnetic field is used. Furthermore, our measurements do not unambiguously determine the direction

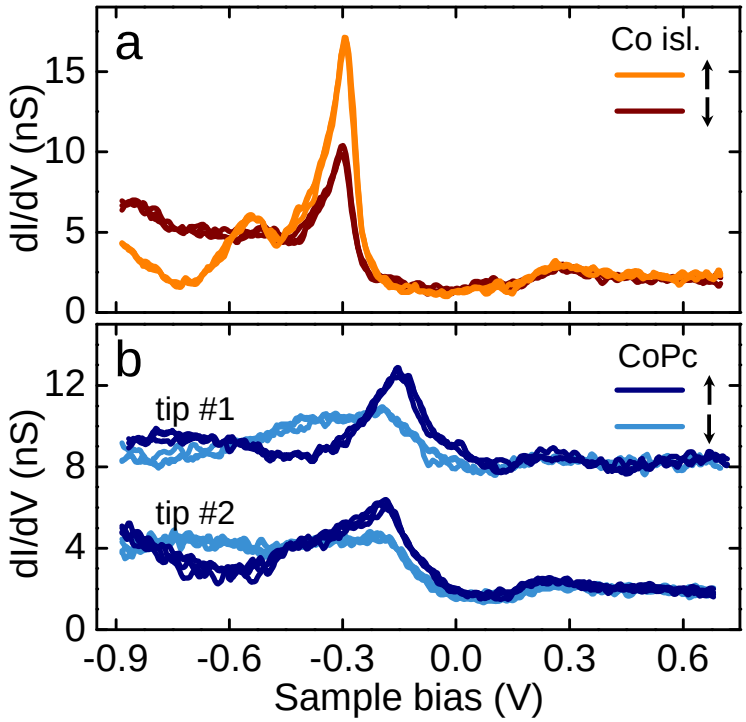

Figure 5.3: a) Typical spin-polarized dI/dV over two cobalt nanoislands of opposite spin-polarization. b) dI/dV spectra acquired over the center of single CoPc molecules adsorbed on cobalt nanoislands of opposite spin-polarization (noted $\uparrow$ and $\downarrow$). Two sets of spectra acquired with distinct tips (noted 1 and 2) are presented. The spectra acquired with tip 1 are displaced upward by 6 nS for clarity. Feedback loop opened at 0.6 V and 0.5 nA (from [8]).

of the total spin (magnetization) of the CoPc because the magnetization is an integral over all filled states (see § 4.1.2) while the spectra shown in the Fig. 5.3 b were taken over a finite voltage range. Therefore, the nature of the magnetic coupling (whether it is ferromagnetic or antiferomagnetic) between the CoPc and the magnetic cobalt surface cannot be established. The SP-STS is not the appropriate technique for revealing such informations. However, our results clearly prove that the CoPc molecules coexist in two different spin-polarized (magnetic) states, this being particularly appealing in view of spin-dependent molecular electronics. These spin-polarized states are likely linked to the bidirectional orientation of the cobalt nanoislands magnetizations. By inverting the nanoislands magnetization, for example, using an external magnetic field, one can then in principle switch the molecular magnetization.

Interestingly, our results are in the line of previous work by Wende et *al.*, which by combining experimental and computational studies have examined the coupling between magnetic

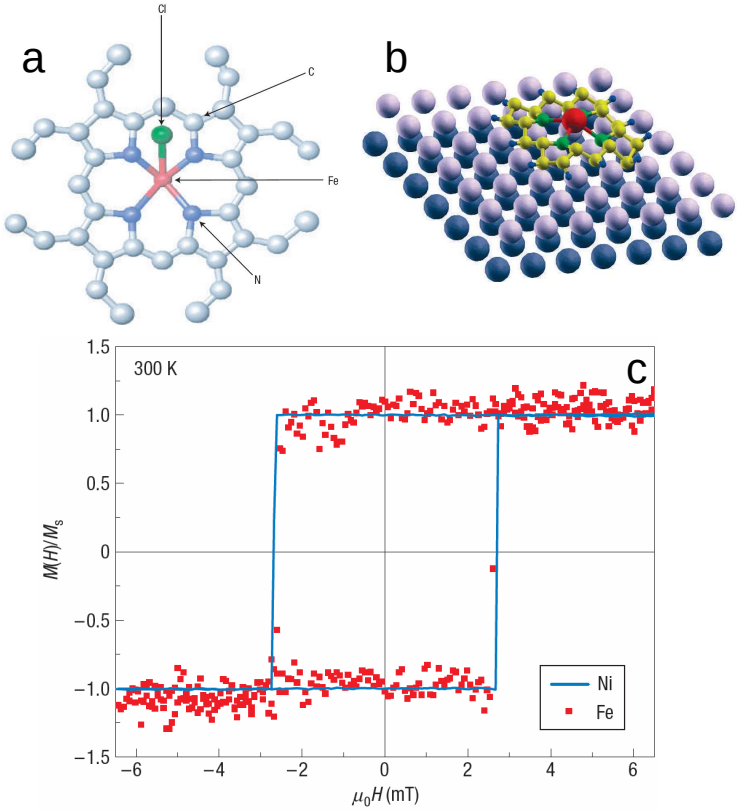

Figure 5.4: a) Schematic illustration of the Fe octaethylporphyrin (OEP) chloride molecule. b) Fe OEP molecule attached to a substrate. The magnetic molecule consists of Fe (red), N (green) and C (yellow). c) The element-specific field dependence of the magnetization of the Fe atoms in the molecule and the ferromagnetic substrate (Ni). Hysteresis curves of the Fe atom (filled squares) and Ni (full line) obtained by the L3 edge XMCD maxima of Fe OEP on Ni/Cu(100) at 300 K (from [9]).

molecules and magnetic surfaces [9]. They have deposited, by sublimation in high vacuum, iron octaethyl porphyrin chloride molecules (FeOEP Cl, Fig. 5.4 a) onto cobalt and nickel magnetic substrates having their easy axis of the magnetization oriented in plane or out of plane, respectively. In a first step they have investigated the structural orientation of the FeOEP Cl molecules, self-assembled in a monolayer and submonolayer, using X-ray absorption spectroscopy (XAS). The authors have found that molecules, upon adsorption on the magnetic surfaces, lose the chloride ion and lay face on (Fig. 5.4 b). The X-ray magnetic circular dichroism (XMCD) measurements have demonstrated that the FeOEP molecules are ferromagnetically coupled with the underlying magnetic surfaces. As shown by the hysteresis loop, the magnetic moment of

the central iron atom aligns along the substrate magnetization (Fig. 5.4 c). An important achievement of these studies is that, depending on the magnetization direction of the magnetic surfaces, the iron magnetic moment can be rotated along directions in plane as well as out of plane.

Finally, a close inspection of Figs. 5.3 a and 5.3 b reveals that, at the voltage where the spin-polarized d resonance of the cobalt nanoislands is located (-0.28 V), both molecular dI/dV spectra are featureless. On the contrary, when an adatom is placed in the middle of the cobalt nanoisland, it exhibits a resonance at this voltage [10], which is spin-polarized [11]. Earlier STM investigations [12, 13], have shown that, such a resonance accounts for a surface induced state [14]. These observations clearly prove that, the spin-polarized resonance detected on CoPc is not induced by the cobalt surface, but it is rather a molecular state.

5.1.3 Visualization of spin-polarized states

To get a full picture on the spin-polarized signal of CoPc, we have plotted the magnetic asymmetry, which results from pairs of spin-polarized spectra (see Eq. 4.7, § 4.2.2) acquired on the central part of CoPc, together with that provided by the cobalt nanoislands of opposite magnetization. Since the spin-polarized asymmetry (especially in the negative voltage range) is very sensitive to the atomic configuration of the tip apex (§ 4.3.1), we have done an average of all the recorded magnetic asymmetries obtained with 13 spin-polarized Co-coated Ni tips. It can be observed that the magnetic asymmetry of the CoPc displays a strong oscillatory behavior in the negative voltage range as the one of the cobalt nanoislands (Fig. 5.5 a). This shows that the spin-polarization of the Co-nanoisland/CoPc-vacuum/Co-tip magnetic junction varies with the sample bias as evident in Fig. 5.3 b. The sign reversal occurs at -0.26 and -0.64 V for CoPc and at -0.12, -0.42, and -0.8 V for cobalt nanoislands, respectively. The asymmetry of CoPc exhibits therefore zero-crossing values which are different from those shown by the bare cobalt nanoisland. This confirms that the spin-polarized signal detected in the Co-nanoisland/CoPc-vacuum/Co-tip magnetic junction refers to an inherent property of CoPc molecule and not of the cobalt nanoisland as remarked above.

A visual rendering of both the dI/dV spectra (Fig. 5.3 a and 5.3b) and the magnetic asymmetries (Fig. 5.5 a) can be done by performing dI/dV maps at different sample biases, for two cobalt nanoisland of opposite magnetization and partially covered with single CoPc molecules. The pixel intensity on each dI/dV maps corresponds to the differential conductance

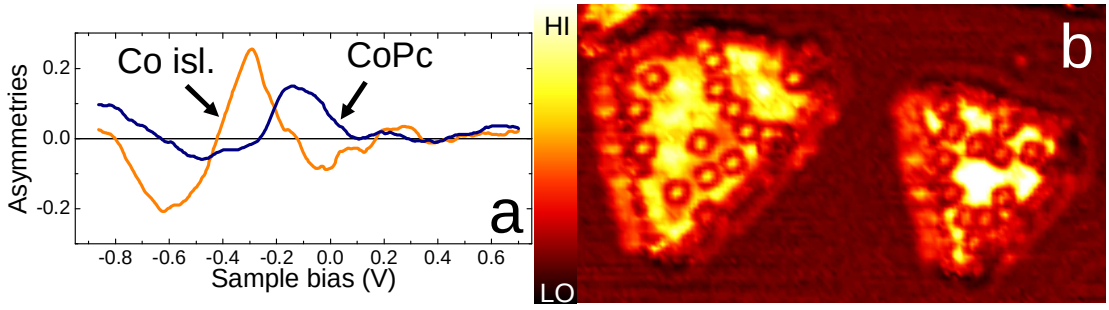

Figure 5.5: a) Asymmetries arising from opposite polarizations for CoPc and the cobalt nanoislands. b) Spin-polarized dI/dV maps taken at -0.29 V (image size: 40×20 nm^2). Feedback loop opened at 0.6 V and 0.5 nA.

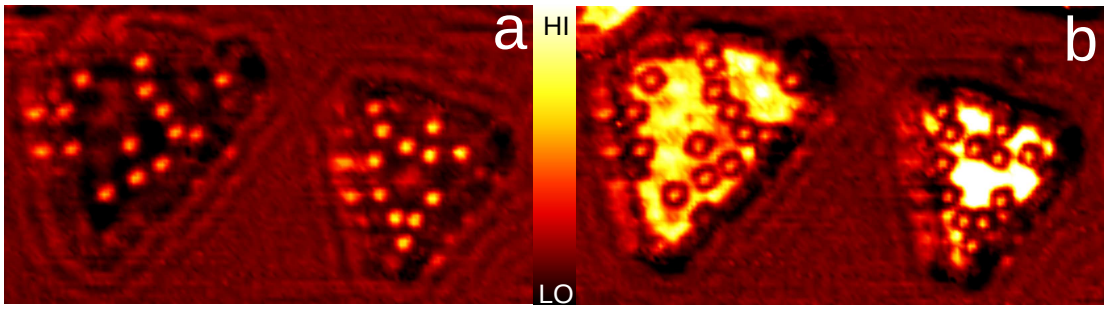

Figure 5.6: Spin-polarized dI/dV maps taken at a) -0.16 V and b) -0.32 V (image size: 40×20 nm^2). Feedback loop opened at 0.6 V and 0.5 nA.

at a given sample bias. Figure 5.5 b represents a dI/dV map measured at sample bias of -0.29 V, where the magnetic asymmetry of the cobalt nanoislands exhibits the maximum value. As already shown in § 4.2.2 at this energy the cobalt nanoislands of opposite magnetization display a strong spin-polarized contrast. The cobalt nanoisland on the right is spin-polarized ↑, while the left nanoislands is spin-polarized ↓. Since the CoPc magnetic asymmetry has a value close to zero (Fig 5.5 a), the CoPc molecules have similar intensities on both cobalt nanoislands (Fig. 5.5 b). The oscillatory behavior of the CoPc magnetic asymmetry (Fig. 5.5 a) suggests that a spin-contrast between ↑ and ↓ CoPc molecules becomes visible when moving upward or downward in energy. We define the CoPc molecules as ↑ if residing on nanoislands that are ↑, and CoPc molecules as ↓ if residing on nanoislands that are ↓. Figure 5.6 a displays a dI/dV map measured at a sample bias of -0.16 V, where the magnetic asymmetry of the CoPc exhibits the maximum value (Fig. 5.3 b). The spin-polarized states of the CoPc molecules occur as bright circular dots, with different intensities depending on the spin-polarization of the cobalt nanoislands. The ↑ (bright) CoPc molecules residing on the ↑ cobalt nanoisland exhibit a higher differential conductance compared to the ↓ CoPc molecules adsorbed on the ↓ cobalt nanoisland. Both cobalt nanoislands have nearly the same intensity (Fig. 5.6 a), since their magnetic asymmetry has a value close to zero at this sample bias (Fig. 5.5 a). This further confirms that the spin-polarized contrast observed in the Fig. 5.6 a is related to an intrinsic property of the CoPc molecule. A spin-polarized contrast is also detected lower in energy, for example at -0.32 V (Fig. 5.6 b). Compared to the previous dI/dV maps, the spin-polarized contrast is the same for cobalt nanoislands, but it is reversed for the CoPc molecules. In this case the brighter molecules, which exhibit the higher differential conductance, are those residing on ↓ cobalt nanoisland (Fig. 5.6 b).

In order to confirm the above observations on the spin-polarized contrast we have compared the profiles of the differential conductance taken over both ↑ and ↓ CoPc molecules. Figures 5.7 a and 5.7 c display such profiles extracted from Figs. 5.6 a and 5.6 b, respectively. Note that the profiles are along one molecular axis and extend on the cobalt surface (Fig. 5.7 b). Their origin is chosen at the center of the CoPc. As can be clearly seen in Fig. 5.7 a, at this location on the molecule, the dI/dV signal given by the ↑ CoPc (6.7 nS) is larger than that showed by the ↓ CoPc (4.4 nS). The difference between the spin-polarized dI/dV signals decreases as we move away from the center of the CoPc. On the cobalt nanoislands both signals have the same intensity of 2.0 nS in accordance with the dI/dV map displayed in Fig. 5.6 a. The profiles plotted in the Fig. 5.7 c show that, while the ↓ CoPc molecule exhibits a larger

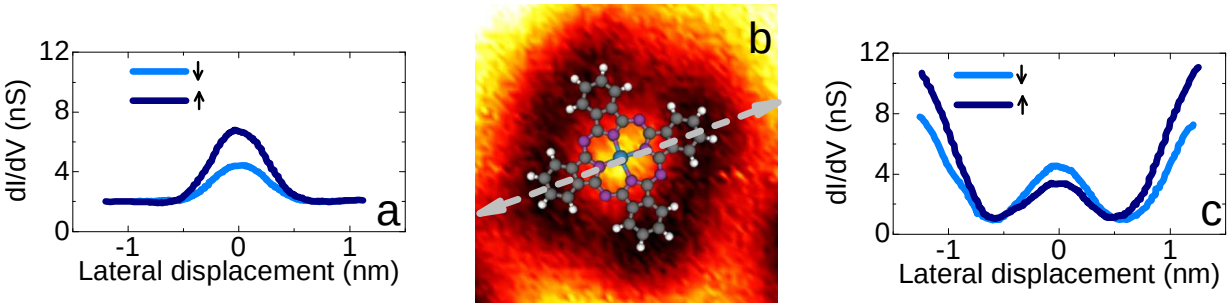

Figure 5.7: a) and c) Profiles of the differential conductance along an individual CoPc extracted from Figs. 5.6 a and 5.6 b, respectively. b) dI/dV map of a $\downarrow$ CoPc taken at -0.32 V with the model molecular structure superimposed (image size: 2.6×2.6 nm^2). Feedback loop opened at 0.6 V and 0.5 nA. The double grey arrow indicates the trajectory of the profile.

dI/dV signal than $\uparrow$ CoPc, the $\downarrow$ nanoisland shows a smaller dI/dV signal than $\uparrow$ nanoisland. This further confirms the reversal of the spin-polarized signal of the CoPc when moving downward in energy, as well the existence in the same time and independently of a spin-polarized signal over the cobalt nanoislands. In between these two regions, the profiles also exhibit an area where their intensity is the same (1.1 nS). This area corresponds to the benzene rings. As can be seen in the Fig. 5.7 b, where the structural model of the CoPc molecule is superimposed on a high-resolution dI/dV map acquired over a single CoPc molecule, the benzene rings of the organic ligands appear as dim regions around the bright region. This bright, 1 nm wide region centered at the Co atom reveals that the spin-polarized signal is spatially limited to this area.

The spatial variation of the differential conductance across the CoPc molecule confirms the above result. The spin-polarized molecular resonance progressively decreases in intensity when moving from the center towards the benzene ring (blue curves on the Fig. 5.8 a) and completely vanishes on the benzene ring (green curves on the Fig. 5.8 a). At this stage the corresponding spin-polarized resonance of Co nanoisland starts to appear and it is progressively recovered when moving from benzene ring to the pristine cobalt surface (yellow to red curves on the Fig. 5.8 a). In the Fig. 5.8 b, we have plotted the dI/dV spectra recorded over the benzene rings of CoPc molecules spin-polarized $\uparrow$ and $\downarrow$. It can be observed that in the voltage range of interest both spectra are featureless and present nearly the same amplitude, 2 nS. Moreover, their corresponding magnetic asymmetry (Fig.5.6 a) is a straight and noisily horizontal line with an amplitude close to zero. Therefore no spin-polarized contrast is evidenced in this bias range. However, spin-polarized metastable-atom deexcitation spectroscopy (SPMDS) measurements

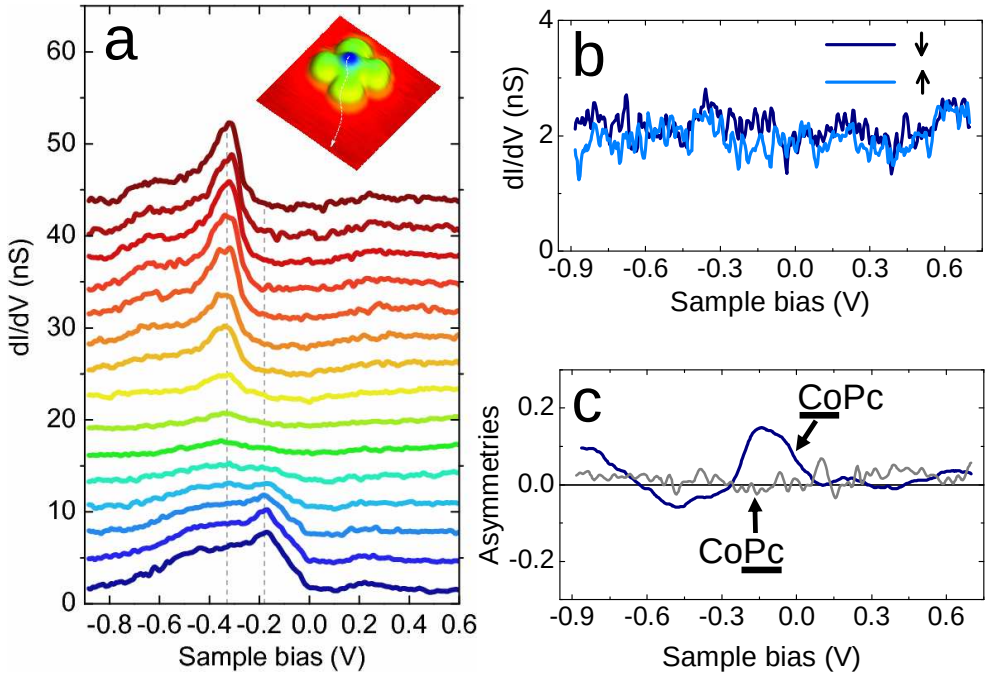

Figure 5.8: a) Spatial variation of the conductance across a CoPc molecule. dI/dV spectroscopic mapping taken from the center of CoPc toward the Co nanoisland as depicted by the arrow in the inset. The color palette of the spectra matches the palette of the CoPc image in the inset, indicating the location where the dI/dV spectra were acquired. The dashed grey lines are centered on the dominant peaks of the CoPc molecule and of the cobalt nanoisland. Feedback loop opened at 0.6 V and 0.5 nA. c) dI/dV spectra over the benzene rigs of CoPc spin-polarized $\uparrow$ and $\downarrow$. d) Asymmetries arising from two CoPc of opposite polarization.

combined with density functional calculations have evidenced the spin polarization for benzene adsorbed on an Fe(100) surface [15, 16]. Most likely, in this voltage range, either a spin polarization exists over the benzene rings, but it is so small in intensity that cannot be detected, either the spin-polarized signal of the benzene rings is located beyond the investigated voltage range.

The magnetic asymmetries for cobalt nanoislands of different stacking together are displayed in the Fig. 5.9 with the magnetic asymmetries corresponding to CoPc molecules adsorbed on both type of nanoislands. It can be observed that the distinct maxima of both magnetic asymmetries of cobalt nanoislands arise at approximately the same voltage, while for the CoPc molecules they occur at different voltages. This is evidenced by a shift of the magnetic asymmetry for CoPc on fcc nanoislands toward E_F by about 0.06 V relative to the magnetic asymmetry

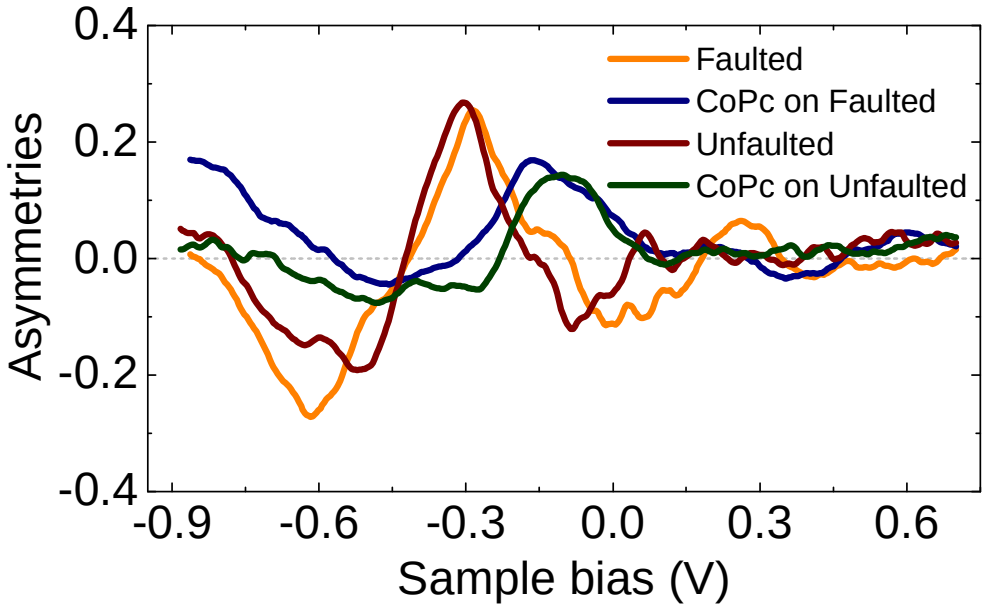

Figure 5.9: Asymmetries arising from two cobalt nanoislands of opposite magnetization for either fcc or hcp stacking and from CoPc molecules residing on them.

for CoPc on hcp nanoislands. It follows that for the CoPc molecules adsorbed on fcc cobalt nanoislands the spin-polarized molecular resonance is located at -0.1 V. Therefore the cobalt nanoislands stacking influences the spin-polarized spectroscopic signature of CoPc. It is worth to mention that although the spin-polarization of the tip states also influences the measured spin-polarization ($\S$ 3.3), a different sign of the magnetic asymmetry at the same energy leads to the conclusion that the molecular spin-polarization is indeed inverted for fcc stacking relative to hcp stacking at energies between: -0.31 V and -0.22 V, -0.68 V and -0.56 V.

5.1.4 The advantages of a local probe technique

In the last years, the interaction between the spin of individual magnetic molecules (especially those comprised from either phthalocyanine or porphyrine unit with a magnetic atom caged at its center) and electrons from a nonmagnetic metal environment has been studied through Kondo effect [17]. The Kondo effect typically arises from spin-flip scattering events between a single magnetic impurity and the electronic spins of a metal host. This interaction causes a correlated screening cloud to form around the impurity atom below the Kondo temperature, leading to anomalous behavior in the resistivity. The Kondo temperature is proportional to

the antiferromagnetic coupling arising between the impurity spin and the electronic spins of the metal host. Several groups have demonstrated using a cryogenic scanning tunneling microscope that, for these Kondo systems, a narrow resonance-like structure is detected in the differential conductance (dI/dV) near the Fermi level [18, 19, 20, 21, 22, 23]. The Kondo state detected in the STS measurements is determined by the Fano interference between two tunneling paths [24]. Electrons originating from the tip can tunnel through the magnetic center and then flow to the surface or tunnel directly into empty surface states. The two quantum paths interfere and depending on their relative weight produce a dipped spectrum or a peaked spectrum or a more complex line shape also known as Fano line shape [25]. In contrast to this "dynamic" process, in our case, the spin of the CoPc is fixed in time, here above detected as bidirectional spin-polarized stationary states. Therefore, our results provide for the first time, a direct visualization of spin-polarization of a single molecule.

The above cited studies on the Kondo effect of single magnetic molecules have attracted a special attention. The study of Iancu et *al.* [20] has shown that, by varying the nearest neighbor coordination number of a single magnetic molecule, inside a two-dimensional molecular self-assembly, the Kondo temperature can be tuned between 105 and 170 K. The same authors have also shown that the Kondo temperatures can be manipulated by changing the molecular conformation of a single magnetic molecule [19]. Different Kondo temperatures were also found for a single dehydrogenated CoPc molecule adsorbed either on terraces of Au(111) surface or to its monoatomic steps [18, 23]. Moreover, the CoPc molecules adsorbed at the monoatomic steps in two typical configurations (with either one or two lobes attached on the higher Au terrace and the others on the lower terrace) exhibit different Kondo temperatures. Finally, it was also shown that the signal of the Kondo resonance depends strongly on the adsorption site of a central Fe atom of a single FePc adsorbed on a Au(111) surface [21]. All these mentioned studies demonstrate that the interaction between the individual localized spin of a magnetic molecule and the spins of the conduction electrons of the surface is very sensitive to $1.)$ the local molecular environment of the single magnetic molecule, $2.)$ the adsorption conformation of the single magnetic molecule on the terrace and at the steps and $3.)$ the adsorption site adopted by its central magnetic ion. The parameters listed above are likely to drive the magnetic properties of single magnetic molecule adsorbed on a magnetic surface. These effects are difficult to access, when an average technique, as XMCD, is used to exploit such systems. The received signal is a collection of signals provided by the investigated specific element of all the molecules adsorbed on the magnetic surface: on terraces, at step edges, at kinks. Obviously, for unambiguous

investigations of the magnetic properties of a single magnetic molecule adsorbed on a magnetic surface, local examinations are required. An example of such studies is what we have presented in this section. In contrast to Wende et *al.* studies, we were able to probe, by means of SP-STM, the location, adsorption configuration and local environment of singles CoPc molecules adsorbed on the magnetic cobalt surfaces. Moreover, we also addressed specific sub-molecular groups of the single CoPc, which allowed us to visualized the spatial distribution of the spin-polarized signal.

To gain insight into the experimetal results, first-principle calculation based on density functional theory by means of the PWSCF package [26] have been performed. These will help us to answer the questions concerning: the origin of the spin-polarized molecular resonance, its spatial distribution and the coupling between the single CoPc and the magnetic cobalt surface. These theoretical studies are presented in the next section.

5.2 Modeling the adsorption of CoPc on Co nanoislands

5.2.1 Adsorption configuration

As a starting point, the adsorption geometry of CoPc molecule adsorbed on a cobalt nanoisland is determined. We are also interested to find the adsorption site adopted by the central cobalt atom of CoPc. This is very important to known since the Kondo effect was found to depend on it [21]. The magnetic surface was mimicked by using a slab model consisting of three Cu layers with two Co layers on top and about 2.2 nm vacuum to the next periodic repeated layer. The CoPc molecule was placed above the Co layers resulting in a 302 atom model. In the geometry optimization of the adsorption model, all the Cu atoms were held fixed at their positions according to bulk values. Instead, CoPc molecule together with the two Co layers were allowed to fully relax.

Single cobalt atoms deposited on Pt(111) surface prefer to sit on both hexagonal close-packed (hcp) and face-centered cubic (fcc) lattice sites [27]. Owing to the fact that the interaction of the CoPc molecule with the magnetic cobalt surface might be dominated by the organic ligands (benzene rings, the outer or inner nitrogen atoms), the cobalt atom might a priori be in a top, bridge or hollow position. The starting configuration was with the cobalt atom

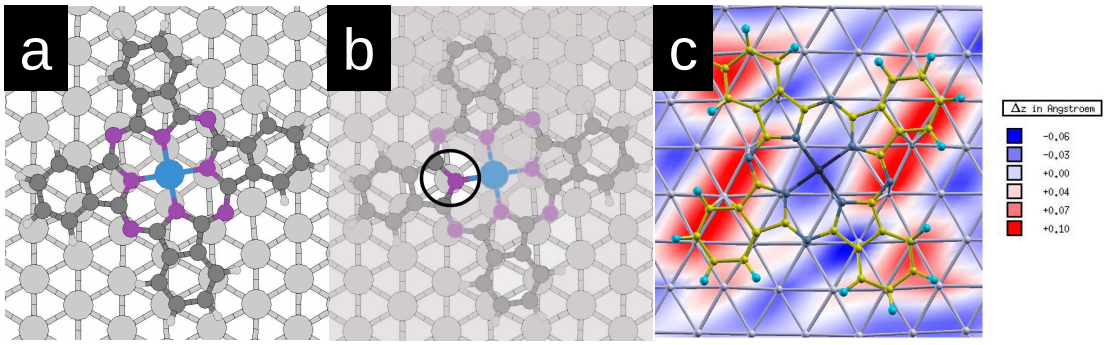

Figure 5.10: a) Schematic representation of a CoPc molecule adsorbed in a bridge configuration on a cobalt surface b) View of a pyrrole nitrogen atom placed on top of a cobalt surface atom. c) Vertical displacement in Å of the surface atoms with respect to the non-distorted surface as obtained from the geometry optimization.

of CoPc on the hollow site. This position is favorable only if the system CoPc/two cobalt layers is not relaxed. The relaxation of the system brings the cobalt atom of CoPc onto a top or a bridge position. At this stage the competition between the interactions of different components of the CoPc, as the benzene rings, the outer and inner (pyrrole) nitrogen atoms or the cobalt atom, with the surface below will determine whether it is on the top or bridge. The lowest energy from the geometry optimization was obtained when the cobalt atom of CoPc resides in a bridge position (Fig. 5.10 a). The adsorption energy of this configuration is 1.0 eV lower than that in top configuration. This big difference suggests that this configuration is very stable. As shown for FePc adsorbed on Au(111) surface, a small difference in the adsorption energy between bridge and top configuration implies that both configurations exist simultaneously [21]. The coexistence of two configurations on the Au(111) surface detrimental for both Cu(111) and Co surfaces, might be explained by the fact that the average in-plane Au-Au distance in the topmost surface layer is larger compared to the Cu-Cu and Co-Co distances, which are quite close. As on the Cu(111) surface, the driving force for the bridge position is the interaction of the four pyrrole nitrogen atoms of CoPc with the cobalt atom beneath: the p_z-orbitals of these nitrogen atoms allow for hybridization with $d_{3z^2-r^2}$-orbitals of the surface atoms. The geometry optimization reveals that the pyrrole nitrogen atoms are located on top of a surface atom (Fig. 5.10 b). These atoms should show the largest wavefuction overlap, thus providing a possible magnetic exchange pathway. The distance between the nitrogen and the cobalt surface atom is estimated, in all cases, to 0.19 nm, slightly shorter than the distance between nitrogen

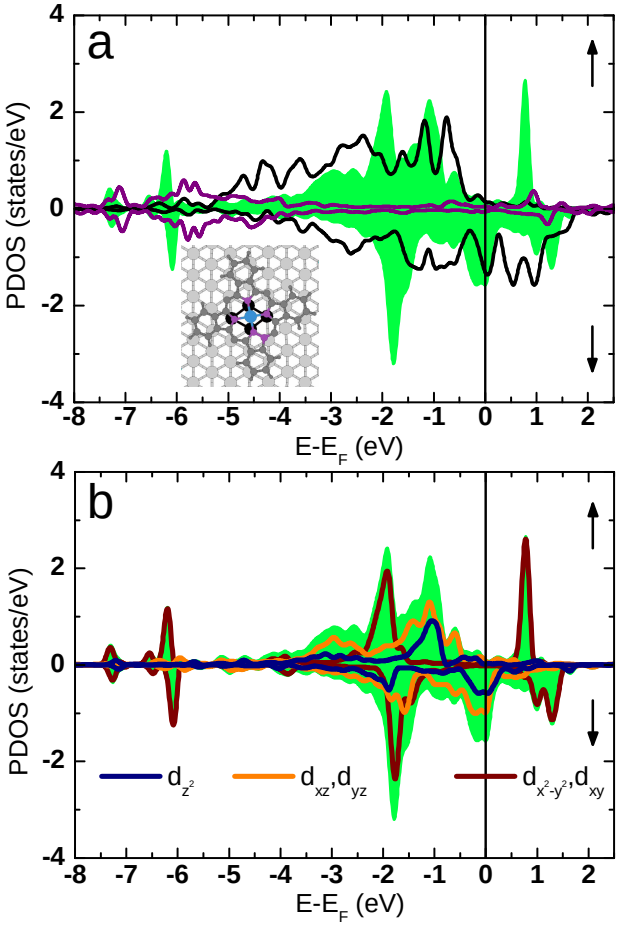

Figure 5.11: a) PDOS of a Co atom of CoPc (green), of a pyrrole N atom (purple) and of the cobalt surface atom (black) beneath the N (top panel, majority PDOS; bottom panel, minority PDOS). b) m-resolved d-contribution on PDOS of Co atom of CoPc.

and cobalt atom of CoPc. In the bridge configuration, the distance between the surface atoms and the cobalt atom of CoPc was found to be about 0.25 nm, close to the in-plane Co-Co distance in the topmost surface layer. The cobalt surface shows negligible distortions of only 0.02 nm or lower (Fig. 5.10 c).

5.2.2 Partial density of states

Figure 5.11 a represents the spin-polarized partial density of states (PDOS) of the cobalt atom of CoPc, of a pyrrole nitrogen atom and of the cobalt surface atom beneath the nitrogen

as sketched in the inset, while Fig. 5.11 b shows the contribution of different d-orbitals of the cobalt atom of CoPc on PDOS. These PDOS give information on possible hybridizations among atoms of CoPc and with the surface atoms. The chemical bonding between the CoPc and the surface is provided by a small hybridization between cobalt surface atoms and nitrogen/carbon atoms of CoPc. This is realized at binding energies between -4.0 to -6.0 eV (Fig. 5.11 a). An hybridization between the cobalt atom of the CoPc and its nitrogen atoms also exists, which can be recognized from the occurrence of peaks close in energy below -4.0 eV for the $3d$-states of Co and $2p$-states of N (Fig. 5.11 a). As an example, the peak located at -6.0 eV for majority states is a bonding combination of p-nitrogen and $d_{x^2-y^2}$-cobalt states (Fig. 5.11 a). Note that the PDOS of the nitrogen atoms (organic ligands) are featureless between -4.0 eV and $+1.0$ eV. Since this is also the case for C atoms (not shown), it probably explains the absence of a spin-polarized signal over the organic parts of CoPc (see Fig. 5.8 b).

The PDOS of the cobalt atom in the free-standing CoPc molecule is spin-polarized (§ 3.1.4, Fig. 3.8), indicating the existence of a magnetic moment in this molecule of about $1.09\ \mu_B$. After deposition of the CoPc molecule on the cobalt surface, the PDOS of CoPc changes. In particular, the d_{z^2}-minority state, which is unoccupied in the free-standing CoPc molecule (§ 3.1.4, Fig. 3.8), it is here broadened over several electronvolts below E_F (Fig. 5.11 b), resulting in a reduced magnetic moment of $0.7\ \mu_B$. We have seen in § 3.1.4 that, the d_{z^2}-minority state of CoPc upon adsorption on Cu(111) becomes completely filled, so that the magnetic moment of CoPc is zero. The same scenario happens when CoPc is adsorbed on Au(111) [18]. The use of a cobalt substrate can therefore provide a chemical interaction distinct from that observed, e.g., in studies utilizing Cu(111) and Au(111) substrates. Compared to the free-standing CoPc, both minority and majority $d^*_{x^2-y^2}$-antibonding states are shifted to lower energies with about 1.5 eV (Fig. 5.11 b). Owing to the minority character of the cobalt surface, the bonds between surface atoms and the minority CoPc electrons are favored, inducing large differences between the PDOS of the two spin channels. For instance, the minority $d^*_{x^2-y^2}$-antibonding state is split into two states, whereas the majority is only shifted to lower energies (Fig. 5.11 b). This is also different from the Cu(111) surface, where the $d^*_{x^2-y^2}$-antibonding states are shifted to lower energies but not split (§ 3.1.4, Fig. 3.10). Also the minority d_{z^2}-state near E_F is split due to the interaction with the surface (Fig. 5.11 b). The prominent minority peak at -2.0 eV corresponds to a d_{xy}-state (Fig. 5.11 b). Contrary to the findings over adatoms placed in the middle of a cobalt nanosislands [10], our spin-polarized resonance at -0.19 V detected by SP-STS over cobalt atom of CoPc has the origin in the d-orbitals of

the central cobalt ion of CoPc and is not a surface-induce state. Indeed, a close inspection of the PDOS reveals that it likely originates from a mixture of minority d_{z^2} and d_π- states, the contribution of $d_{x^2-y^2}$ and d_{xy}- states being negligible near E_F (Fig. 5.11 b). This conclusion should also hold in the vacuum region where the tip is, since states with a small in-plane $\overrightarrow{\kappa}$ -component are the states that show the slowest decay into vacuum, i.e. the states to which STM is the most sensitive.

In order to obtain a more detailed insight concerning the chemical bonding it is useful to analyze the wavefunctions or charge densities within an energy window. Selected wavefunctions supporting the above discussion are shown in (Fig. 5.12). The left upper panel displays a state with σ-bonding character between the p-nitrogen and the $d_{x^2-y^2}$-cobalt atom of CoPc states realized at -6.2 eV below E_F. A corresponding unoccupied antibonding combination located at 0.7 eV above E_F is shown on the upper right panel. The lower left panel exhibits a selected example of d_π bonding of either cobalt atom of CoPc or cobalt surface atom with nitrogen p_z-orbital, while the right panel shows a direct coupling of the cobalt atom of CoPc to the cobalt surface atom below (dotted white circle).

Figures 5.13 a and 5.13 b represent the calculated spin-polarized PDOS of the cobalt ion of the CoPc when it is adsorbed on top and hollow site (unrelaxed system), respectively. It can be notice that the d-orbital distribution near the Fermi level changes with the adsorption site. Remarkable changes in the d-orbital distribution near the Fermi level occur when the cobalt atom of CoPc resides on a top site (Fig. 5.13 a). It can be observed that the minority d_{z^2}-state are completely depleted near the E_F, while the minority d_π- state is shifted lower in energies. For the hollow and bridge configurations, the d-orbital distribution near the Fermi level is roughly equivalent except for a slight energy shift (Figs. 5.13 a and 5.11 b). While the contribution of $d_{x^2-y^2}$ and d_{xy}- states are negligible near E_F for both configurations, the minority d_{z^2} and d_π- states invert their weights with the adsorption site. For instance, the minority d_{z^2}-state is enhanced at the Fermi level for hollow site compared to the bridge site. Therefore different adsorption site induce different interaction between d-orbitals and the substrate, which influence the spin-polarized stationary states and consequently the spin-polarized transport through single CoPc molecules. This is in line with what is observed for the Kondo resonance in single FePc molecules adsorbed on a Au(111) surface [21]. These observations anticipate that control over the adsorption geometry of a molecule, which can be achieved modifying its lateral structure by the careful attachment of ligands [28], opens up the possibility to tailor its spin-polarized properties and consequently its spin conductance to the desired specifications.

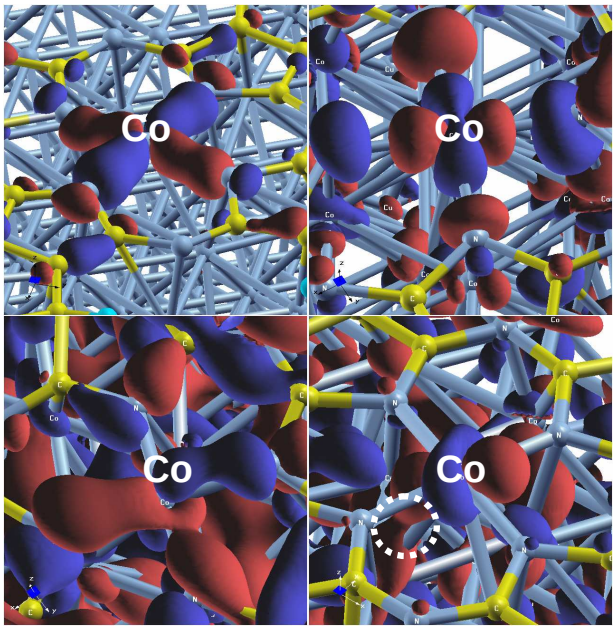

Figure 5.12: The upper left (right) shows a bonding (antibonding) combination of Co $d_{x^2-y^2}$ with N p-states. The lower left panel presents an example of d_π bonding with N p_z-orbitals. The right panel is showing a direct coupling of CoPc to the surface below, indicated by a dotted white circle.

5.2.3 Magnetic coupling

Further insight into the mechanism of the magnetic coupling between CoPc and the cobalt surface can be obtained from an analysis of the magnetization densities (Fig. 5.14). This convincingly shows that between a CoPc molecule and the underlying cobalt surface a ferromagnetic coupling is established. As anticipated from the experimental data (Fig. 5.8 a) the largest magnetization density is found close to the cobalt atom of the CoPc molecule. There is also a magnetization of $0.05\ \mu_B$ or lower at some inner nitrogen and carbon atoms of the benzene rings pointing in the opposite direction with respect to the cobalt atoms. The pyrrole N atom atop a cobalt surface atom (Fig. 5.10 b) realize a Co-N-Co angle close to $90°$, where the two Co atoms refer to Co surface atom and Co atom of CoPc, respectively. According to the Goodenough-Kanamori-Anderson rules for superexchange [29, 30], in this configuration the d-orbitals of both Co atoms (CoPc and surface) communicate via a hybridization with two different p-nitrogen states (Fig. 5.14 b). Firstly, the Hund's first rule applied to the two p-orbitals favors a parallel alignment of their spin (black arrows in Fig. 5.14 b). Secondly, the electrons

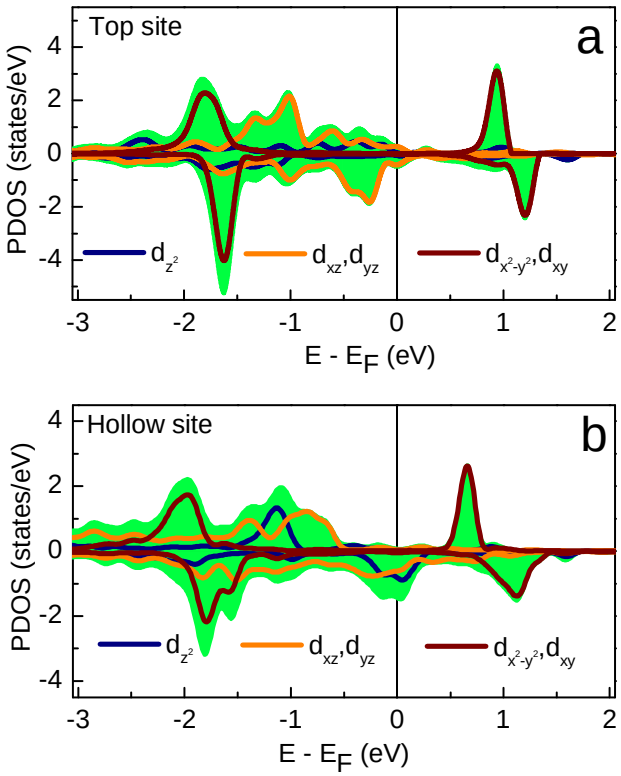

Figure 5.13: m-resolved d-contribution on PDOS of Co atom of CoPc adsorbed on a) top and b) hollow site (unrelaxed system).

in the overlapping lobes have opposite spins in the ground state configuration to satisfy the exclusion principle of Pauli (black and red arrows in Fig. 5.14 b). Thus, the spins of both cobalt magnetic atoms are parallel oriented (red arrows in Fig. 5.14 b), and the ferromagnetic coupling is favored. Therefore, the indirect exchange interaction mediated by the pyrrole N atom generate a ferromagnetic coupling between CoPc and cobalt surface beneath. The geometry optimization revealed that, in the bridge configuration the distance between the surface atoms and the cobalt atom of CoPc is about 0.25 nm, which is comparable to the average distance within the cobalt surface. This suggests that a direct exchange coupling exists as well between both cobalt atoms (CoPc and surface).

Similarly, the studies presented in § 5.1.2 have illustrated that the spin of the central atom of FeOEP molecules aligns parallel to the substrate magnetization [9]. The computational investigations performed by the authors have shown that the ferromagnetic coupling is established by the same kind of superexchange interaction as in our case. A direct exchange coupling was

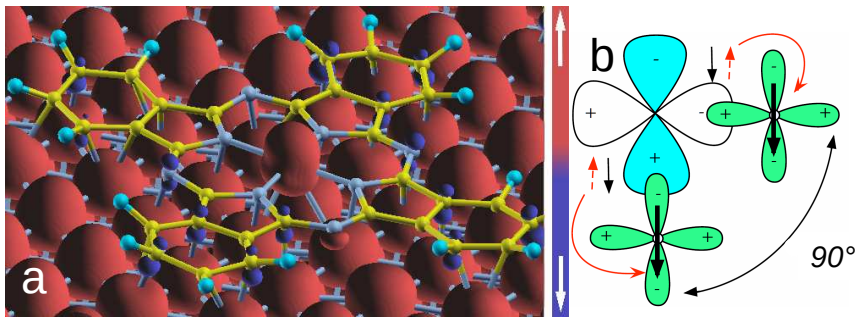

Figure 5.14: (color online) a) Isosurface plot of the magnetization density (↑, magnetization in the "up" direction; ↓, "down" direction). b) Schematic representation of $90°$ superexchange coupling mechanism between two d-orbitals mediated by two p-orbitals.

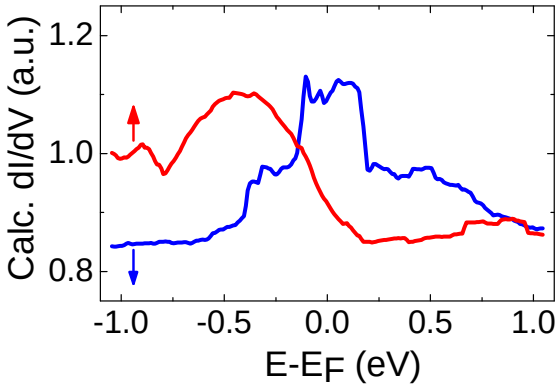

Figure 5.15: Calculated differential conductance (majority ↑, minority ↓).

not predicted since they found a distance between the iron atom of FeOEP and the surface atoms of 0.35 nm, which would be relatively large for a direct overlap of Fe and Co d-orbitals. The same authors have demonstrated, both experimentally and theoretically, that an antiferromagnetic coupling can be realized by placing oxygen atoms in between the FeOEP molecules and the magnetic substrates [31]. In this particular geometry Fe-O-Co (the angle is $180°$), the oxygen p_z orbital is responsible for the antiparallel spin alignment.Such a geometry could be directly studied at a single molecular level using a spin-polarized-STM.

In order to link the calculations to the experimental dI/dV curves (Fig. 5.3 b), the spin-dependent charge densities over the cobalt atom of CoPc is exploited according to the Tersoff-Hamann approximation [32]. The dI/dV curves were obtained by differentiating the numerical $I(V)$ curves with respect to energy, assuming a parallel alignment of both tip and sample magnetization (the tip is 100% spin-polarized). This approach gives the same results as the

more straightforward method proposed by Wortmann et *al.* [33]. According to Eq. 4.2 (§ 4.1.2) a change in contrast corresponds to a change of $\overrightarrow{m}_S$ at a given energy eV and at a given location of the sample. Equivalently, the spin-dependent differential conductance is directly proportional to the spin-resolved charge density at an energy eV (§ 4.2.1, Eq. 4.6). The corresponding dI/dV curves near E_F for both majority and minority states (Fig. 5.15) show reasonable agreement with SP-STS data on Fig. 5.3 b. It can be observed that a change of contrast is predicted at -0.15 V. Clearly, for a complete comparison to SP-STS, the spin-polarized tip needs to be included in the simulations as discussed in Chapter 4.

5.3 Conclusion

We have combined low-temperature spin-polarized scanning tunneling microscopy and model DFT calculations to study for the first time the spin transport across single CoPc molecules adsorbed on well characterized cobalt nanoislands with opposite magnetization. The interaction between the CoPc molecule and the cobalt surface results in two molecular spin states clearly discernible in the differential conductance of the spin-polarized tunnel junction. A spin-polarized resonance is detected for all CoPc molecules adsorbed on $\uparrow$ cobalt nanoislands with an amplitude different from the CoPc molecules adsorbed on $\downarrow$ cobalt nanoislands. The spin-polarized signal is localized over the central part of the CoPc. Such stationary states correspond to the two *up* and *down* orientations of the molecular magnetization on the cobalt nanoislands, which cannot be fully determined experimentally by SP-STS.

DFT calculations have shown that the central cobalt atom of CoPc preferentially adsorbs on the bridge site with respect to the cobalt surface atoms. The bridge site is achieved due to the particular configuration of the N atoms atop of the cobalt surface atoms. Calculations have revealed that the chemical binding of CoPc to the magnetic substrate primarily takes place between the carbon and nitrogen atoms of the CoPc and the cobalt surface atoms. Contrary to single atoms which posses a spin-polarized stationary state induced by the magnetic cobalt surface, the calculation have shown that our molecular stationary states involved in the spin-dependent tunneling arise from the d_{z^2}, d_{xz} and d_{yz} orbitals of Co atom of the CoPc molecule. Furthermore, it was also shown that, the distribution of d-orbitals of Co atom around Fermi level is site dependent, which may influence the spin-polarized electron tunneling through the CoPc molecule. The magnetization density have identified a ferromagnetic coupling between

CoPc and the magnetic cobalt surface, which is generated through two mechanisms: $1.)$ a $90°$ superexchange coupling mediated through the pyrrole nitrogen atoms and $2.)$ a direct exchange coupling between central cobalt ion of CoPc and cobalt atoms of the surface.

Bibliography

[1] O. Pietzsch, A. Kubetzka, M. Bode, and R. Wiesendanger. Spin-polarized scanning tunneling spectroscopy of nanoscale cobalt islands on Cu(111). Phys. Rev. Lett. **92**, 057202 (2004).

[2] O. Pietzsch, S. Okatov, A. Kubetzka, M. Bode, S. Heinze, A. Liechtenstein and R. Wiesendanger. Spin-resolved electronic structure of nanoscale cobalt islands on Cu(111). Phys. Rev. Lett. **96**, 237203 (2006).

[3] M. V. Rastei, B. Heinrich, L. Limot, P. A. Ignatiev, V. N. Stepanyuk, P. Bruno, and J. P. Bucher. Size-dependent surface states of strained cobalt nanoislands on Cu(111). Phys. Rev. Lett. **99**, 246102 (2007).

[4] F. J. Himpsel, and D. E. Eastman. Intrinsic Λ_1-symmetry surface state on Co(0001). Phys. Rev. B **20**, 3217 (1979).

[5] W. Eberhardt, F. Greuter, and E. W. Plummer. Bonding of H to Ni, Pd, and Pt surfaces. Phys. Rev. Lett. **46**, 1085 (1981).

[6] M. Sicot, O. Kurnosikov, O. A. O. Adam, H. J. M. Swagten, and B. Koopmans. STM-induced desoption of hydrogen from Co nanoislands. Phys. Rev. B **77**, 035417 (2008).

[7] A. L. Vazquez de Parga, F. J. Garcia-Vidal, and R. Miranda. Detecting electronic states at stacking faults in magnetic thin films by tunneling spectroscopy. Phys. Rev. Lett. **85**, 4365 (2000).

[8] C. Iacovita, M. V. Rastei, B. W. Heinrich, T. Brumme, J. Kortus, L. Limot, J. P. Bucher. Visualizing the spin of individual cobalt-phthalocyanine molecules. Phys. Rev. Lett. **101**, 116602 (2008).

[9] H. Wende, M. Bernien, J. Luo, C. Sorg, N. Ponpandian, J. Kurde, J. Miguel, M. Piantek, X. Xu, Ph. Eckhold, W. Kuch, P. M. Panchmatia, B. Sanyal, P. M. Oppeneer, and O. Eriksson. Substrate-induced magnetic ordering and switching of iron porphyrin molecules. Nature Mater. **6**, 516 (2007).

[10] B. W. Heinrich, C. Iacovita, M. V. Rastei, L. Limot, P. A. Ignatiev, V. S. Stepanyuk, P. Bruno, and J. P. Bucher. Spin structure of an atomic protrusion: Probing single atoms on cobalt nanoislands. Accepted in Phys. Rev. B.

[11] Y. Yayon, V. W. Brar, L. Senapati, S. C. Erwin, and M. F. Crommie. Observing spin polarization of individual magnetic adatoms. Phys. Rev. Lett. **99**, 067202 (2007).

[12] L. Limot, E. Pehlke, J. Kröger, and R. Berndt. Surface-state localization at adatoms. Phys. Rev. Lett. **94**, 036805 (2005).

[13] F. E. Olsson, M. Persson, A. G. Borisov , J. P. Gauyacq, J. Lagoute and S. Fösch. Localization of the Cu(111) surface state by single Cu adatoms. Phys. Rev. Lett. **93**, 206803 (2004).

[14] B. Simon. Ann. Phys. (N.Y.) **97**, 279 (1976).

[15] X. Sun, T. Suzuki, M. Kurahashi, J. W. Zhang, and Y. Yamauchi. First-principles study on the spin polarization of benzene adsorbed on Fe(100) surface. J. Appl. Phys. **101**, 09G526 (2007).

[16] X. Sun, T. Suzuki, M. Kurahashi, J. P. Wang, and S. Entami. Spin polarization study of benzene molecule adsorbed on Fe(100) surface with metastable-atom deexcitation spectroscopy and density functional calculations. J. Phys. Chem. C **111**, 15289 (2007).

[17] J. Kondo. Resistance minimum in dilute magnetic alloys. Prog. Theor. Phys. **32**, 37 (1964).

[18] A. Zhao, Q. Li, L. Chen, H. Xiang, W. Wang, S. Pan, B. Wang, X. Xiao, J. Yang, J. G. Hou, and Q. Zhu. Controlling the Kondo effect of an adsorbate magnetic ion through its chemical bounding. Science **309**, 1542 (2005).

[19] V. Iancu, A. Deshpande, and S. W. Hla. Manipulating Kondo temperature via single molecule switching. Nano Lett. **6**, 820 (2006).

[20] V. Iancu, A. Deshpande, and S. W. Hla. Manipulating of the Kondo effect via twp-dimensional molecular assembly. Phys. Rev. Lett. **97**, 266603 (2006).

[21] L. Gao, W. Li, Y. B. Hu, Z. H. Cheng, Z. T. Deng, Q. Liu, N. Jiang, X. Lin, W. Guo, S. X. Du, W. A. Hofer, X. C. Xie, and H. J. Gao. Site-specific Kondo effect at ambient temperature in iron-based molecules. Phys. Rev. Lett. **99**, 106402 (2007).

[22] Y. S. Fu, S. H. Ji, X. Chen, X. H. Qiu, B. Sun, P. Zhang, J. F. Jia, and Q. K. Xue. Manipulating the Kondo resonance through quantum size effects. Phys. Rev. Lett. **99**, 256601 (2007).

[23] A. Zhao, Z. Hu, B. Wang, X. Xiao, J. Yang, and J. G. Hou. Kondo effect in single cobalt phthalocyanine molecules adsorbed on Au(111) monoatomic steps. J. Chem. Phys. **128**, 234705 (2008).

[24] M. Plihal and J. W. Gadzuk. Nonequilibrium theory of scanning tunneling spectroscopy via adsorbate resonances: Nonmagnetic and Kondo impurities. Phys. Rev. B **63**, 085404 (2001).

[25] U. Fano. Effects of configuration interaction on intensities and phase shifts. Phys. Rev. **124**, 1866 (1961).

[26] PWSCF is part of the Quantum-ESPRESSO package (www.pwscf.org).

[27] F. Meier, L. Zhou, J. Wiebe, and R. Wiesendanger. Revealing magnetic interaction from single-atom magnetization curves. Science **320**, 82 (2008).

[28] D. X. Shi, W. Ji, X. Lin, X. B. He, J. C. Lian, L. Gao, J. M. Cai, H. Lin, S. X. Du, F. Lin, C. Seidel, L. F. Chi, W. A. Hofer, H. Fuchs, and H. J. Gao. Role of Lateral Alkyl Chains in Modulation of Molecular Structures on Metal Surfaces. Phys. Rev. Lett. **96**, 226101 (2006).

[29] J. B. Goodenough. *Magnetism and the Chemical Bond*. Wiley, New York (1963).

[30] P. W. Anderson. Exchange in Insulators: Superexchange, Direct Exchange, and Double Exchange in: *Magnetism* vol. **1**, G. T. Rado and H. Suhl eds. Academic Press, New York (1963).

[31] M. Bernien, J. Miguel, C. Weis, Md. E. Ali, J. Kurde, B. Krumme, P. M. Panchmatia, B. Sanyal, M. Piantek, P. Srivastava, K. Baberschke, P. M. Oppeneer, O. Eriksson, W. Kuch, and H. Wende. Tailoring the nature of magnetic coupling of Fe-porphyrin molecules to ferromagnetic substrates. Phys. Rev. Lett. **102**, 047202 (2009).

[32] J. Tersoff and D. R. Hamann. Theory and application for the scanning tunneling microscope. Phys. Rev. Lett. **50**, 1998 (1983).

[33] D. Wortmann, S. Heinze, Ph. Kurz, G. Bihlmayer, and S. Blügel. Resolving complex atomic-scale spin structures by spin-polarized scanning tunneling microscopy. Phys. Rev. Lett. **86**, 4132 (2001).

Chapter 6

Summary and Outlook

Cobalt(II) phthalocyanine (CoPc) is a molecule with an extended π-electron system comprising 18 delocalized electrons. Together with the central metal ion, this π-system is quite capable of maintaining electrons in specific spin states for sustained periods, making the CoPc an ideal and desirable candidate for spintronics applications [1]. In this thesis, the electronic and the spin-polarized properties of individual CoPc molecules have been studied both on non-magnetic [Cu(111)] and magnetic (cobalt nanoislands) metal surfaces. An extensive investigation has been carried out by combining both scanning tunneling microscopy (STM) and spin-polarized scanning tunneling microscopy (SP-STM). In order to achieve a more deeper understanding, DFT calculations have been used to assist the analysis and the interpretation of the experimental data.

The adsorption of individual CoPc molecules on the Cu(111) surface leads to a reduction of the symmetry of the molecule: the four-fold symmetry of CoPc molecules (presented in the gas phase) is reduced to a two-fold symmetry. Thereby, at the given voltage, CoPc evolves with one axis pronounced and a second perpendicular axis appearing at reduced apparent height. The appearance of the CoPc in STM images, as well as the degree of observed reduced molecular symmetry, depends on the applied bias voltage, i.e, the involved molecular states in the tunneling. The loss of symmetry is also seen in the dI/dV spectra acquired on different locations over adjacent molecular lobes. The features, found in the dI/dV spectra, vary significantly with and within the molecular axis. First principle calculations based on density functional theory reveal that the energetically favored adsorption geometry corresponds to the bridge position, i. e. the cobalt atom of the molecule is centered between two surface atoms of copper. In fact

the CoPc molecule is guided on the bridge position by the nitrogen atoms which are located on top of underlying copper atoms. The calculations predict an undeformed CoPc on the Cu(111) surface, however the electronic and magnetic properties of the free-standing CoPc molecule change upon adsorption on the Cu(111) substrate. In particular, the LUMO (d_{z^2}) becomes occupied and splits into a bonding and an anti-bonding state compared to the free-standing CoPc molecule where it is half-emptied. The molecule-surface interaction leads to a complete cancellation of the magnetic moment of CoPc: both the spin-down and spin-up states are equally filled. The different atomic configuration underneath both perpendicular molecular axes induce different electronic effects between them and the surface.

Consequently, the adsorption of four-fold symmetric CoPc on substrates with incommensurate symmetries as Cu(111) can provide a valuable contribution to the understanding of molecule-substrate interactions. In order to gather more information about the symmetry loss, future experimental and theoretical investigations are envisioned. A detailed mapping of the tunnel transport properties is going to be performed using the STM in constant-height mode of operation: the tip is kept at a constant height relative to the surface. This operating mode of the STM presents mainly two advantages compared to the usual constant-current mode. Firstly, the comparison to the calculated data is simplified, since simulations are also carried out at a constant height. Secondly, the signal-to-noise ratio is considerably improved since the feedback loop of the STM is opened during the acquisition of all the dI/dV spectra, giving then access to minute spectral features otherwise difficult to detect. As an example, a constant-height dI/dV map over a single CoPc molecule taken at 0.28 V together with the model structure of CoPc superimposed on it is presented in Fig. 6.1. Beside the anticipated symmetry loss of the CoPc molecule, the dI/dV map offers information on the intramolecular tunnel transport properties of different components of the CoPc. It can be observed that the maximum signal (in black) is detected over the C-C bond shared by the benzene and the pyrrol rings along the brighter molecular axis.

The major objective of this thesis was to perform SP-STM measurements over single CoPc molecules adsorbed on magnetic cobalt nanoislands grown on the Cu(111) surface. These nanoislands exhibit a perpendicular magnetic anisotropy, having their magnetization oriented either up or down, with respect to the surface plane. This inherent property makes them an ideal magnetic system where the tunneling magnetoresistance effect can be probed without employing an external magnetic field. Single CoPc molecules adsorbed on such magnetic system posses a molecular resonance located near E_F and arising from the d_{z^2}, d_{xz} and d_{yz} orbitals of the central

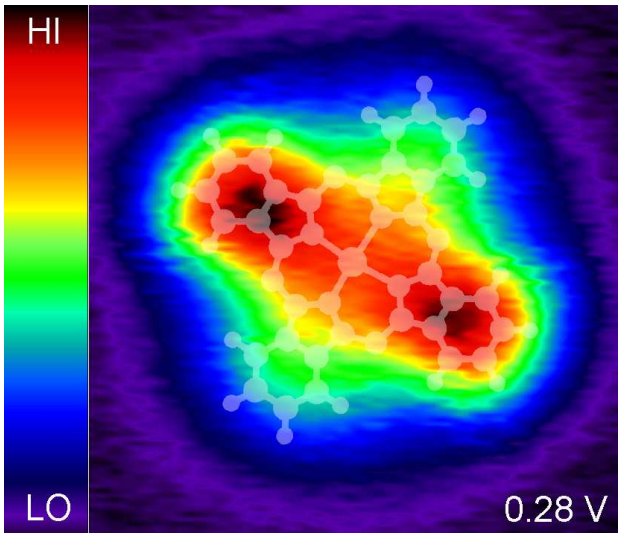

Figure 6.1: Constant-height dI/dV map over CoPc. The feedback loop was opened at $I = 0.35$ nA and $V = 0.28$ V. The model structure of CoPc is superimposed to the dI/dV map in order to localize the signal maximum (in black). (from [2]).

cobalt atom. The molecular resonance becomes spin-polarized (exhibits a different intensity), when the CoPc molecules are adsorbed on cobalt nanoislands of opposite magnetization. The dI/dV map recorded at the energy of the molecular resonance shows that the CoPc molecules are spin-polarized in opposite direction. Near E_F, the spin-polarized signal is detected over the central part of the CoPc. No spin-polarized contrast is evidenced over the benzene rings of the CoPc near E_F. The theoretical calculations predict that the central cobalt ion of the CoPc molecule preferentially adsorbs on the bridge site with respect to cobalt surface atoms. As on the Cu(111) surface, the bridge site is achieved due to the particular configuration of the pyrrole nitrogen atoms atop of cobalt surface atoms. The spin magnetic moment of the CoPc molecule is affected by the interaction with the magnetic cobalt surface, being reduced to 0.7 μ_B. The theoretical calculations also predict an optimal Co-substrate distance of 0.25 nm and a direct ferromagnetic exchange coupling of the CoPc to the cobalt surface. The ferromagnetic ordering is also stabilized due to a superexchange interaction, which is mediated through the four pyrrole nitrogen atoms.

The detection and visualization of the two spin-polarized stationary molecular states represent the most original result of this thesis. This achievement represents a fundamental step towards the development of spintronic devices based on metallorganic molecules supported on

a solid magnetic substrate. Our experiments demonstrate that this can be achieved through the coupling of the molecular spin to the magnetic substrate of opposite magnetization. Future work could consist in extending the present study on CoPc to other molecular systems. For example, single molecular magnets are potentially interesting as they exhibit a large spin ground-state and a large magnetic anisotropy [3]. It was recently shown that the inherent properties of bis(phthalocyaninato) terbium (III) molecules are preserved upon adsorption on the Cu(111) surface [4], making it a candidate molecule for spin-polarized measurements. Another interesting application would be to study the magnetic interaction between the spins of different magnetic atoms linked by organic ligands to form either a single molecule [5, 6] or an extended two-dimensional array [7].

Bibliography

[1] C. G. Claessens, U. Hahn, and T. Torres. Phthalocyanines: From outstanding electronic properties to emerging applications. The chemical record **8**, 75 (2008).

[2] B. W. Heinrich, L. Limot, C. Iacovita, D. J. Choi, M. V. Rastei, J. P. Bucher, W. A. Hofer, T. Brumme, and J. Kortus. Unveiling the chemical bond between a single CoPc and a copper surface. In preparation

[3] L. Bogani, and W. Wernsdorfer. Molecular spintronics using single-molecule magnets. Nat. Matt. **7**, 179 (2008).

[4] L. Vitali, S. Fabris, A. Mosca Monte, S. Brink, M. Ruben, S. Baroni, and K. Kern. Electronic structure of surface suppported bis-(phthalocyaninato)terbium(III) single molecule magnets. Nano Lett. **10**, 3364 (2008).

[5] M. Mannini, F. Pineider, P. Sainctavit, C. Danieli, E. Otero, C. Sciancalepore, A. M. Talarico, M. A. Arrio, A. Cornia, D. Gatteschi, and Roberta Sessoli. Magnetic memory of a single-molecule quantum magnet wired to a gold surface. Nat. Matt. **8**, 194 (2009).

[6] R. Yamachika, X. Lu, D. Wegner, Y. Wang, A. Wachowiak, M. Grobis, L. M. C. Beltran, J. R. Long, M. Pederson, and M. F. Crommie. Local electronic properties of titanocene chloride dimer molecules on a metal surface. J. Phys. Chem. C **113**, 677 (2009).

[7] P. Gambardella, S. Stepanow, A. Dmitriev, J. Honolka, F. M. F. de Groot, M. Lingenfelder, S. S. Gupta, D. D. Sarma, P. Bencok, S. Stanescu, S. Clair, S. Pons, N. Lin, A. P. Seitsonen, H. Brune, J. V. Barth, and Klaus Kern. Supramolecular control of the magnetic anisotropy in two-dimensional high-spin Fe arrays at a metal interface. Nat. Matt. **8**, 189 (2009).